Diffractive Photoproduction of ρ Mesons with Large Momentum Transfer at HERA

Carl Gwilliam

2006

Particle Physics Group
School of Physics and Astronomy

A thesis submitted to The University of Manchester for the degree of
Doctor of Philosophy in the Faculty of Engineering and Physical Sciences

Contents

List of Figures

List of Tables

Abstract

The diffractive photoproduction of ρ mesons with large momentum transfer, $\gamma p \to \rho Y$, where Y is the proton remnant, is studied with the H1 detector at HERA using an integrated luminosity of 20.1 pb^{-1}. The photon-proton centre of mass energy spans the range $75 < W < 95$ GeV and the photon has a virtuality $Q^2 < 0.01$ GeV^2. The t dependence of the cross section is measured in the range $1.5 < |t| < 10.0$ GeV^2, where t is the the four momentum transferred at the proton vertex. The t behaviour is well described by a power law, $d\sigma/dt \propto |t|^{-n}$, which yields $n = 4.26 \pm 0.06$ (stat.) $^{+0.06}_{-0.04}$ (syst.). The spin density matrix elements, which provide information on the helicity structure of the interaction, are extracted using measurements of the decay angular distributions. The data indicate a violation of s-channel helicity conservation, with contributions from both single and double helicity-flip observed. The results are compared to the expectation of a perturbative QCD model based on BFKL evolution.

No portion of the work referred to in this thesis has been submitted in support of an application for another degree or qualification of this or any other university or other institute of learning.

This work was supported financially by the Particle Physics and Astronomy Research Council (PPARC) between October 2002 and September 2005.

For my parents and my sisters, Toni and Paula

Acknowledgements

The fat lady is warming up and so, before my brain turns completely to mush, I would like to take a brief moment to thank all the people who have played a part, both in my PhD itself and also in life outside of it – which they assure me exists.

Firstly, those people from Manchester without whom this thesis would not exist. Top of that list is my supervisor Robin Marshall, who introduced me to H1 in the first place and suggested an interesting project for my PhD. Thanks are also due to Brian Cox, for helping with thesis queries and reading it through, Roger Barlow, for help with all things statistical and beyond, Stefan Soldner-Rembold, for several useful discussions, and Jeff Forshaw, for reading the theory sections of this thesis without laughing too much. Finally, this section would not be complete without a warm thank you to Fred Loebinger, who was instrumental in convincing me to come to Manchester in the first place and to continue with a particle physics PhD here. You've got him to blame!

On the analysis side, thanks must go to Xavier Janssen for his efforts to explain all things vector meson, even when I was being particularly dim-witted, and his continual help, without which I would never have got this far. Oh, and nice Mohican by the way! Thanks must also go to Duncan Brown for his help in the early days and the two-dimensional fitting stuff at the end. My referees, Pierre Marage and Vincent Boudry, deserve thanks for their knowledge and insight, which helped to knock the analysis into shape at the end. In fact, the entire diffractive group at H1 were great. Outside H1, thanks to Rikard Enberg (and Jeff, who can't be here due to a prior engagement in the previous paragraph) for providing the model curves shown in chapter 7.

Living in Hamburg was a great experience, which was made all the more fun (or maybe interesting is a better word) due to the people I met there. A warm handshake

goes to Matt Beckingham, Oliver Henshaw, Mudhahir Ismail, Paul Laycock, Nick Malden, Dave South, Dan Traynor and many others too numerous to list here. Particular thanks must go to Andy Rimmer for keeping me sane (no easy task) and providing some good laughs, even if many of these came about through his bumbling incompetence. Be sure to watch out for falling 'Happy Christmas' signs!

Back in Manchester, the biggest thank you goes to Sarah Allwood. Not only is she a great friend but she somehow managed to put up with living with me for four years without once trying to kill me, although she probably came close. Thanks also to Peter Moore (who has had the misfortune to know me since the very first week), James Monk (no, London is not the capital of Wales), Mitchell Naisbit, Irina Nasteva, Paul Telford (badum tish!) and the rest of the HEP group. A particular mention to Dave Mercer for making coffee times, which were rather too frequent, that bit more interesting and regularly providing cake. In addition, thanks to Simon Bray and Kate Kersley for being great neighbours and providing regular distractions, most notably in the form of trips to the (dangerously cheap) local pub.

I would like to thank all my, rather large, family for the love, warmth and encouragement they have shown throughout the years. Finally, special thanks to Mum, Dad, Toni and Paula for always being there when I need you. Also, for never failing to believe that I could do this even when I, in my usual pessimistic way, could see no light at the end of the tunnel. This thesis is for you and, as such, it is only fair that you be forced to read it until you understand every last word...!

As a final postscript, I draw your attention to the 'standard euro-person' who provides a sense of perspective, not only for the H1 detector, but everything else too.

Chapter 1

Introduction

The aim of particle physics is to study both the fundamental particles of nature and the forces which act between them. Perhaps the least well understood of these forces is the strong force, which, in the Standard Model, is described in terms of the gauge theory Quantum Chromodynamics (QCD). Unlike the electromagnetic force, the strong coupling constant, α_s, increases strongly with increasing distance or, equivalently, decreasing energy. This gives rise to the concept of confinement, whereby free quarks and gluons are not observed experimentally. Only in the presence of a hard scale, which is larger than the typical QCD energy scale, Λ_{QCD}, does α_s become small enough to allow perturbative methods to be applied to QCD. Such perturbative QCD (pQCD) calculations have proved very successful in describing short distance physics [1] but not all processes contain such a hard scale.

Total hadronic cross sections are dominated by peripheral soft interactions. Although the absence of a hard scale prevents the application of pQCD, these can be successfully described using the phenomenological model of Regge theory [2]. At high energy, the total cross section is primarily due to the exchange of an object with the quantum numbers of the vacuum [3]. This object is known as the pomeron and interactions described by its exchange are termed diffractive. Such events are

characterised by a large region of no hadronic activity between two distinct systems of particles in the final state, known as a rapidity gap.

The observation of rapidity gaps in deep inelastic scattering (DIS) ep collisions at HERA [4] rejuvenated the field of diffraction. The presence of a hard scale, afforded by the high virtuality, Q^2, of the intermediate photon which mediates the reaction, allows pQCD calculations to be performed. In this language, diffraction is viewed as the exchange of two or more gluons in a colour singlet state [3] and it is this lack of colour transfer that gives rise to the observed rapidity gap. Events in the photoproduction regime, where the photon is quasi-real ($Q^2 \approx 0$), may also exhibit the characteristics of a hard interaction. Such a hard scale may be provided by the mass of a diffractively produced vector meson or the negative four momentum transfer squared at the proton vertex, t.

Diffractive vector meson production with a large momentum transfer at the proton vertex provides a powerful means to probe the structure of the diffractive exchange. The large value of $|t|$ supplies the necessary hard scale to investigate the application of pQCD calculations. This thesis studies the diffractive photoproduction of ρ mesons, $\gamma p \to \rho Y$, where Y represents a dissociated proton system, in just such a region of high $|t|$, the ρ meson being identified by its subsequent decay into two pions. The cross section is measured differentially in t and the helicity structure of the interaction studied via an analysis of the angular decay distributions. This analysis is the first measurement of the the ρ meson at high $|t|$ to be performed by the H1 Collaboration. The results have been accepted as preliminary by the H1 Collaboration and were presented at the DIS 2005 [5] and Low x 2005 [6] workshops.

This thesis begins with a description of the HERA accelerator and the H1 detector in chapter 2, concentrating on the detector components used in this analysis. Chapter 3 introduces the relevant ep physics, beginning with deep inelastic scattering and then concentrating on low–x phenomenology and the photoproduction regime. A brief introduction to diffraction and a fuller discussion of diffractive vector meson

production is given in chapter 4. Chapter 5 details the data reconstruction and the procedure used to select diffractive ρ events. Chapter 6 describes the method used to correct the data and determine the final cross sections. This includes a study of the invariant mass distribution of the two decay pions. The results of the analysis are presented and discussed in chapter 7. Finally, chapter 8 summarises.

Chapter 2

The H1 Experiment at HERA

The H1 detector is one of two multi-purpose detectors situated on the HERA (Hadron-Elektron Ring Anlage) accelerator at the DESY (Deutches Elektronen Synchrotron) laboratory in Hamburg, Germany. This chapter begins by giving a brief description of HERA and an overview of the H1 detector. It then goes on to give a more detailed description of the individual detector components and data acquisition system, with emphasis on those aspects having particular relevance to this analysis.

2.1 The HERA Accelerator

HERA (figure 2.1) consists of two concentric storage rings, each having a circumference of 6.3 km. One of these rings accelerates protons to 920 GeV[1], while the other accelerates electrons[2] to 27.6 GeV. The beams are brought into collision, with a centre of mass energy of approximately 320 GeV, at two interaction points, where

[1]Before 1998 the proton beam energy was 820 GeV.

[2]HERA is able to accelerate both electrons and positrons. Since no distinction is necessary in this analysis, the term electron will be used generically to refer to both electrons and positrons.

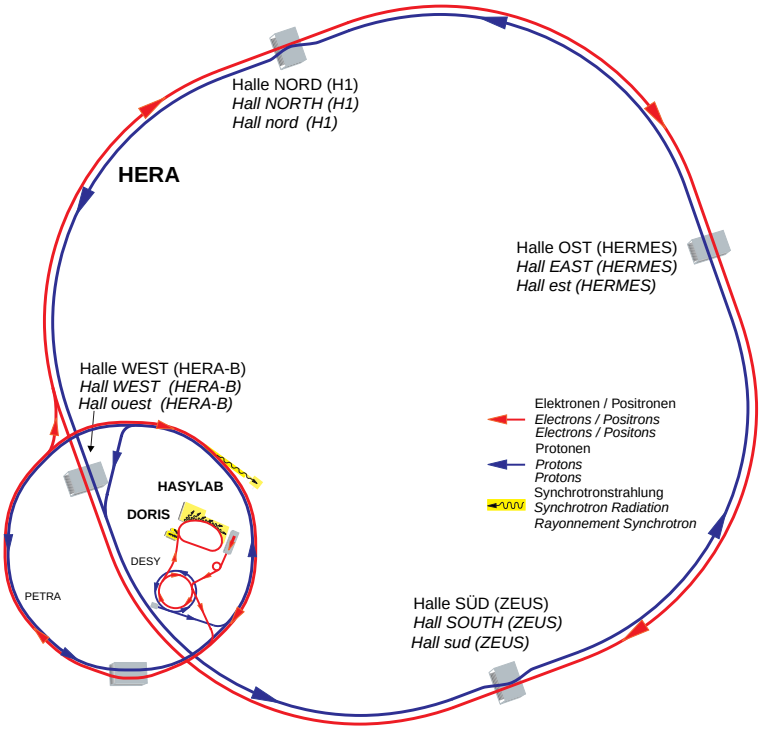

Figure 2.1: *An overview of the HERA accelerator and its pre-accelerator complex.*

the interaction products are detected by the H1 and ZEUS detectors. Due to the imbalance in the beam energies, both detectors are asymmetric with optimisation of the forward direction (that of the incoming proton beam) to reconstruct hadronic final states of high multiplicity and the backward direction (opposite to that of the incoming proton beam) to detect the scattered electron.

The beams are both divided into up to 220 bunches and typically have currents of 70 mA for the protons and 20 mA for the electrons over the 2000 data taking period considered here. These bunches are brought into collision at the interaction point every 96 ns. However, typically only 170 bunches collide with a counterpart in the other beam, while the remainder, known as pilot bunches, are filled only for a single beam and arrive at the interaction point alone. The pilot bunches are used to study the rate of background interactions occurring between the beam and the beam pipe (beam-wall), and between the beam and the residual gas within the beam pipe (beam-gas).

2.2 An Overview of the H1 Detector

The H1 detector[3] [8], shown in figure 2.2, is a nearly hermetic detector located around the northern interaction point of the HERA accelerator. It weighs about 2800 tonnes and has dimensions of approximately 12 m $\times$ 10 m $\times$ 15 m. The unequal beam energies cause the centre of mass of the ep system to be boosted in the forward direction and this is reflected in the strongly asymmetric design of the detector, which is both more highly instrumented and segmented in the forward region.

Detection and measurement of the interaction products relies mainly on a combination of tracking and calorimetry. Tracking detectors (section 2.3) lying immediately outside the beam pipe produce precise position measurements that allow the paths of charged particles passing through them to be measured. The surrounding calorimeter (section 2.4) is finely segmented to measure both the total energy deposition and the shape of the deposition, which provides information on the nature of the incident particle. These components are encased in a superconducting coil producing a 1.15 T magnetic field, which allows measurement of particle momentum and charge from the curvature of the track traced out. Muons and any hadrons that pass through the hadronic calorimeter are detected in the instrumented iron return yoke of the magnet (section 2.5). Particles scattered at low angles can be detected by further instrumentation (not depicted in figure 2.2) placed along the beam pipe in both directions. The detectors in the electron direction (section 2.7) provide luminosity measurement and are also able to detect electrons scattered through very small angles, which is of particular importance for this analysis.

Points within the H1 detector are described by means of a right handed Cartesian coordinate system with the origin centred on the nominal interaction point. The

[3]The H1 detector is described as it was during 2000, when the data analysed in this thesis were collected. It has since undergone a major upgrade [7].

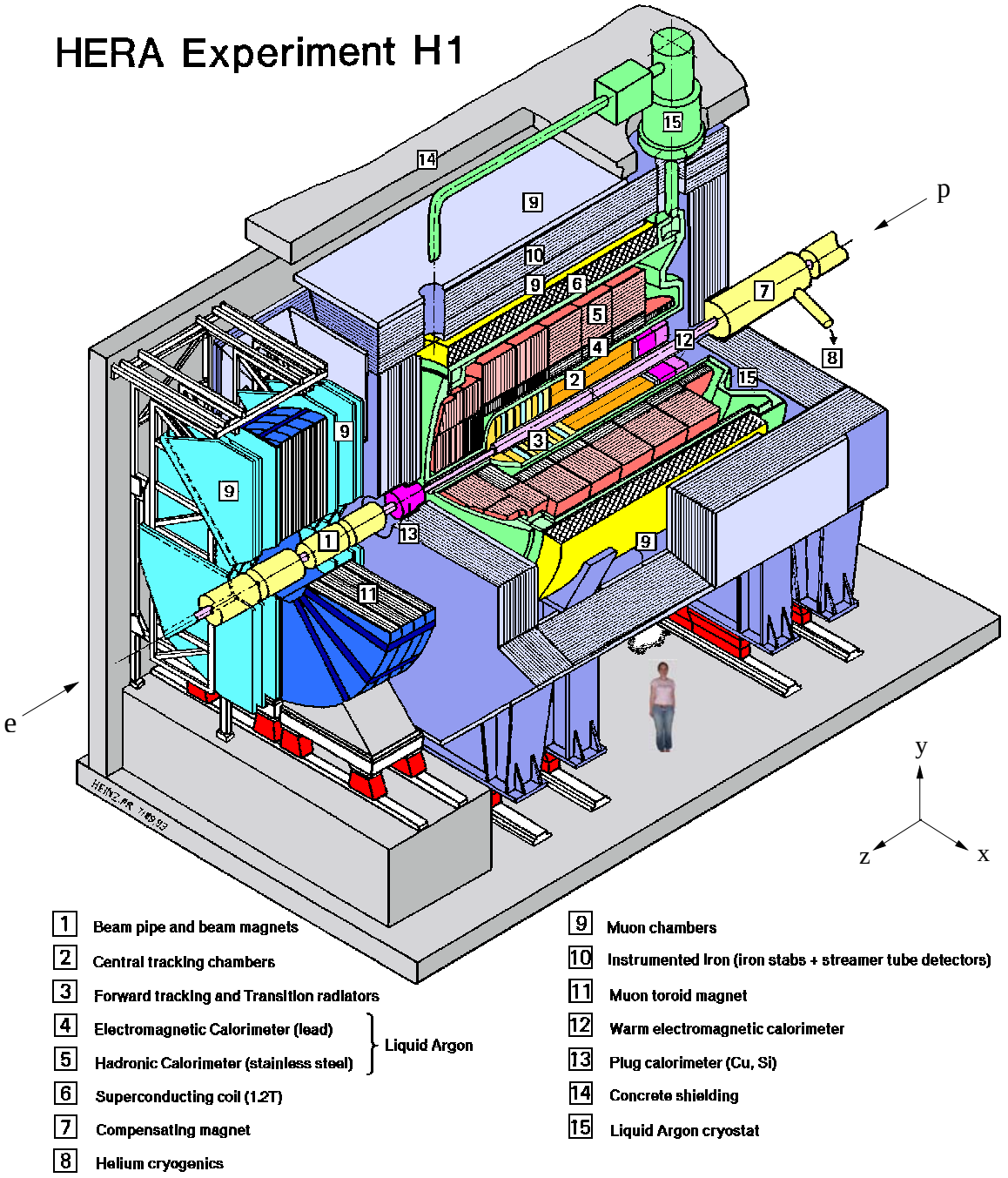

Figure 2.2: *A schematic view of the H1 Detector.*

positive z direction is defined by the incoming proton beam and the positive x direction points towards the centre of the HERA ring. Simultaneously, a spherical coordinate system is defined with θ and ϕ measured relative to the $+z$ and $+x$ axes respectively. Often a more useful variable is the pseudorapidity, η, which is defined as

$$\eta = -\ln \tan\left(\frac{\theta}{2}\right) \tag{2.1}$$

In the limit of negligible particle mass this approximates to the true rapidity, Y:

$$Y = \frac{1}{2}\ln\left(\frac{E + P_z}{E - P_z}\right) \tag{2.2}$$

where E and p_z are the energy and longitudinal momentum of the particle, respectively.

2.3 Tracking

The H1 tracking system is shown in figure 2.3. Due to the asymmetric nature of the beam, it is divided into two main sections: the forward tracking detector (FTD) and the central tracking detector (CTD). Track reconstruction is based mainly on drift chambers, while additional fast trigger information is afforded by multiwire proportional chambers.

The bulk of the CTD consists of two drift chambers, the central jet chamber one (CJC1) and two (CJC2). These are augmented by two thinner drift chambers to provide a more accurate measurement of the z coordinate, the central inner (CIZ) and central outer (COZ) z-chambers, and two multiwire proportional chambers to provide fast trigger signals, the central inner (CIP) and central outer (COP) proportional chambers. The FTD consists of three supermodules based on drift chambers, multiwire proportional chambers and transition radiators. In the backward direction tracks are reconstructed in the backward drift chamber (BDC). In the central and backward regions more precise vertex information is provided by silicon trackers, the

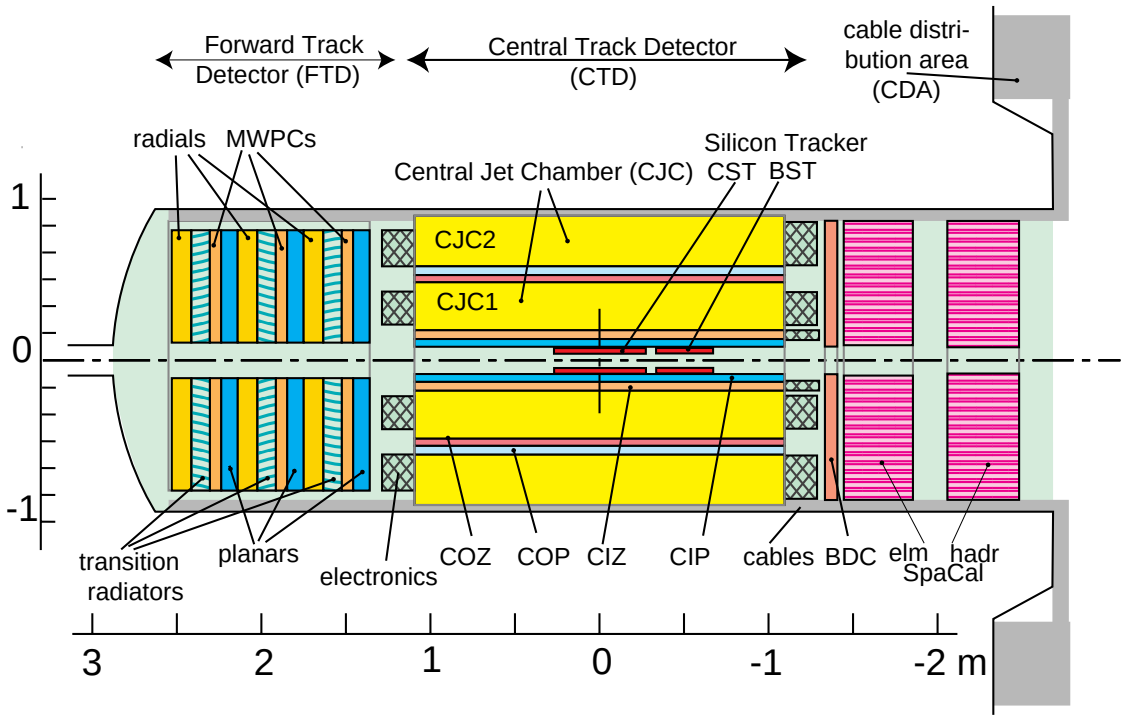

Figure 2.3: *A cross sectional view of the H1 Tracking System, showing the central, forward and silicon trackers and the BDC.*

central silicon tracker (CST) and the backward silicon tracker (BST), lying adjacent to the beam pipe. Further information on these detectors can be found in [9,10].

Drift chambers consist of many separate gas-filled cells, each of which contain a set of field wires (cathodes) and sense wires (anodes). Additional field shaping wires ensure the majority of each cell is subject to a nearly uniform electric field. A charged particle traversing a cell ionises some of the gas molecules. The resulting positively charged ions drift towards the cathode wires and the electrons drift towards the anode wires, at a well known velocity. Once close to the sense wire (< 1 mm), the electrons experience a rapidly increasing electric field, causing them to produce an avalanche of secondary ionisation. This induces a current in the sense wire. The time at which the current pulse occurs, coupled with a knowledge of the electron drift velocity, allows the closest distance of approach of the incident particle to the wire to be accurately determined. Drift distances can typically be resolved to a few

hundred μm. The movement of the ions also induces a current in the sense wire. Although this pulse is typically much larger than the corresponding electron pulse, it is not used for timing information due to the slower drift velocity of the ions. Measurement of the pulse at both ends of the wire enables the position of the signal along the wire to be estimated by charge division, with a typical resolution of 1% of the wire length. The combination of the space points produced by each sense wire allow the path of the incident particle to be traced out.

Multiwire proportional chambers (MWPCs) are similar to drift chambers, consisting of gas-filled cells containing very closely strung anode wires ($\sim$ 1 mm apart) and cathode pads around the outside of the cell. The closeness of the anode wires causes the avalanche regions to overlap and results in rapid amplification of the initial ionisation. The charge produced is collected by a single anode wire and remains proportional to the initial ionisation. The spatial resolution is limited to the separation of the anode wires but the absence of any large drift region significantly improves the readout time and allows fast position information to be determined, which is essential for effective triggering.

2.3.1 The Central Track Detector

The CTD consists of a set of concentric cylindrical detectors, which are shown in cross section in figure 2.4. The inner detectors, CIZ and CIP, are located inside the inner jet chamber, CJC1, while the outer detectors, COZ and COP, are sandwiched between CJC1 and CJC2. It extends over a radial distance of $150 < r < 850$ mm and covers the angular range $15^\circ < \theta < 165^\circ$.

CJC1 and CJC2 [11] consist of 56 wires running parallel to the beam pipe to produce a drift field in the $r-\phi$ plane. Typical drift velocities are around 50 mm/μs, resulting in a spatial resolution of 170 μm in this plane. The individual cells are tilted by 30° such that ionisation electrons drift almost perpendicular to high momentum

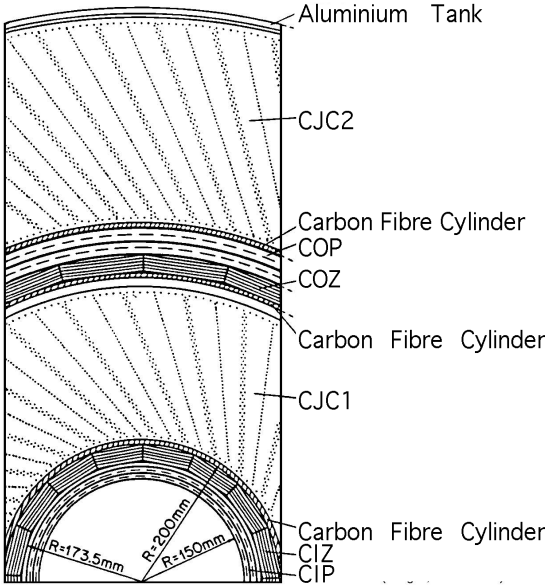

Figure 2.4: *A cross sectional view, in the $r-\phi$ plane, of the Central Track Detector [8].*

tracks, providing optimal resolution. A further advantage of this angular offset is the ability to resolve reconstruction ambiguities by connecting track segments from different cells. The z coordinate of the track is only accessible via charge division, leading to a poorer resolution of 22 mm.

The CIZ and COZ [12] provide improved measurement in the z direction by having the sense wire orientated in the azimuthal plane. The resulting drift field is parallel to the beam pipe and allows measurement of the z coordinate from the drift time with an accuracy of 300 μm. The combined track measurements afforded by the four central drift chambers give a design momentum resolution of[4] $\sigma p/p^2 = 3 \times 10^{-3}$ GeV^{-1} [8].

The CIP and COP [13] are MWPCs, each consisting of a double layer of drift chambers with sense wires along the z direction. The CIP is divided into 60 pads in z with each pad being divided into 8 sections in ϕ. The COP is similar, except

[4]Throughout this thesis a system of natural units is used whereby $\hbar = c = 1$.

that there are 18 pads in z separated into 16 ϕ sectors. They deliver fast timing information over the full central range, essential for providing trigger information within the 96 ns bunch crossing interval. Their principal use is the z-vertex trigger, which is described in section 2.8.1. Additionally, they provide extra coverage in the backward direction where the CJCs no longer provide sufficient space points.

2.3.2 The Forward Track Detector

Track reconstruction in the forward region for $5° \leq \theta \leq 30°$ is provided by the FTD [14], shown on the left-hand side of figure 2.3. Each supermodule comprises of, in increasing z, layers of planar drift chambers, MWPCs, transition radiators (TRs) and layers of radial drift chambers, as shown in figure 2.5. The planar chambers consist of parallel sense wires strung in a plane perpendicular to the beam pipe, to provide an accurate measurement of the polar angle θ. Within each supermodule, the planar chambers are arranged in three groups lying at angles of 0°, +60° and −60°, in order to improve spatial resolution. The TRs produce transition radiation photons, which are detected in the neighbouring radial chamber. The radial chambers (containing radially orientated sense wires) supply an accurate determination of the azimuthal angle ϕ via drift time measurements and a fair radial position through charge division. The FTD has an overall momentum and angular resolution of better than $\sigma_p/p = 0.03$ GeV^{-1} and $\sigma_{\theta,\phi} = 1$ mrad respectively.

2.3.3 The Backward Drift Chamber

The BDC [15], shown on the right-hand side of figure 2.3, is located in front of the SpaCal calorimeter and provides additional information on electrons scattered through small angles. It consists of four pairs of octagonal layers containing radially strung wires, which are used for electron identification in the backward direction.

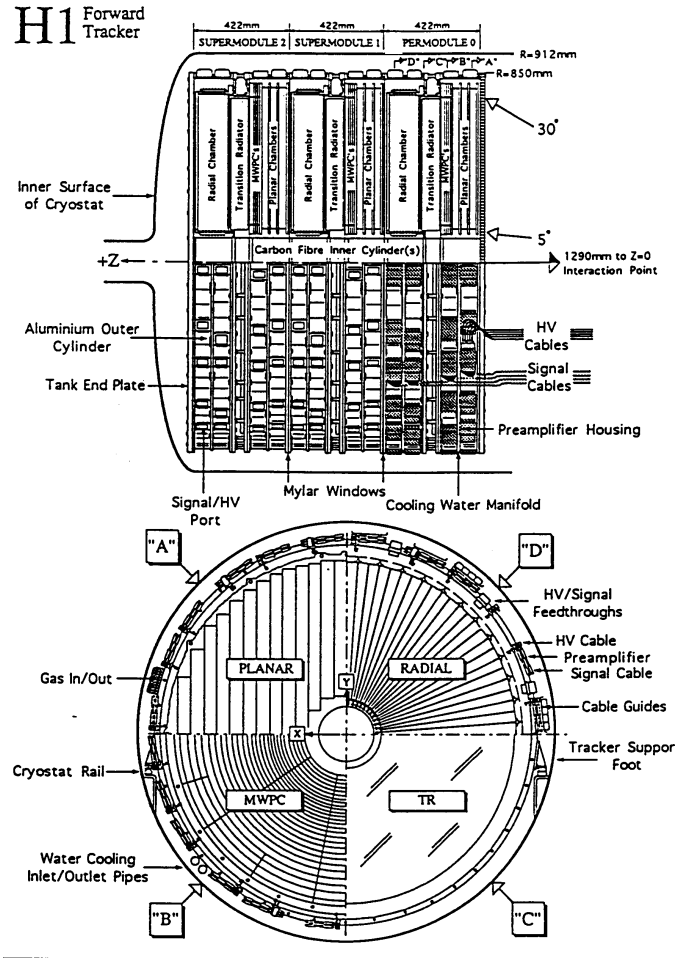

Figure 2.5: *A single supermodule of the FTD [8]. The $r-z$ view (top) shows the different components which make up a supermodule and the $r-\phi$ view (bottom) shows the basic structure of each component.*

2.4 Calorimetry

All calorimetry in H1 is provided by means of sampling calorimeters. Such calorimeters consist of absorbing (passive) layers interspersed with sampling (active) layers. Incident particles undergo multiple interactions with the absorber material, producing secondary particles which subsequently interact with further layers of absorber to form a shower. The energy of the shower, which is proportional to the energy of the incident particle if the shower is fully contained, is measured through ionisation

of the atoms in the sampling layer.

Electromagnetic particles, such as electrons and photons, lose energy via pair production or bremsstrahlung within the electric field provided by the absorber nuclei. The resulting particles undergo further interactions, causing a shower to propagate. The propagation of an electromagnetic particle through an absorbing layer is governed by the radiation length, X_0, which is the mean distance over which $1/e$ of the particle's original energy is lost. For lead, a typical absorber material, the radiation length is 0.56 cm.

Strongly interacting particles, such as hadrons, undergo both elastic and inelastic scattering with the absorber nuclei. Again, a shower develops, which continues until the particle's energy is sufficiently low that it can be stopped by ionisation or nuclear capture. Much of the energy in a hadronic shower is lost due to excitation or break up of the absorbing nucleus. In the case of strongly interacting particles, the characteristic length is the interaction length, λ. This is usually much larger than X_0, being approximately 17 cm for lead, leading to a longer hadronic shower. Hadronic showers are also broader due to the Coulomb scattering of secondary charged particles, mainly pions. Further, the decay of secondary neutral pions $\pi \to \gamma\gamma$ adds a prompt electromagnetic component to hadronic showers. Based on their different geometries, the two shower types can be distinguished, facilitating offline correction of the hadronic showers for energy loss.

The different components of the H1 calorimetry are summarised in figure 2.6. The main coverage is provided by the liquid argon (LAr) calorimeter (section 2.4.1) in the forward and central regions and the spaghetti calorimeter, or SpaCal, (section 2.4.2) in the backward direction. The gap between the forward edge of the LAr and the beam pipe ($0.6^\circ < \theta < 3.5^\circ$) is closed by the plug calorimeter (PLUG), which is a compact calorimeter designed mainly to minimise the missing transverse momentum and veto forward activity. Energy from hadronic showers leaking out of the LAr can be coarsely measured in the tail catcher. This is formed

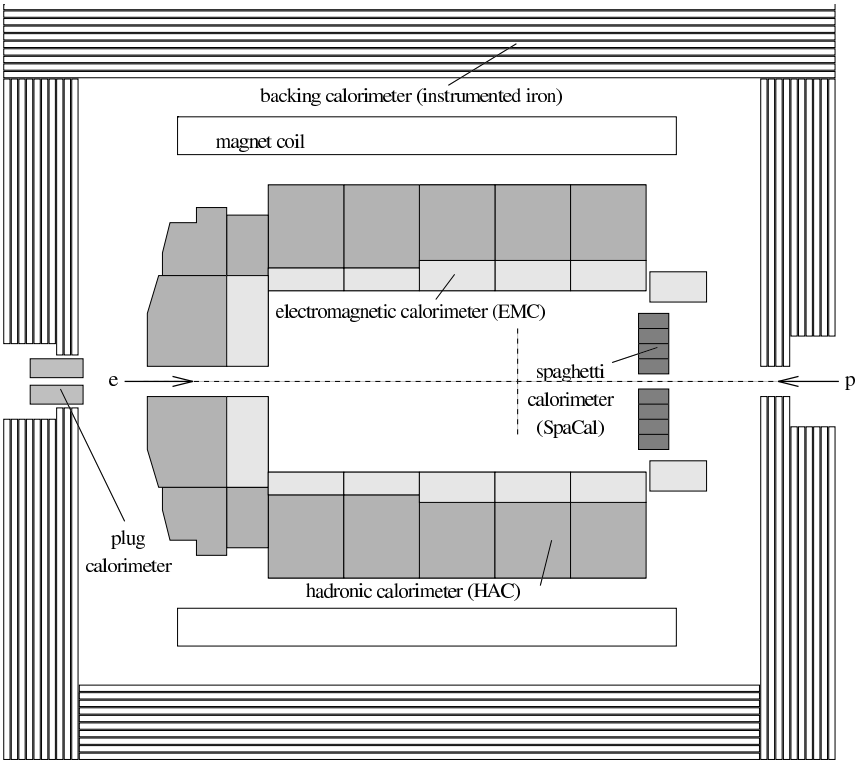

Figure 2.6: *An overview of the H1 calorimetry in the $r-z$ plane.*

from 11 of the 16 layers of limited streamer tubes (LSTs) which instrument the iron return yoke of the H1 magnet.

2.4.1 The Liquid Argon Calorimeter

The main purpose of the LAr calorimeter [16] is to detect the hadronic final state (HFS) and identify the scattered electron in high Q^2 (> 100 GeV^2) events[5]. To do this it provides full azimuthal coverage over the polar range $4^\circ < \theta < 154^\circ$ (corresponding to $-1.43 < \eta < 3.35$). The LAr comprises an inner electromagnetic part (EMC) and an outer hadronic part (HAC), housed within a single liquid argon cryostat. As shown in figure 2.7, it is split into eight wheels along the z axis, each

[5] Q^2 is the modulus squared of the four momentum transferred at the electron vertex (see section 3.1 for further details).

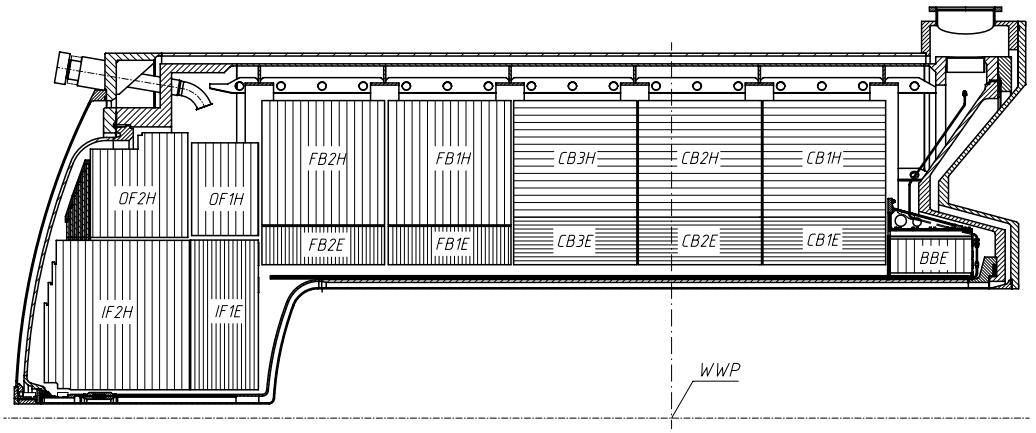

Figure 2.7: *An $r-z$ view of the upper section of the liquid argon calorimeter [8]. The interaction point (Wechselwirkungspunkt) is represented by WWP.*

containing eight azimuthal octants.

Both the EMC and the HAC use liquid argon as the active material as its high atomic density produces high ionisation, while its inert nature suppresses secondary inelastic scattering of the ionisation products. In the former case the absorbing layer is provided by 2.4 mm lead plates, whereas 19 mm stainless steel is used in the latter case. The asymmetric nature of the beams is reflected in the thickness of the LAr calorimeter, which decreases from 30 X_0 (EMC) and 8 λ (HAC) in the forward region to 20 X_0 (EMC) and 5 λ (HAC) in the backward region.

The LAr consists of 45 000 individual readout channels, providing a fine granularity which is almost uniform in η and ϕ. This fine granularity provides electron-pion discrimination down to 1 part per 1000. The readout channels are grouped together to form 256 towers radiating away from the nominal interaction point. Energy sums within these towers form the basis of the LAr trigger (section 2.8.3). The LAr is a non-compensating calorimeter, i.e. it has a different response to electromagnetic and hadronic particles. In the case of hadrons the response is typically 30% less than for similar energy electrons. This difference is adjusted by reweighting the hadronic energy within the offline reconstruction software [17].

The energy[6] resolution of the LAr, as obtained in test beams, is $\frac{\sigma_E}{E} = \frac{0.12}{\sqrt{E}} \oplus 0.01$ [18] for electrons detected in the EMC and $\frac{\sigma_E}{E} = \frac{0.50}{\sqrt{E}} \oplus 0.02$ [19] for pions detected in the EMC and HAC.

2.4.2 The Spaghetti Calorimeter

The SpaCal [20] supplies precision measurements of the scattered electron in low Q^2 events ($1 \lesssim Q^2 \lesssim 100$ GeV^2) and measurements of hadronic activity in the electron direction. The discrimination between electrons and pions is better than 1 part in a hundred. The SpaCal is situated in the backward region, as shown in figure 2.8, and covers the polar range $153^\circ < \theta < 177.5^\circ$ (corresponding to $-1.43 < \eta < -3.82$). Like the LAr, it is a non-compensating sampling calorimeter, which is split up into electromagnetic and hadronic parts.

The SpaCal consists of active scintillating fibres embedded in an absorber formed from grooved lead sheets. Incident charged particles initiate showers in the lead sheets, causing the fibres to scintillate. The resulting light is read out by photomultiplier tubes, which have a time resolution of better than 1 ns. This fast response enables the SpaCal to provide additional time of flight (ToF) information (see section 2.6) and to be used for triggering purposes. Both sections are 250 mm deep, corresponding to $\approx 28X_0$ or $\approx 1\lambda$ for the electromagnetic part and a further $\approx 1\lambda$ for the hadronic part. The former consists of 0.5 mm diameter fibres, giving a lead to fibre ratio of 2.3:1, and is read out through 1192 channels. Reflecting the greater extent of hadronic showers, the latter consists of 1.0 mm diameter fibres, giving a lead to fibre ratio of 3.4:1, and is read out through 136 channels.

The energy resolution, as measured in test beams, is $\frac{\sigma_E}{E} = \frac{0.07}{\sqrt{E}} \oplus 0.01$ and $\frac{\sigma_E}{E} = \frac{0.50}{\sqrt{E}} \oplus 0.02$ for the electromagnetic [21] and hadronic [22] parts respectively. The combined energy resolution for charged pions at 4 GeV is $\frac{\sigma_E}{E} = 0.29 \pm 0.02$ [23].

[6] All energy measurements in this thesis are in GeV unless specified otherwise.

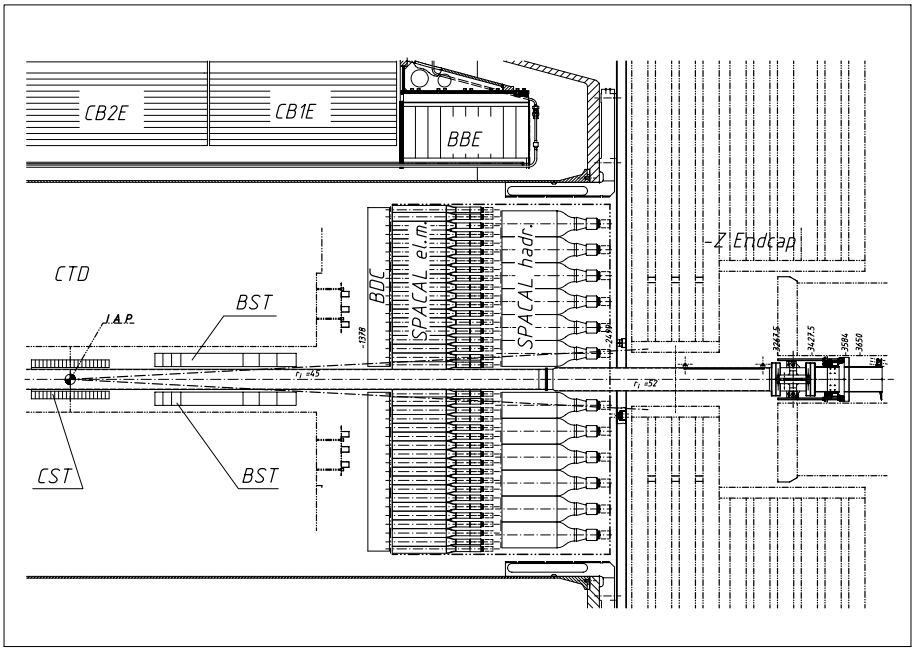

Figure 2.8: *A cross sectional view of the SpaCal in the $r - z$ plane [20]. The interaction point is represented by IAP.*

2.5 Muon Systems

Muons generally escape the calorimeters since they do not interact hadronically and their bremsstrahlung radiation is suppressed as a result of their heavier mass. Detection is provided by means of the central (CMD) and forward (FMD) muon detectors, which lie outside the main calorimeters.

2.5.1 The Central Muon Detector

The CMD is formed by the 5 remaining layers of LSTs (not utilised in the tail catcher) which make up the instrumented iron and covers an angular range of $6° < \theta < 172°$. Readout is provided by means of a metal wire strung along the centre of the LST and metal strips perpendicular to this. For a muon to be reconstructed a signal is required in at least 3/5 layers, except in the forward region

where 4/5 layers are required due to the increased particle flux. Studies of cosmic ray muons indicate a muon identification of better than 90%.

2.5.2 The Forward Muon Detector

The FMD [24] is situated in the forward region, as shown in figure 2.2, and covers the angular range $3° < \theta < 17°$. It consists of three twin layers of drift chambers either side of a 1.5 T toroidal magnet. Four of these layers have wires perpendicular to the radial direction to provide accurate measurement of the polar angle θ, while the remaining two have wires radiating out from the beam pipe to provide accurate measurement of the azimuthal angle ϕ. The FMD is also used in diffractive analyses to veto proton dissociation events by identifying the remnant particles or their secondaries, which result from interactions in the dead material.

2.6 Time of Flight System

At HERA the rate of background events, mainly due to proton beam-gas and beam-wall interactions, is over 1000 times larger than ep collisions. Particles from background reactions, which generally occur up-stream or down-stream of the interaction point, will arrive at a particular point in z at a different time than particles due to true ep events. The role of the ToF system is to provide fast timing information that can be used to reject these backgrounds. It is composed of several separate plastic scintillators positioned close to the beam pipe at various points: near the FMD (FToF), within the PLUG (PToF) and within the backward iron endcap (BToF). Additional ToF information in the backward direction is provided by the SpaCal.

Further background arises from beam-halo, a shower of particles (mainly muons) which accompany the proton beam and are produced by beam-gas or beam-wall collisions occurring far upstream. This is suppressed by a double layer of scintillators,

called the veto wall, positioned behind the backward iron end cap.

2.7 Luminosity System

A precise measurement of the luminosity is essential for cross section determination. At H1 this is provided by means of two taggers: an electron tagger (ET) and photon detector (PD) sited along the beam pipe in the electron direction at $z = -33.4$ m and $z = -102.9$ m respectively. As well as providing an absolute measurement of the offline luminosity, it provides relative online luminosity information, essential for monitoring the electron beam.

The components of the luminosity system [25] are illustrated in figure 2.9. Both the ET and PD are Čerenkov crystal calorimeters composed of 22 radiation lengths of TlCl/TlBr crystals with an energy resolution of $\frac{\sigma_E}{E} \sim \frac{0.10}{\sqrt{E}} \oplus 0.01$. The ET contains 49 crystals arranged in a 7×7 array, whereas the PD is smaller, consisting of 25 crystals in a 5×5 array. The front of the PD is shielded from the high synchrotron radiation flux by a $\sim 2X_0$ lead filter (F) and a $\sim 1X_0$ water Čerenkov veto counter (VC). The VC vetos events where the photons interact in the filter. On the proton side the protection is afforded by a 2 m thick iron wall.

The luminosity measurement is determined by the rate of the Bethe-Heitler [26] process, $ep \to ep\gamma$, which is calculable in QED to a level of 0.5 %. The principal source of background is due to electron beam-gas interactions, $eA \to eA\gamma$, which can be estimated from pilot bunch data. The online measurement is determined by detecting the scattered electron in the ET in coincidence with a photon in the PD, with an energy sum close to the incoming electron beam energy. The acceptance of the ET is highly dependent on the run-by-run beam tilt, which is not easily simulated, and this gives rise to the largest systematic error.

The offline measurement is determined by the rate of photons with energy above

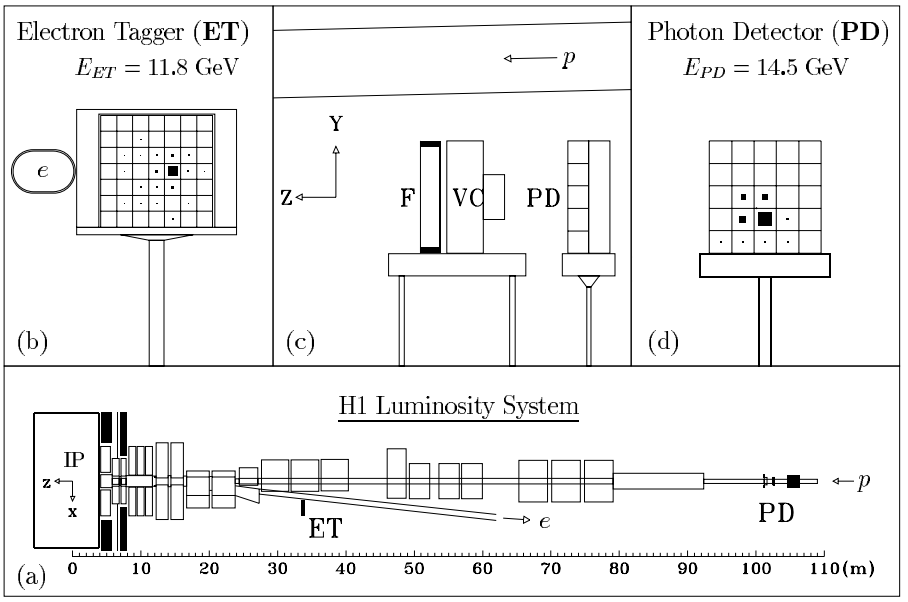

Figure 2.9: *An overview of the luminosity system [8] showing: (a) the positions of the electron tagger (ET) and photon detector (PD) in z, relative to the interaction point (IP), (b) a cross section of the ET, (c) a side view of the PD shielded by the lead filter (F) and water Čerenkov detector (VC) and (d) a cross section of the PD.*

a certain threshold (typically 10 GeV) entering the PD. This reduces the systematic effects, as the acceptance for photons is much less dependent on the beam optics. A further correction of up to 10% is applied to account for the proton current contained within satellite bunches which accompany the proton beam. The final offline luminosity is accurate to 1.5% for the data considered here [27].

The ET is also used to detect the scattered electron at small angles in low Q^2 events (< 0.01 GeV^2). This is aided by further taggers at -8.0 m (ET8) and -43.2 m (ET44), each of which covers a slightly different kinematic range. The ET44 is similar to the ET, consisting of 6 $NaBi(WO_4)_2$ crystals in a 2×3 array, whereas the ET8 is a SpaCal-type electromagnetic calorimeter. Due to the small size of the ET44, the energy deposited by the scattered electron is never fully contained within the calorimeter, leading to a poor energy resolution [28]. In 1995, the energy

	ET	PD	ET44
Material	TlCl(78%) + TlBr(22%)		$NaBi(WO_4)_2$
Size (mm)	154 × 154	100 × 100	44 × 66
Granularity	7 × 7	5 × 5	2 × 3
Crystal depth (cm)	20		
Radiation length X_0 (cm)	0.92		1.03
Moliere radius R_M (cm)	2.08		2.38
Energy resolution $\sigma E/E$	$0.1/\sqrt{E} \oplus 0.01$		$0.2/\sqrt{E} \oplus 0.01$
Acceptance in y[a]	0.2-0.8		0.04-0.24

[a] y is the fractional energy loss at the electron vertex (see section 3.1 for further details).

Table 2.1: *A summary of the luminosity system and ET44 properties.*

resolution was measured to be $\frac{\sigma_E}{E} \sim \frac{0.20}{\sqrt{E}} \oplus 0.01$, but it is known to have degraded significantly since then. The ET44 forms a key component of the trigger used to identify the events in this analysis and its properties, in relation to those of the ET and PD, are summarised in table 2.1.

2.8 Triggering and Data Acquisition

HERA currently has the highest bunch crossing rate of any collider, with a crossing occurring every 96 ns (10.4 MHz). The challenge is to determine true ep collisions from a background which is a factor of 1000 times larger. Even modern electronics cannot process the full $\sim$ 270000 channels of detector information in the time between bunch crossings. In order to avoid the otherwise unacceptable deadtime, H1 utilises a pipelined four level trigger system: L1, L2, L4 and L5[7]. L1 and L2 are

[7]L3 is not yet implemented but will be used in future for the new fast track trigger (FTT) [29].

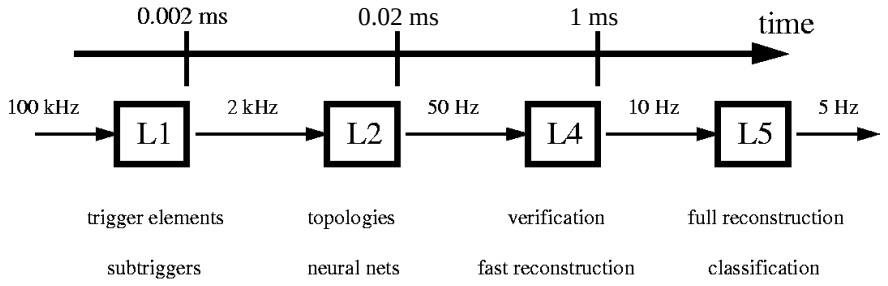

Figure 2.10: *An outline of the trigger system showing the approximate rates and decision times at each stage.*

online hardware triggers, while L4 is an offline software trigger and L5 is an offline event classification. The trigger system is outlined in figure 2.10.

At each bunch crossing, all the H1 detector components send data, called trigger elements, to the central trigger (CTL1) [30]. The L1 trigger, shown in figure 2.11, combines the 192 individual trigger elements into 128 subtriggers and then, based on these, makes a decision on whether the event is interesting in ≈ 2.3 μs (i.e. ~ 24 bunch crossings). During this time the information for all ~ 24 bunches is stored in a pipeline in order to allow deadtime free operation. If an event fires one (or more) of the subtriggers, an L1Keep signal is sent to CTL1, the pipeline is frozen and the information is passed to L2. Events that are not kept fall off the end of the pipeline. Due to the limited readout capacity, subtriggers with a high rate must be prescaled to prevent them swamping the system's bandwidth at the expense of other subtriggers. This means that only 1 in P of the events is kept, where P is the prescale factor of that subtrigger. Information on both those events which fire a subtrigger and those events which are actually saved after prescaling is stored separately. L1 reduces the input rate, ~ 100 kHz, by a factor of roughly 50.

The L2 trigger consists of a set of topological triggers (L2TT) [31] and neural networks (L2NN) [32], which make decisions based on the correlations between the different subtriggers in a time of ~ 20 μs. In the former, decisions are made based

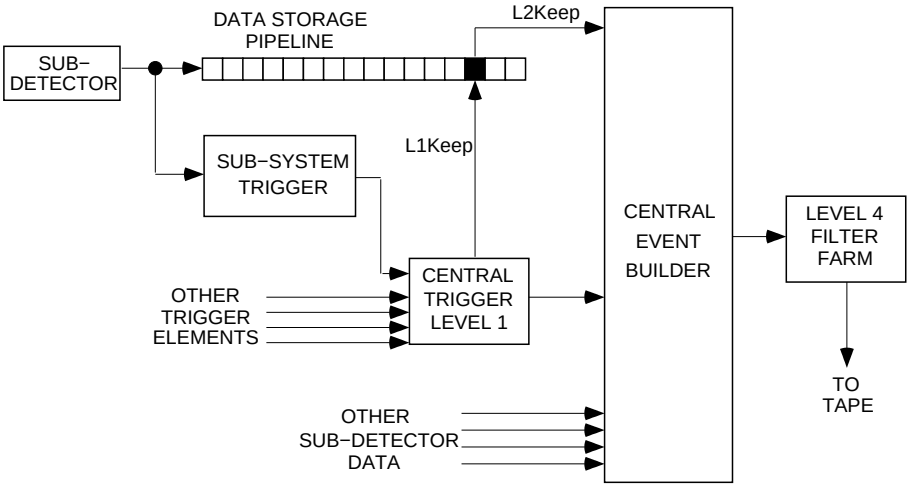

Figure 2.11: *A schematic view of the L1 and L4 trigger systems.*

on topological features of particular final states, while, in the latter, distinctive physics channels are separated from the background. L2 sends an L2Keep signal that validates the L1 decision and causes the entire event to be read out to the central event builder (CEB) and subsequently the L4 trigger. This process freezes the pipeline for ~ 1 ms, causing a deadtime of 10% on average. Through this level the rate is further reduced to $\sim$ 50 Hz, which is the input limit of L4 to avoid deadtime.

L4 is an asynchronous software trigger consisting of a farm of approximately 30 PCs. It performs limited reconstruction of each event and applies further, often complex, cuts depending on the combination of subtriggers fired. The majority of the remaining background, such as beam-gas and beam-wall interactions, is rejected at this stage and the remaining data is written to tape at a rate of ~ 10 Hz. In order to reduce the volume of data, some high rate physics processes are downscaled at L4. This involves saving only a fraction of events, which are then assigned an L4 weight in such a way such that a statistically accurate representation of the original data can be reconstructed. In order to identify which processes should be downscaled, and avoid downscaling high priority events, algorithms to select particular final states, known as finders, are implemented.

The data is then passed to a dedicated computer farm which constitutes the offline L5 trigger. Here, the events are fully reconstructed, using all individual subdetectors, and classified according to their physics content. This is performed by the `H1REC` software package [33]. The full events are then written to production output tapes (POTs), while a compressed version (typically 10 kB/event), containing the information sufficient for most physics analyses, is written to data summary tapes (DSTs).

The following sections describe the main trigger elements that make up the subtrigger used in this analysis.

2.8.1 The z-Vertex Trigger

The z-vertex trigger [34] removes non-ep interactions using fast track reconstruction provided by the CIP and COP, along with a MWPC in the first supermodule of the FTD (FPC). The trigger splits the detector up into 16 ϕ segments, as shown in figure 2.12(a). Within each segment, coincident hits in two out of the three components are used to define rays pointing back to the z-axis. The z coordinate of the intercept of each ray with the z-axis is entered into a 16-bin histogram which covers the range $|z| < 44$ cm. This process is illustrated in figure 2.12(b) for a single ϕ segment. The individual histograms for each segment are then combined into a single z-vertex histogram. A true ep event will produce a peak at the nominal interaction point, while wrongly identified rays give rise to a flat background. Various L1 trigger elements can then be defined by placing cuts on this histogram. In particular, the zVtx_Cls trigger element requires that all entries in the histogram (neglecting the two outermost bins at each edge) lie within four neighbouring bins [35].

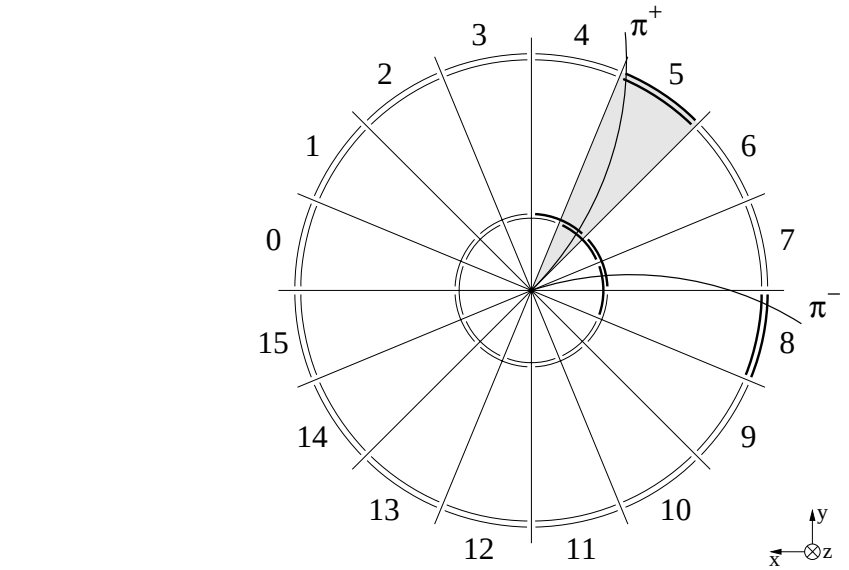

(a)

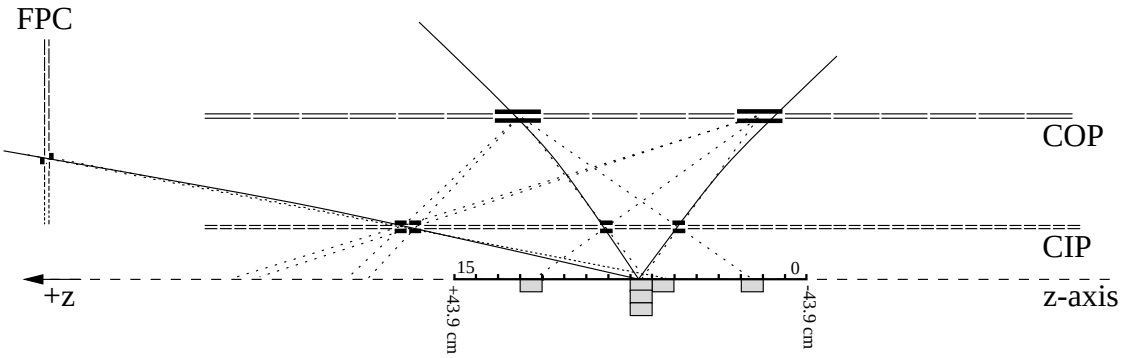

(b)

Figure 2.12: *An overview of the principle of operation of the z-vertex trigger in (a) $r-\phi$ and (b) $r-z$ view [35]. The filling of the z-vertex histogram for a single ϕ segment is illustrated schematically in (b), with genuine rays shown as full lines and wrongly identified ones as dotted lines.*

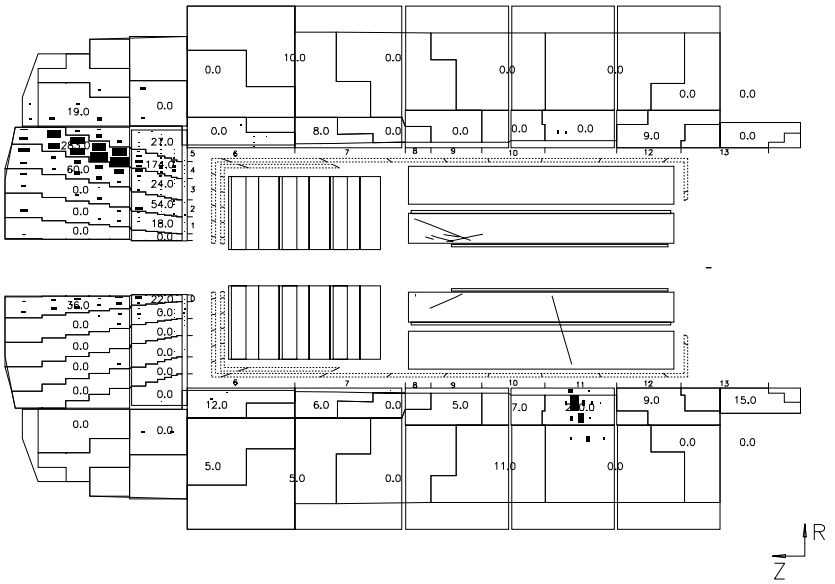

Figure 2.13: *An outline of the LAr big tower (BT) geometry with a neutral current (NC) event overlaid [8].*

2.8.2 The DCRϕ Trigger

The DCRϕ trigger [36] compares hits in 10 out of the 56 wire layers comprising the CJC to predefined masks, based on track position and curvature, in order to provide limited track information in the $r-\phi$ plane. Only charged particles with transverse momentum, p_t, above 0.4 GeV are able to fire the trigger. Several trigger elements are defined based on the track multiplicity, the sign of the charge and the transverse momentum. In particular, DCRPh_Ta requires that one or more track candidates exist. To reduce non-ep background, the DCRϕ trigger is only sensitive to those tracks whose closest distance of approach to the beam pipe is less than 2 cm.

2.8.3 The LAr Trigger

As mentioned earlier, the LAr readout channels are grouped into 256 towers, called big towers (BT), radiating out from the interaction vertex. This is depicted in figure 2.13. The LAr trigger forms several trigger elements by placing requirements

on the sum of the electromagnetic and hadronic energy within BTs in various regions of the LAr. In the case of LAr_IF it is the BTs lying in the inner forward (IF) region, which covers the polar angular range $4 < \theta < 20°$, that are summed. Thus, !LAr_IF[8] requires that there be no energy deposits, above noise level (~ 2 GeV), detected in this region [37].

2.8.4 The 44 m Electron Tagger Trigger

The etag_44 trigger requires an energy deposit of greater then 10 GeV in ET44 along with a veto on there being no signal in the PD, above 6 GeV, or the VC.

2.9 Monte Carlo Simulation

In order for the data produced at H1 to be fairly compared to data from other experiments and theoretical predictions, the acceptance and resolution effects of the H1 detector must be understood and corrected for. This is performed using a simulation based on Monte Carlo (MC) techniques, whereby particular physics models are simulated using probability distributions and random numbers.

This simulation is performed in two distinct stages. Firstly, an event generator is used to compile a list of all particles produced by a particular interaction, based on all allowed Feynman diagrams and probability density functions. Fragmentation and hadronisation models are used to further evolve any short lived states into stable particles. Each event then consists of a list of four vectors describing these final state particles. This stage produces the generator level (gen) information. In this analysis, the DIFFVM [38] event generator (see section 5.2) is used to simulate both the signal and background processes.

[8]The symbol ! indicates a logical NOT.

The interaction of the particles with the detector is then simulated using the `H1SIM` package, which models the H1 detector using the GEANT3 framework [39]. The simulation is updated to include information on any damage caused to the detector, such as broken wires within the drift chambers. This stage produces the reconstructed (rec) level information. Once passed through the reconstruction software, `H1REC`, this information can be directly compared with the data. Provided the data is reliably described by the reconstructed level information, it can be corrected using correction factors obtained from the differences between the two levels of simulation.

Chapter 3

HERA Physics

This chapter presents an introduction to ep physics. Firstly, a brief overview of deep inelastic scattering (DIS) is given, focusing on the low x regime relevant to HERA. In this process the electron is able to probe the structure of the proton. This is followed by a discussion of the photon structure in the photoproduction limit, where the exchanged photon is almost real, with particular attention to the vector meson dominance model (VDM). A more comprehensive review of diffractive physics is given in chapter 4.

3.1 DIS Kinematics

DIS, depicted in figure 3.1, is mediated by the exchange of an electroweak boson which interacts with a single point-like constituent of the proton, known as a parton. This boson can be either a photon or Z^0, leading to the neutral current (NC) process $ep \to eX$, or a $W^{\pm}$, leading to the charged current (CC) process $ep \to \nu_e X$. Since the propagator term in the amplitude varies with the boson mass, M, as $\sim 1/(Q^2 + M^2)$, the NC cross section is dominated by photon exchange except at the highest Q^2 ($Q^2 \gtrsim M_{Z^0}^2 \sim 10^4$ GeV^2). By the same rationale, the NC cross

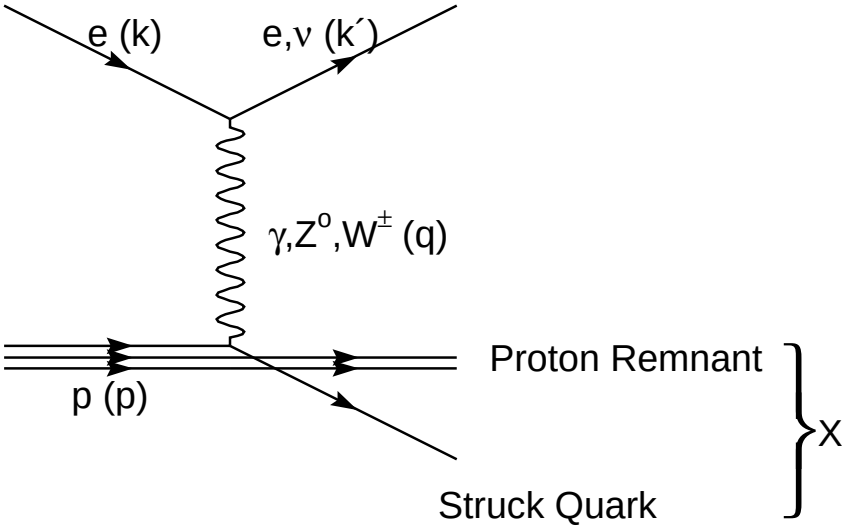

Figure 3.1: *DIS process at the Born level.*

section dominates over the CC cross section for most of the HERA kinematic regime, being up to three orders of magnitude larger at the lowest Q^2. Only at the scale of electroweak unification $Q^2 \gtrsim M_{Z^0}^2, M_W^2$ do the cross sections become similar, as illustrated in figure 3.2.

The kinematics of a DIS interaction are described by Lorentz invariant combinations of the four vectors defined in figure 3.1. The square of the four momentum transferred,

$$Q^2 = -q^2 = -(k - k')^2, \tag{3.1}$$

defines the virtuality of the exchanged photon and provides a measure of its spatial resolving power. In the case of DIS, where $Q^2 \gtrsim 1$ GeV^2, the wavelength of the virtual photon is short enough to probe the internal structure of the proton. For $Q^2 \ll 1$ GeV^2 the photon is almost real, i.e. on mass shell, and gives rise to the kinematic regime known as photoproduction (see section 3.4). The *ep* centre of mass (CoM) energy squared of the interaction is given by

$$s = (k + p)^2 \tag{3.2}$$

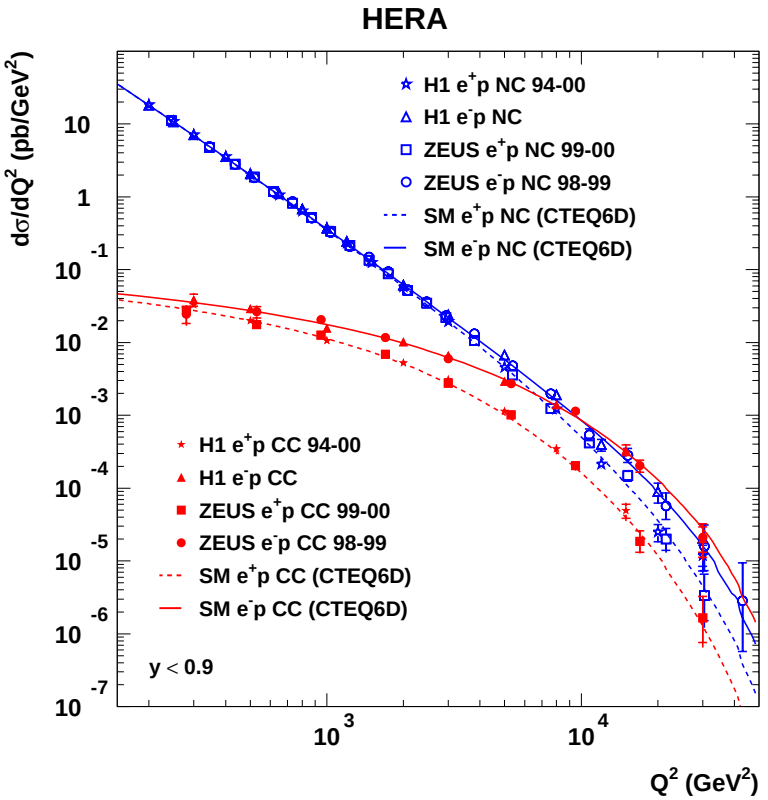

Figure 3.2: *The neutral and charged current cross sections as a function of Q^2 [40].*

and has the value 101 200 GeV^2 for the data used in this analysis. Additionally, by excluding the scattered electron, the reaction can be described in terms of the photon-proton centre of mass energy squared,

$$W^2 = (q + p)^2. \tag{3.3}$$

The dimensionless Bjorken scaling variable, x, is defined as

$$x = \frac{Q^2}{2p \cdot q} \tag{3.4}$$

and can be interpreted as the fraction of the proton's momentum carried by the struck parton in the limit that it is both massless and carries no transverse momentum. A further Bjorken scaling variable

$$y = \frac{p \cdot q}{p \cdot k} \tag{3.5}$$

describes the fraction of the electron energy carried by the exchanged photon in the rest frame of the proton. At fixed s, the interaction can be fully described by two independent quantities which, in the limit of massless incoming particles, are related by

$$Q^2 = sxy \tag{3.6}$$

$$W^2 = Q^2 \left(\frac{1-x}{x} \right). \tag{3.7}$$

3.2 Structure of the Proton

The unknown structure of the proton can be described, in the most general way compatible with relativistic invariance, in terms of two[1] structure functions, $F_1(x, Q^2)$ and $F_2(x, Q^2)$, which are dependent on the electric charge distributions within the proton[2]. The total differential electromagnetic cross section $ep \to eX$ may then be parameterised at lowest order in QED, as

$$\frac{d^2\sigma_{ep\to eX}}{dxdQ^2} = \frac{4\pi\alpha_{em}^2}{xQ^4} \left[xy^2 F_1(x, Q^2) + (1-y) F_2(x, Q^2) \right]. \tag{3.8}$$

F_1 describes the photo-absorption cross section for transversely polarised photons (σ_T), while F_2 is related to the sum of both the transverse and longitudinal photon cross sections ($\sigma_L + \sigma_T$). Specifically, the structure functions are related to the structure functions for transverse and longitudinal polarised photons, $F_T(x, Q^2)$ and $F_L(x, Q^2)$, by

$$F_T(x, Q^2) = 2xF_1(x, Q^2) \tag{3.9}$$

$$F_L(x, Q^2) = F_2(x, Q^2) - 2xF_1(x, Q^2). \tag{3.10}$$

Hence, the total cross section may be re-expressed as

$$\frac{d^2\sigma_{ep\to eX}}{dxdQ^2} = \frac{2\pi\alpha_{em}^2 Y_+}{xQ^4} \left[F_2(x, Q^2) - \frac{y^2}{Y_+} F_L(x, Q^2) \right] \tag{3.11}$$

[1] At high Q^2, where Z^0 exchange is significant, a third, parity-violating, structure function xF_3 is necessary to describe the full NC cross section.

[2] For a full derivation see, for instance, [41, 42].

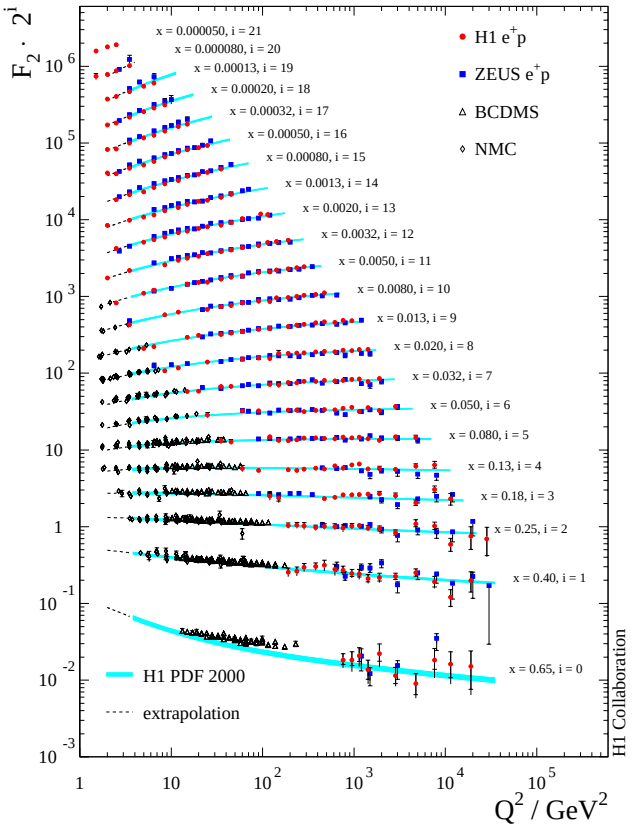

Figure 3.3: *Measurements of the structure function F_2, by H1 [43], ZEUS [44] and fixed target experiments [45, 46], as a function of Q^2 for a range of x values. The data are compared to the result of the H12002 PDF fit [43] (shaded band), which is extrapolated in the region below the starting scale of the fit (dashed line).*

where $Y_+ = 1 + (1 - y)^2$. Due to the spin-$\frac{1}{2}$ nature of the quarks, the F_L term is expected to be zero in the quark parton model (see section 3.2.1). Experimentally, the contribution due to F_L is small and can be neglected except at the highest y. This allows F_2 to be determined from the experimentally measured cross section by estimating the small contribution from F_L and Z_0 exchange and allowing for QED radiation corrections. The values obtained for F_2 by H1 [43] and ZEUS [44], along with fixed target results [45, 46], are presented in figure 3.3. Experimental observation of F_2 prior to HERA [47] showed little dependence on Q^2 over a wide

range of the $x - Q^2$ plane. This phenomenon is known as Bjorken scaling [48] and led to the formulation of the quark parton model (QPM).

3.2.1 Quark Parton Model

In the QPM [49] the proton is composed of non-interacting, point-like constituents, termed partons. The lack of length scale, due to the point-like nature of the partons, naturally explains the experimentally observed scale invariance. A particularly suitable frame in which to formulate the QPM is the infinite momentum frame of the proton. Here, the charge distribution within the proton is Lorentz contracted and the time scale for partons to interact with each other is time dilated, such that the partons are essentially frozen. Thus, on the scale of the partonic interactions, the photon-parton interaction is instantaneous and incoherent, meaning that the partons can be treated as free. This allows DIS to be considered as an incoherent elastic scattering of electrons off the individual charged partons, rather than the entire proton.

The DIS cross section may then be expressed as a sum over all active partons of the cross section for the elastic scattering of an electron off a parton of type i,

$$\frac{d^2\sigma_{ep\to eX}}{dxdQ^2} = \sum_i \int_0^1 dx f_i(x, Q^2) \frac{d^2\sigma_{eq_i\to eq_i}}{dxdQ^2}. \tag{3.12}$$

The parton density function (PDF), $f_i\,(x, Q^2)$, represents the probability of finding a parton q_i carrying a fraction x of the proton's momentum. The PDFs are independent of the hard scattering process, allowing them to be constrained through global fits to a variety of experimental results. The comparison of this result with equation 3.11 leads to the relations

$$F_2(x, Q^2) = x \sum_i e_i^2 f_i(x, Q^2) \tag{3.13}$$

and

$$F_2(x, Q^2) = 2xF_1(x, Q^2) \tag{3.14}$$

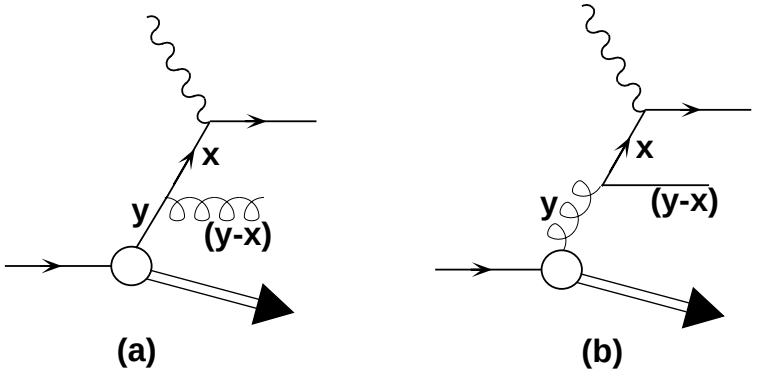

Figure 3.4: *A diagrammatic representation of the splitting functions (a) $P_{qq}(x/y)$, where the original quark radiates a gluon, and (b) $P_{qg}(x/y)$, where the original gluon splits into a quark-antiquark pair. In each case, the original parton carries a momentum fraction y, while the photon couples to a quark carrying momentum fraction x.*

where e_i is the electromagnetic charge of the parton q_i. The latter is known as the Callan-Gross relation [50] and is a consequence of the assumption that the partons carry spin-$\frac{1}{2}$ (which is equivalent to $F_L = 0$). The experimental verification of this relation provides direct evidence for the spin-$\frac{1}{2}$ nature of quarks (charged partons).

3.2.2 Scaling Violations

It can be seen from figure 3.3 that Bjorken scaling only holds exactly for $x \sim 0.1$. Away from this value, particularly at low x, the detailed measurements show a clear dependence on Q^2 and, hence, a violation of scaling. This is a consequence of the fact that, even at large Q^2, the strong coupling α_s is non-zero and, therefore, the partons must be regarded as weakly interacting.

Quantum Chromodynamics (QCD), the theory of the strong force, allows us to explain the deviations from the naïve QPM (which is zeroth order in QCD) by the addition of interacting gluons. Leading order QCD corrections are illustrated in

figure 3.4. Here, the struck quark may emit a gluon or the original gluon may split into a quark-antiquark pair, giving rise to a $q\bar{q}$ sea in addition to the three valence quarks. Further evidence for interacting gluons comes from the experimental observation that charged partons, which couple to the photon, only carry approximately half the momentum of the proton, requiring neutral partons to carry the remainder [42]. Higher order terms are included via a perturbative QCD (pQCD) expansion in orders of α_s and lead to logarithmic corrections to F_2 of the form $\alpha_s \ln Q^2$ and $\alpha_s \ln(1/x)$. Such an expansion converges only when there is a hard scale, such as a large Q^2, which gives rise to a small α_s. A small, but non-zero, F_L contribution is also predicted [51].

At a fixed order, n, in pQCD the full expansion of F_2 has terms of the form $\alpha_s^n \ln^m Q^2$ and $\alpha_s^n \ln^m(1/x)$ where $m \leq n$. A full QCD expansion is not tractable but analytical solutions exist in the form of evolution equations relating PDFs at one point in phase space to those at a starting point elsewhere. In different kinematic regions of the $x - Q^2$ plane, different terms dominate the expansion, giving rise to different evolution schemes.

3.3 Phenomenology in the Low x Regime

In the low x regime, F_2 shows a substantial rise with decreasing x, as shown in figure 3.5, which becomes more significant as Q^2 increases. This is a result of the increasing gluon density at low x and can be described by one of two pQCD evolution equations, DGLAP or BFKL, which are discussed in the following sections. The DGLAP equation describes the evolution of the PDFs in terms of Q^2, while the BFKL equation considers the PDF evolution with x. One of the physics aims at HERA is to search for unambiguous experimental evidence for BFKL evolution.

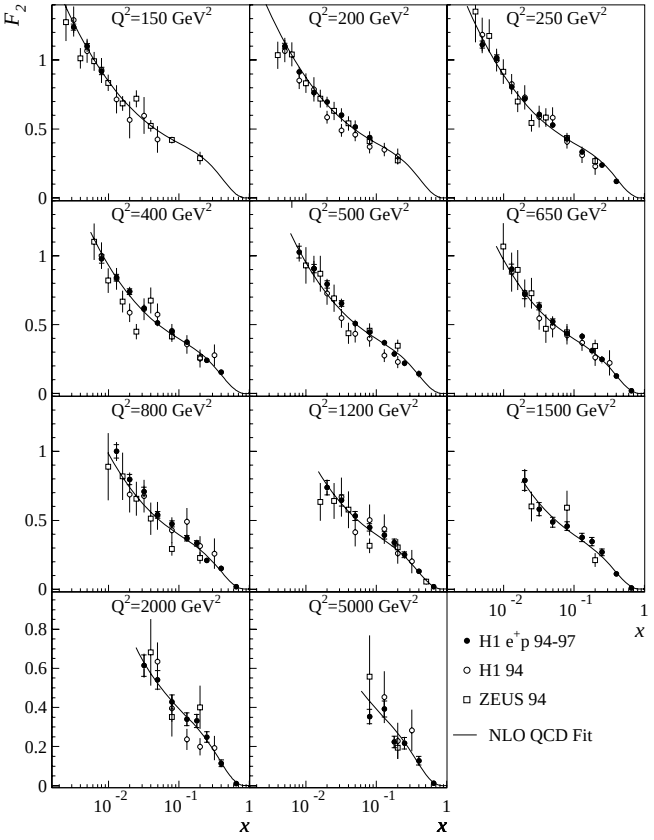

Figure 3.5: *Measurement of the structure function $F_2(x, Q^2)$ [52] at high Q^2 as a function of x along with the results of a NLO QCD fit. Also shown are the earlier H1 [53] and ZEUS [54] results.*

3.3.1 DGLAP Evolution Equation

The DGLAP [55] evolution equations of Dokshitzer, Gribov, Lipatov, Altarelli and Parisi express the Q^2 development of the PDFs at intermediate x. The equations are only calculable above a scale Q_0^2 (~ 1 GeV^2) where pQCD is applicable and hence require experimentally measured PDFs at this scale as an input. These PDFs are split into three types of density functions for the valence (flavour non-singlet) quarks, $q^{NS}(y, Q^2)$, the sea (flavour singlet) quarks, $q^S(y, Q^2)$, and the gluons, $g(y, Q^2)$. The PDFs are then evolved to higher Q^2 via partonic splitting, as illustrated in figure 3.4.

These splitting processes are expressed in terms of splitting functions $P_{ab}\left(\frac{x}{y}\right)$, depicting the probability that a struck parton a, carrying momentum fraction x, is emitted from another parton b, carrying momentum fraction y. The four different one-to-two splittings are described by four distinct Altarelli-Parisi splitting functions P_{qq}, P_{gq}, P_{qg} and P_{gg}. The splitting functions P_{qq} and P_{gq} represent the modification of the original valence quark distribution through gluon bremsstrahlung $q \rightarrow qg$. The sea quark distribution is adjusted by both pair production $g \rightarrow q\bar{q}$, which is represented by P_{qg}, and gluon bremsstrahlung. The gluon distribution is driven by gluon bremsstrahlung and subsequent gluon splitting $g \rightarrow gg$, described by P_{gg}. Calculations of the splitting functions up to next-to-next-to-leading order (NNLO) are currently available [56].

The resulting set of three coupled DGLAP evolution equations is

$$\frac{dq^{NS}\left(x,Q^2\right)}{d\ln Q^2} = \frac{\alpha_s\left(Q^2\right)}{2\pi}\int_x^1 \frac{dy}{y}\left[q^{NS}\left(y,Q^2\right)P_{qq}\left(\frac{x}{y}\right)\right] \tag{3.15}$$

$$\frac{dq^{S}\left(x,Q^2\right)}{d\ln Q^2} = \frac{\alpha_s\left(Q^2\right)}{2\pi}\int_x^1 \frac{dy}{y}\left[q^{S}\left(y,Q^2\right)P_{qq}\left(\frac{x}{y}\right) + g\left(y,Q^2\right)P_{qg}\left(\frac{x}{y}\right)\right] \tag{3.16}$$

$$\frac{dg\left(x,Q^2\right)}{d\ln Q^2} = \frac{\alpha_s\left(Q^2\right)}{2\pi}\int_x^1 \frac{dy}{y}\left[q^{S}\left(y,Q^2\right)P_{gq}\left(\frac{x}{y}\right) + g\left(y,Q^2\right)P_{gg}\left(\frac{x}{y}\right)\right]. \tag{3.17}$$

Solving these equations, along with equation 3.13, gives rise to a logarithmic dependence of F_2 on Q^2 that recreates the rise and fall of F_2 with Q^2 at low x and high x respectively. The Q^2 dependence results from the ability to probe an increasing proportion of the partonic structure as the resolving power of the virtual photon improves with Q^2. At high Q^2, the splitting processes produce a net increase in partons, which leads to an overall migration from high x to low x.

The complete DGLAP formalism iterates the leading order splitting process by summing terms containing the maximum power of $\ln Q^2$ to all orders in perturbation theory. This gives rise to a series of parton emissions, forming a ladder such as that illustrated in figure 3.6(a). The partons which make up the ladder have a strong

transverse momentum ordering

$$k^2_{Tn} \gg k^2_{Tn-1} \gg ... \gg k^2_{T1} \tag{3.18}$$

but weak longitudinal momentum ordering

$$x_n < x_{n-1} < ... < x_1. \tag{3.19}$$

In the leading logarithm approximation (LLA) only those terms in $\alpha_s^n \ln^n Q^2$ are considered in the sum. This is valid at large Q^2 and intermediate x, where the $\ln(1/x)$ terms can be neglected

$$\ln(1/x) \ll \ln(Q^2/Q_0^2), \tag{3.20}$$

provided perturbation theory is applicable ($\alpha_s \ll 1$). Parameterisations of F_2 based solely on DGLAP evolution are able to satisfactorily describe all current HERA data [43, 44].

3.3.2 BFKL Evolution Equation

At sufficiently low x, which may be approached in the HERA regime, the $\ln(1/x)$ terms neglected by the DGLAP evolution become important. An alternative evolution equation in terms of $\ln(1/x)$ at fixed Q^2 was developed by Balitsky, Fadin, Kuraev and Lipatov (BFKL) [57]. Due to the high partonic density, the low x regime is dominated by gluon splitting, leading to a gluon ladder such as that illustrated in figure 3.6(a). Unlike in the DGLAP case, the partons forming the ladder in the BFKL evolution have a strong longitudinal momentum ordering

$$x_n \ll x_{n-1} \ll ... \ll x_1 \tag{3.21}$$

but no transverse momentum ordering. In the LLA, terms containing the highest power of $\ln(1/x)$ are summed to all orders of perturbation theory. Hence, BFKL evolution is valid in the region of low x and moderate Q^2 where

$$\ln(1/x) \gg \ln(Q^2/Q_0^2) \tag{3.22}$$

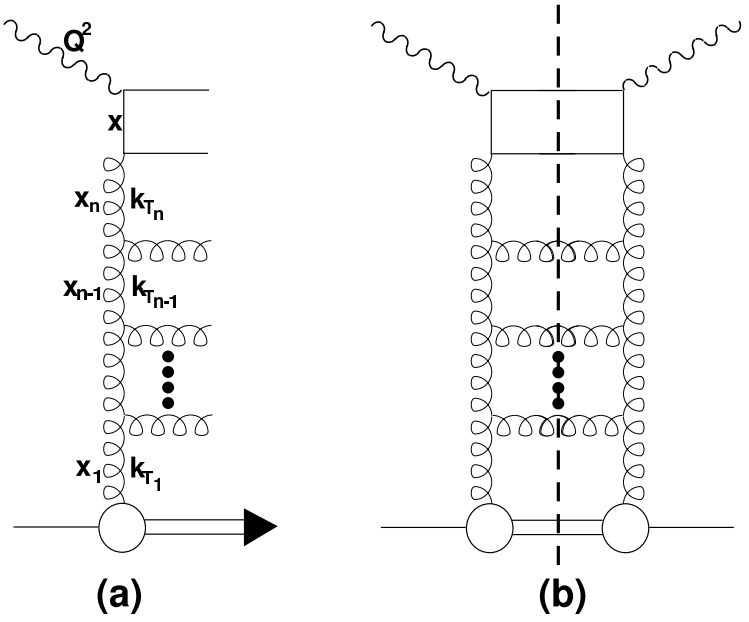

Figure 3.6: *(a) A ladder diagram which contributes to $F_2(x, Q^2)$ at low x. The ladder is composed of both quarks and gluons in the DGLAP equation, while only gluons contribute in the BFKL equation at leading order (LO). The evolution equations sum squared amplitudes such as that represented in (b) and cutting along the dotted line recovers the final states present in (a).*

is satisfied.

Summing squared amplitudes, such as that illustrated in figure 3.6(b), for the set of all possible gluon interactions leads to the BFKL equation

$$x\frac{df}{dx} \equiv K_L \otimes f\left(x, k_T^2\right) \tag{3.23}$$

where $\otimes$ represents the integration over k_T^2. K_L is the Lipatov kernel, which implements the sum over $\alpha_s^n \ln^n(1/x)$, and $f\left(x, k_T^2\right)$ is the unintegrated gluon density. Analytically solving the LLA BFKL equation at low x and fixed Q^2 gives the x dependence of F_2 as

$$F_2 \sim x^{-\lambda} \tag{3.24}$$

where

$$\lambda = \frac{12\alpha_s}{\pi} \ln 2, \tag{3.25}$$

which is around 0.5 for $\alpha_s \approx 0.25$ (corresponding to $Q^2 \approx 4$ GeV^2) . The BFKL equation then allows the structure function at low x to be predicted from the measured value at higher x but the same Q^2.

For $x < 0.01$, the measurements of F_2 may be parameterised as in equation 3.24 with the value of λ required to fit the data increasing from 0.2 to 0.4 over the Q^2 range 1.5 to 150 GeV^2 [58]. There is some evidence [59] that DGLAP fits to the structure functions, in particular F_L, may be improved by resumming the $\ln(1/x)$ terms in the splitting functions à la BFKL. Differentiation between the two different evolution equations may be provided by further measurements at HERA, such as production of forward jets [60] and pions [61] or vector meson production with large momentum transfer [62, 63].

3.4 Photoproduction and the Vector Dominance Model

The $1/Q^4$ term in the expression of the differential ep cross section (equation 3.8) means that interactions at HERA are dominated by the photoproduction regime, in which the electron acts as a source of almost real photons. In this case, HERA may be thought of as a γp collider and it is convenient to introduce a γp cross section, $\sigma_{\gamma p}$, defined by

$$\frac{d^2\sigma_{ep}}{dQ^2 dy} = \sigma_{\gamma p}(ys) F(y, Q^2) \tag{3.26}$$

where $F(y, Q^2)$ is the photon flux, which can be calculated via the Weizsäker-Williams approximation [64] in the case of quasi-real photons. In such events the γp centre of mass energy, W, which can be obtained from equations 3.6 and 3.7 after

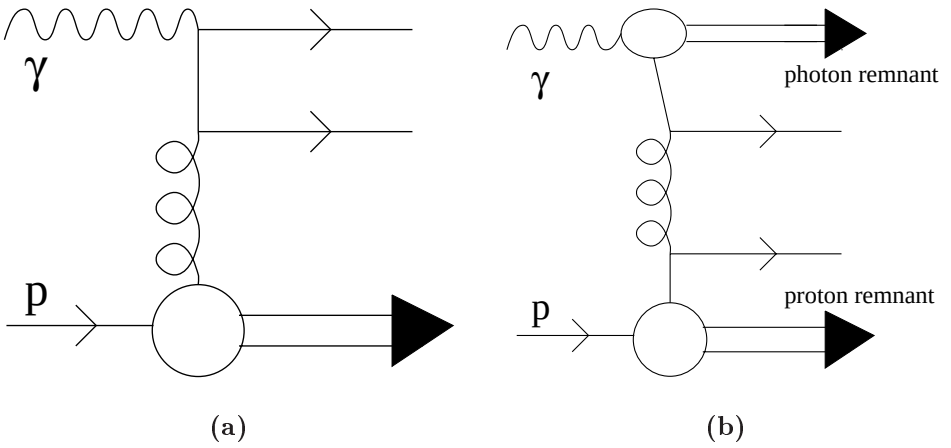

Figure 3.7: *Leading order (a) direct and (b) resolved photon–proton interactions.*

neglecting Q^2, is given by

$$W^2 = ys. \tag{3.27}$$

While DIS processes may be understood in terms of highly virtual photon probing the structure of the proton, photoproduction reactions are observed to resemble hadron-hadron collisions with a cross section reduced by α_{em}. At leading order, this may be understood in terms of two types of photon interaction: direct and resolved. In the direct process, the photon interacts as a point-like object, coupling directly to the hard subprocess via the boson-gluon fusion reaction shown in figure 3.7(a). In the resolved process the photon fluctuates into a $q\bar{q}$ pair long before the interaction with the proton, as shown in figure 3.7(b), giving rise to the hadronic behaviour. Subsequent QCD evolution gives rise to a photon consisting of quarks and gluons, which can be represented by a photon structure function F_2^γ in analogy to the proton.

The hadronic behaviour of photon-proton interactions led to the notion of the photon as a superposition of a purely electromagnetic bare component $|\gamma_B\rangle$ and a strongly interacting hadronic component $|h\rangle$,

$$|\gamma\rangle = \sqrt{Z_3}|\gamma_B\rangle + \sqrt{\alpha_{em}}|h\rangle, \tag{3.28}$$

where $1 - Z_3$ represents the probability of behaving hadronically. This is analogous

to the pair production of charged leptons, $l^{\pm}$, where the photon fluctuates into the state $|l^+l^-\rangle$.

The hadronic component of the photon must retain the quantum numbers of the bare state, $J^{PC} = 1^{--}$ with no charge and zero baryon number and strangeness, which has been experimentally confirmed in quasi-elastic photon interactions [65]. This gave rise to the vector meson dominance model (VDM) [66–68], in which the hadronic component is represented by a linear superposition of vector mesons

$$\sqrt{\alpha_{em}}|h\rangle = \sum_V \frac{e}{f_V}\frac{m_V^2}{Q^2+m_V^2}|V\rangle \tag{3.29}$$

where m_V is the mass of vector meson V and f_V is its coupling to the photon. Hence, at high energy, the amplitude for a photon-proton interaction $\gamma p \to X$ is equivalent to the sum of the amplitudes for the corresponding reactions involving vector mesons, $Vp \to X$:

$$A_{\gamma p\to X}(Q^2, W^2, t) = \sum_V \frac{e}{f_V}\frac{m_V^2}{Q^2+m_V^2}A_{Vp\to X}(W^2, t), \tag{3.30}$$

where each component is multiplied by the appropriate propagator factor.

The initial formulation of the VDM by Sakurai [66] contained only the three vector mesons $\rho(770)$, $\omega(783)$ and $\phi(1020)$ in the approximate ratio

$$\rho : \omega : \phi = 1 : 1/9 : 2/9 \tag{3.31}$$

given by SU(4), which ignores the differences between the vector meson masses and wavefunctions. This was later generalised to include other vector mesons [67], such as the $\rho'(1450)$, $J/\psi(3097)$ and $\Upsilon(9460)$, and then extended to include a continuum of unbound states having the appropriate quantum numbers [68], such as $\pi^+\pi^-$, $\pi^+\pi^-\pi^0$ and $K\bar{K}$. The model was able to provide a successful phenomenological description of photon interactions at high energy.

This formalism applies to transversely polarised photons, as is always the case if the photons are real. For electroproduction ($Q^2 > 0$), however, a significant

longitudinal photon component is observed and, in this regime, the ratio of the longitudinal to transverse cross sections can be parameterised as

$$R = \frac{\sigma_L}{\sigma_T} = \frac{\xi Q^2}{m_V^2} \tag{3.32}$$

where the value of ξ is determined experimentally. In photoproduction, where the photons are almost purely transversely polarised and the longitudinal component may be neglected, R tends to zero.

Chapter 4

Diffraction

Diffractive scattering was first observed around 40 years ago in hadron-hadron collisions. It was so called due to the similarity between the angular distribution of the scattered hadrons and the well known optical diffraction pattern. Renewed interest in diffraction came about following the observation at HERA of a class of DIS events containing a large rapidity gap [4].

Hadron-hadron cross sections at high energy are dominated by peripheral soft interactions. The resulting absence of a hard scale prevents the application of perturbative QCD and necessitates the use of phenomenological models such as Regge theory (see section 4.1). In this framework, the observed rise in the total cross section at high energies is described in terms of a diffractive exchange known as the pomeron, which carries the quantum numbers of the vacuum. The nature of the exchanged object has, however, proved elusive.

HERA offers the possibility to study diffractive processes in the presence of a hard scale, where calculations based on perturbative QCD are valid. In this language, diffraction is viewed as the exchange of a collection of two, or more, gluons which form a colour singlet state. In diffractive DIS [69], Q^2 provides the hard scale and permits the photon to probe the structure of the pomeron (see figure 3.6). Evidence

for a hard scale is also observed in diffractive photoproduction, although it can no longer be provided by Q^2. Possible alternatives for providing the hard scale are the mass of the quarks involved in the interaction, such as in the case of a J/ψ meson, or the momentum transfer squared at the proton vertex, $|t|$.

The subject of this thesis is the diffractive production of vector mesons with a large momentum transfer at the proton vertex. This process provides a powerful tool to study the structure of the diffractive exchange and its description in terms of pQCD (see section 4.3.3). It is discussed in detail in section 4.3.

4.1 Regge Theory

Before the advent of QCD, the scattering of strongly interacting particles could be described in terms of Regge theory. The theory is based on general assumptions about the scattering process and aims to provide a description of the scattering amplitude in the limit that the centre of mass energy is much larger than all other scales involved in the process. Its predictions must therefore act as a constraint on the properties of QCD in the high energy limit [70]. A brief overview of Regge theory is given in the following section with the aim of introducing the notion of a diffractive exchange and its description in terms of the pomeron. A more detailed explanation can be found in [3].

4.1.1 s and t Channel Processes

A general two body scattering process $ab \to cd$ may be described in terms of a set of Lorentz invariant quantities. A convenient set of such invariants are the Mandelstam

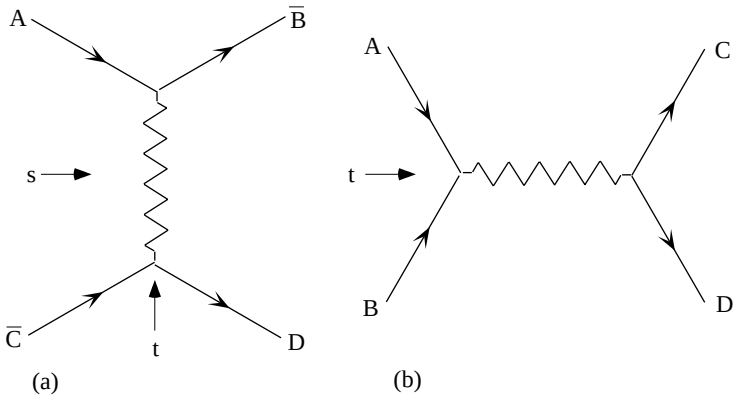

Figure 4.1: *Schematic illustrations of (a) the t-channel process* $a\bar{c} \to \bar{b}d$ *and (b) the related s-channel process* $ab \to cd$.

variables s, t and u defined by

$$s = (p_a + p_b)^2 = (p_c + p_d)^2 \tag{4.1}$$

$$t = (p_a - p_c)^2 = (p_b - p_d)^2 \tag{4.2}$$

$$u = (p_a - p_d)^2 = (p_b - p_c)^2, \tag{4.3}$$

where p_i denotes the four momentum of particle i. Using conservation of momentum, it can be shown that u is not an independent variable and hence, the scattering amplitude A can be written as a function of s and t only, $A = A(s,t)$. Here, s denotes the square of the centre of mass energy and the modulus of t, which itself is negative, denotes the square of the momentum transferred between the interacting particles. Regge theory is applicable in the Regge limit where $s \to \infty$ and $s \gg |t|$.

Scattering processes are interpreted in terms of intermediate propagators which can be exchanges, such as the t-channel process shown in figure 4.1(a), or resonances, such as the s-channel process shown in figure 4.1(b). Assuming the scattering amplitude is an analytic function of the invariants, which are taken as complex variables, leads to an important relation between these two processes, known as crossing symmetry. Consider the s-channel reaction $ab \to cd$, which is physical in the range $s > 0$ and $t < 0$. If this is then extended into the unphysical range $s < 0$ and $t > 0$, one obtains the t-channel reaction $a\bar{c} \to \bar{b}d$. Crossing symmetry states that these two

processes, although taking place in physically disconnected regions of s and t space, have identical amplitudes

$$A_{ab\to cd}(s,t) = A_{a\bar{c}\to\bar{b}d}(t,s) \tag{4.4}$$

provided s and t are interchanged.

4.1.2 Regge Trajectories

The scattering amplitude for the t-channel process $a\bar{c} \to \bar{b}d$ may be decomposed into a series of partial waves of varying angular momentum l,

$$A_{a\bar{c}\to\bar{b}d} = \sum_{l=0}^{\infty}(2l+1)\alpha_l(s)P_l(\cos\theta), \tag{4.5}$$

where $P_l(\cos\theta)$ are the Legendre polynomials and $\alpha_l(s)$ are the partial wave amplitudes. The scattering angle θ between a and $\bar{c}$ in the centre of mass frame is defined by $\cos\theta = 1 + \frac{2t}{s}$. Using crossing symmetry, this amplitude may be continued into the s-channel region to give the amplitude for the process $ab \to cd$. The full set of partial waves can be summed using a method suggested by Sommerfeld [71], whereby the discrete sum is replaced by a contour integral in the complex angular momentum plane (the functions α_l and P_l having been analytically continued). Deforming the contour, one picks up contributions due to any poles which exist in the complex angular momentum plane. The pole in the l^{th} partial wave has the form

$$\alpha_l(t) \simeq \frac{\beta(t)}{l - \alpha(t)}, \tag{4.6}$$

giving rise to a Regge pole at $\alpha(t) = l$ with a residue function $\beta(t)$ which represents the coupling of the pole to the external particles. In the Regge limit, the scattering amplitude is dominated by the pole having the largest real angular momentum component, i.e. the pole situated furthest to the right in the complex angular momentum plane. This allows the leading dependency of the scattering amplitude on

s, which describes the high energy behaviour, to be written as

$$A(s,t) \to \beta(t) \left(\frac{s}{s_0}\right)^{\alpha(t)}, \tag{4.7}$$

where s_0 defines the relevant energy scale. This may be viewed as the exchange of an object with angular momentum $\alpha(t)$, known as a reggeon. This is not a true particle since the angular momentum is a continuous complex variable (the complex part represents the decay width of unstable hadrons). Rather, it is a sum over all possible exchanged particles having the appropriate quantum numbers. In the t-channel, at positive t, the amplitude consists of a series of poles corresponding to physical particles of mass m_i having spin J_i, such that $\alpha(m_i^2) = J_i$. These particles may be thought of as angular momentum excitations of the lowest lying state, such that the relationship between their angular momentum and mass squared is known as a Regge trajectory. In general, such a trajectory is observed experimentally to follow a straight line of the form

$$\alpha(t) = \alpha(0) + \alpha' t. \tag{4.8}$$

The resulting differential cross section is given by

$$\frac{d\sigma}{dt} \sim \frac{1}{s^2}|A(s,t)|^2 \tag{4.9}$$

which, for a process dominated by the exchange of a single trajectory, may be written, using equation 4.7, as

$$\frac{d\sigma}{dt} \sim f(t) \left(\frac{s}{s_0}\right)^{2\alpha(t)-2} \tag{4.10}$$

where $f(t)$ represents the remaining t dependence, not contained in $\alpha(t)$.

Regge theory is able to accurately predict the s and t dependencies for many low momentum transfer hadronic interactions over a wide range in centre of mass energy [72]. As an example, consider the s-channel reaction $\pi^- p \to \pi^0 n$ and its related t-channel process $\pi^-\pi^0 \to \bar{p}n$. The t-channel amplitude has a series of poles corresponding to the production of physical particles having the quantum numbers

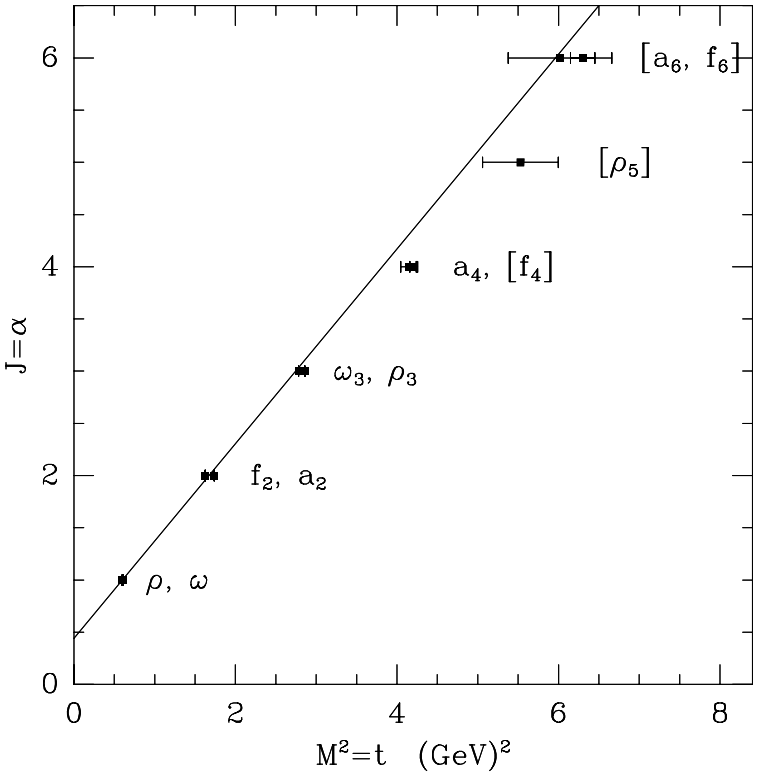

Figure 4.2: *The Chew-Frautschi plot showing the rho trajectory, which consists of the ρ, ω, f and a mesons [73].*

of the ρ meson. Chew and Frautschi [73] showed these particles are well described by a straight line trajectory of the form given in equation 4.8 with $\alpha(0) = 0.55$ and $\alpha' = 0.86$ GeV^{-2}, as shown in figure 4.2. The continuation of this trajectory to negative t, shown in figure 4.3, provides a good description of the data measured directly in the s-channel reaction [74]. The $\pi^- p \to \pi^0 n$ cross section is well described by equation 4.10.

The Dependence on t and Shrinkage

Using the Regge trajectory from equation 4.8, the differential cross section given in equation 4.10 may be written as

$$\frac{d\sigma}{dt} \sim f(t) \left(\frac{s}{s_0}\right)^{2\alpha(0)-2} \left(\frac{s}{s_0}\right)^{2\alpha' t} . \tag{4.11}$$

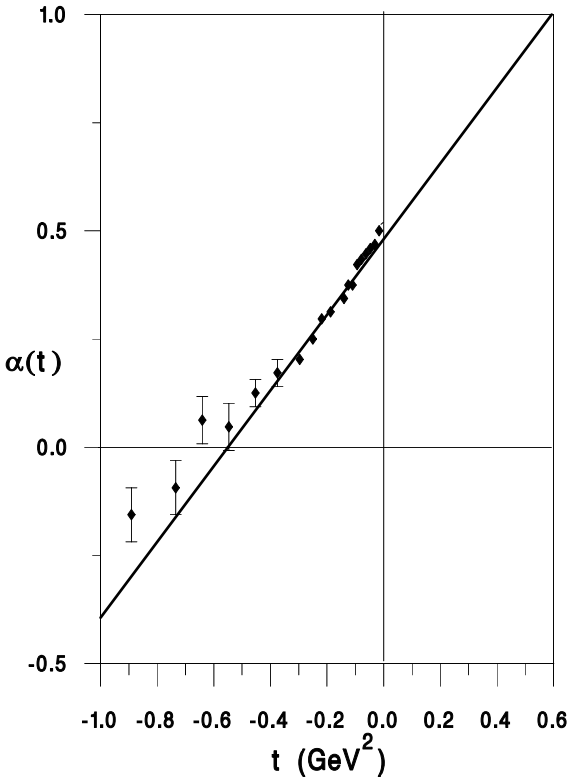

Figure 4.3: *The values of $\alpha(t)$ obtained from $\pi^- p \to \pi^0 n$ scattering data (points) compared to an extrapolation of the trajectory shown in figure 4.2 to $t < 0$ [3].*

It is observed experimentally that the t dependence of the cross section at low $|t|$ follows an exponential form. Hence, writing $f(t) = e^{b_0 t}$, equation 4.11 may be re-expressed as

$$\frac{d\sigma}{dt} \sim f(t) \left(\frac{s}{s_0}\right)^{2\alpha(0)-2} e^{2\alpha' \ln\left(\frac{s}{s_0}\right) t} \tag{4.12}$$

$$\sim \left.\frac{d\sigma}{dt}\right|_{t=0} e^{bt}, \tag{4.13}$$

where b is the slope parameter, given by

$$b = b_0 + 2\alpha' \ln\left(\frac{s}{s_0}\right). \tag{4.14}$$

Since α' is positive, b grows with s and, as t is negative, leads to a logarithmic increase in the t slope with the centre of mass energy. This increase in the sharpness of the forward ($t = 0$) peak is known as shrinkage.

4.1.3 Total Cross Sections and The Pomeron Trajectory

The Optical Theorem, which is a consequence of the unitarity of the scattering matrix arising from probability conservation, relates the imaginary part of the forward elastic amplitude, A_{el}, to the total scattering cross section via

$$\sigma_{tot} = \frac{1}{s}\Im m A_{el}(s,0). \tag{4.15}$$

Since, in the Regge limit, the elastic amplitude is almost purely imaginary, it follows, from equations 4.7 and 4.8, that

$$\sigma_{tot} \sim s^{\alpha(0)-1} \tag{4.16}$$

where $\alpha(0)$ is the intercept of the appropriate trajectory.

The total cross section for hadron-hadron collisions is experimentally observed to rise slowly with s [75], clearly requiring an intercept $\alpha(0) \geq 1$. However, all meson trajectories, such as the ρ trajectory already seen, are observed to have $\alpha(0) \lesssim 0.5$ and hence an exchange involving such quantum numbers leads to a cross section that falls with s. In fact, Pomeranchuk and Okun [76] proved that any cross section whereby charge is exchanged gives rise to a cross section that vanishes as $s \to \infty$. This is known as the Pomeranchuk theorem. However, Foldy and Peierls [77] reversed this statement to argue that any cross section which does not fall as $s \to \infty$ must be dominated by the exchange of vacuum quantum numbers (i.e. isospin zero and even under charge conjugation). Hence, the total hadron-hadron cross section requires a trajectory with $\alpha(0) \geq 1$ and vacuum quantum numbers. Such a trajectory is known as the pomeron ($\mathbb{P}$) and interactions described by its exchange are called diffractive. No physical particles lying on this trajectory have ever been conclusively observed, although bound states of gluons, known as glueballs, do exist in QCD.

The total pp and $p\bar{p}$ cross section is shown in figure 4.4, along with fits by Donnachie and Landshoff [78] of the form

$$\sigma_{tot}(s) = X s^{\alpha_{\mathbb{P}}(0)-1} + Y s^{\alpha_{\mathbb{R}}(0)-1} \tag{4.17}$$

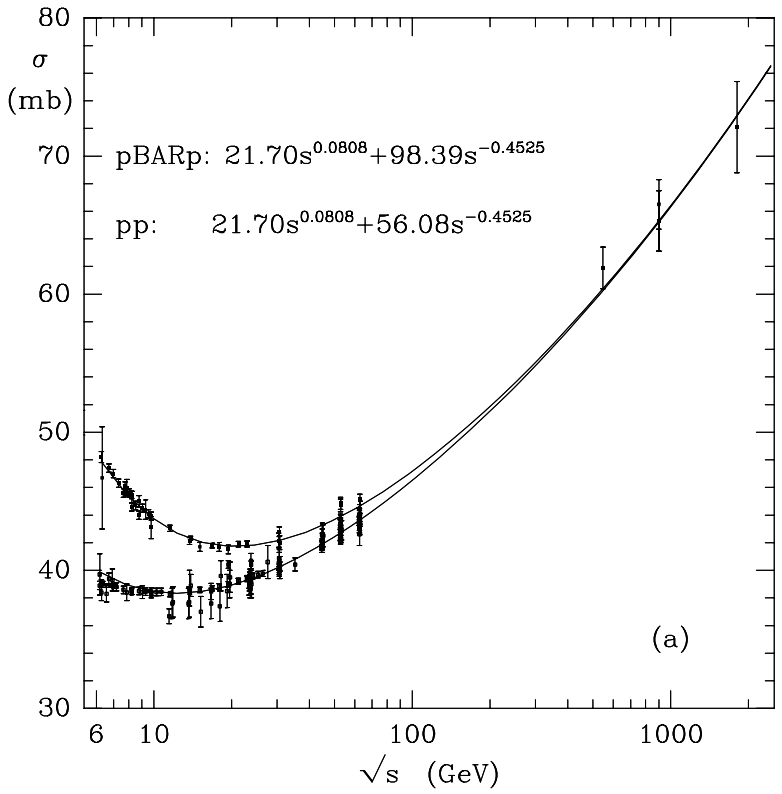

Figure 4.4: *The dependence of the total proton-proton and proton-antiproton cross sections on centre of mass energy compared to fits by Donnachie and Landshoff [78].*

where the separate terms represent the contribution due to the pomeron, $\alpha_{I\!P}$, and reggeon, $\alpha_{I\!R}$, trajectories and X and Y are the normalisation of the two components. The obtained pomeron intercept is $\alpha_{I\!P} = 1.08$ with the same strength for both interactions, since a vacuum exchange is unable to distinguish between particles and antiparticles. The reggeon term has an intercept $\alpha_{I\!R} = 0.55$ and is able to distinguish between the two processes. Hence, from equation 4.16, the pomeron contribution must dominate over the reggeon contribution at high energies. The fits are also able to describe the $\pi^- p$, $\pi^+ p$ and γp [79] total cross sections with the same intercepts, indicating that the pomeron may be considered as a universal object. Information on the slope of the pomeron trajectory, $\alpha'_{I\!P}$, can be obtained by analysing the elastic pp and $p\bar{p}$ cross sections differentially in t (see equation 4.12).

The value obtained by Donnachie and Landshoff is $\alpha'_{I\!P} = 0.25$ GeV^{-2} [78]. Hence, following equation 4.8, the pomeron trajectory can be parameterised as

$$\alpha_{I\!P}(t) = 1.08 - 0.25|t|. \tag{4.18}$$

HERA offers the possibility to study diffractive processes in the presence of a hard scale. Such a hard scale allows pQCD calculations to be performed and, hence, the interpretation of diffraction is no longer purely a matter for Regge phenomenology. Consequently, HERA offers a unique opportunity to probe the boundary between Regge theory and QCD.

4.2 Diffraction at HERA

The start of HERA operation saw the observation of a class of DIS events containing a large rapidity gap between the outgoing proton direction and the remainder of the hadronic final state [4]. Within Regge theory and QCD, such events can be interpreted as a highly virtual photon, γ^*, probing the structure of a colour singlet object, termed the pomeron, arising from the proton. This observation revitalised experimental and theoretical interest in the field of diffraction. This section outlines the principal characteristics of diffractive events in ep interactions and the following section concentrates specifically on diffractive vector meson production, which is the subject of this thesis.

Figure 4.5 illustrates a generic inclusive diffractive interaction in ep scattering, $ep \to eXY$. The hadronic final state is divided into two systems X and Y, having masses M_X and M_Y respectively, separated by a large rapidity gap, $\Delta\eta$. The Y system may either be the intact proton, whereby the event is termed (proton) elastic, or a low mass hadronic system arising from the break up of the proton, whereby the event is termed (proton) dissociative. The negative four momentum transferred

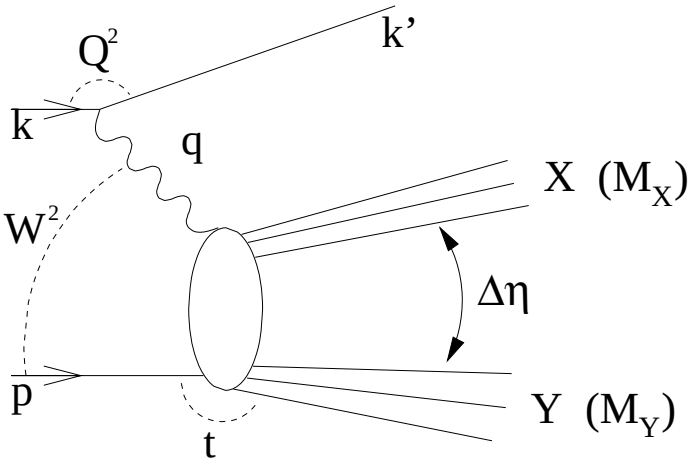

Figure 4.5: *A schematic representation of inclusive diffraction, $ep \to eXY$.*

squared at the proton vertex, t, is defined by

$$t = (p - Y)^2 \;=\; (q - X)^2 \tag{4.19}$$

where the appropriate four vectors are defined in figure 4.5. In the case that both Q^2 and $|t|$ are small, the size of the rapidity gap is given by

$$\Delta\eta \simeq \ln\left(\frac{W^2}{M_X M_Y}\right). \tag{4.20}$$

In the Regge limit, both M_X and M_Y are small, $M_X, M_Y \ll W$, leading to the large rapidity gap observed.

In the photoproduction regime, diffractive processes make up about 40% of the total photoproduction cross section for HERA energies [79]. In order for a photon to interact with a proton via pomeron exchange it must first fluctuate into a $q\bar{q}$ pair. The truly elastic process $\gamma p \to \gamma p$ then has a very low cross section since it is of order α_{em}^2. However, the quasi-elastic reaction $\gamma p \to Vp$, shown in figure 4.6(a), is only of order α_{em} and makes up around 10% of the total γp cross section [79]. Diffraction also exists as an inelastic process, where one or both of the incoming hadrons undergo dissociation as a result of non-zero momentum transfer at the corresponding vertex, as shown in figures 4.6(b)–(d). Since no colour is exchanged

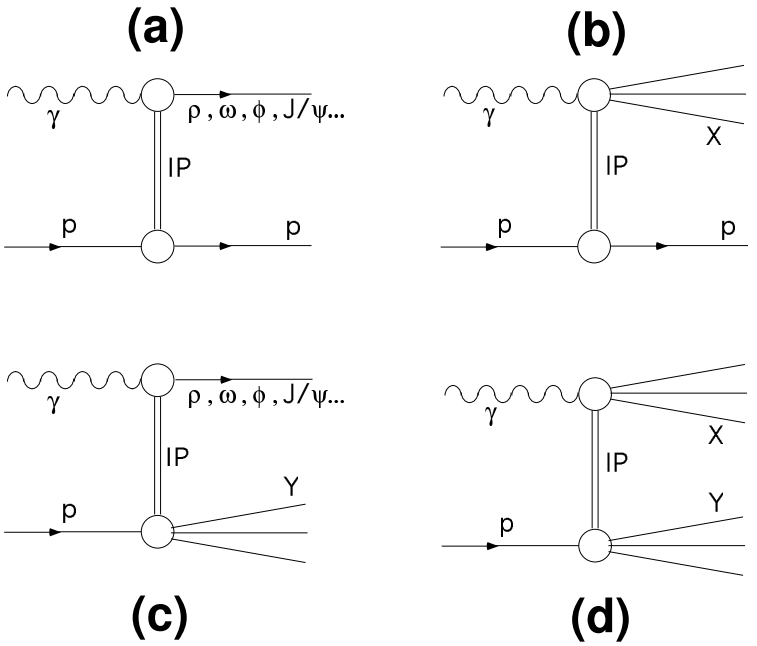

Figure 4.6: *Diffractive γp interactions: (a) quasi-elastic vector meson production $\gamma p \to Vp$, (b) single photon dissociation $\gamma p \to Xp$, (c) single proton dissociative vector meson production $\gamma p \to VY$ and (d) double dissociation $\gamma p \to XY$.*

the dissociated state must once again retain the quantum numbers of the incoming particle.

4.3 Diffractive Vector Meson Production

Diffractive vector meson production corresponds to the system X consisting of a single vector meson, V:

$$ep \to eVY \tag{4.21}$$

and is illustrated in figure 4.7 for both the elastic and dissociative channels. This process provides a clean experimental signature in which the kinematics can be precisely determined through an accurate measurement of the vector meson four momentum. Consequently, it forms a powerful tool by which to study the structure

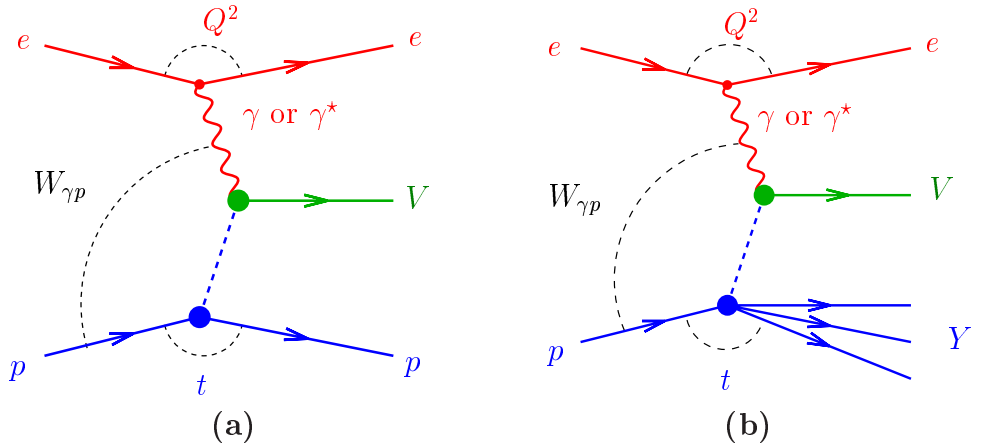

Figure 4.7: *Feynman diagrams illustrating diffractive vector meson production in (a) the proton elastic and (b) proton dissociative case.*

of the diffractive exchange.

This section begins with the definition of the angular distributions which are used to study the polarisation of the produced vector meson. A brief overview of selected results on diffractive vector meson production at HERA is then given, focusing mainly on the region of large momentum transfer relevant to this analysis. Finally, the description of diffractive vector meson production at large momentum transfer within the framework of pQCD is outlined.

4.3.1 Helicity Structure

The helicity of the produced vector meson is sensitive to both the photon polarisation and the meson wavefunction. The polarisation states of the vector meson and the exchanged photon are related to the production and decay angular distributions of the vector meson and, in the case of unpolarised beams, are completely described by 15 spin density matrix elements (SDMEs) [80].

For a vector meson undergoing a two body decay, the angular distributions are characterised by three angles as shown in figure 4.8. Φ is the angle between the vector

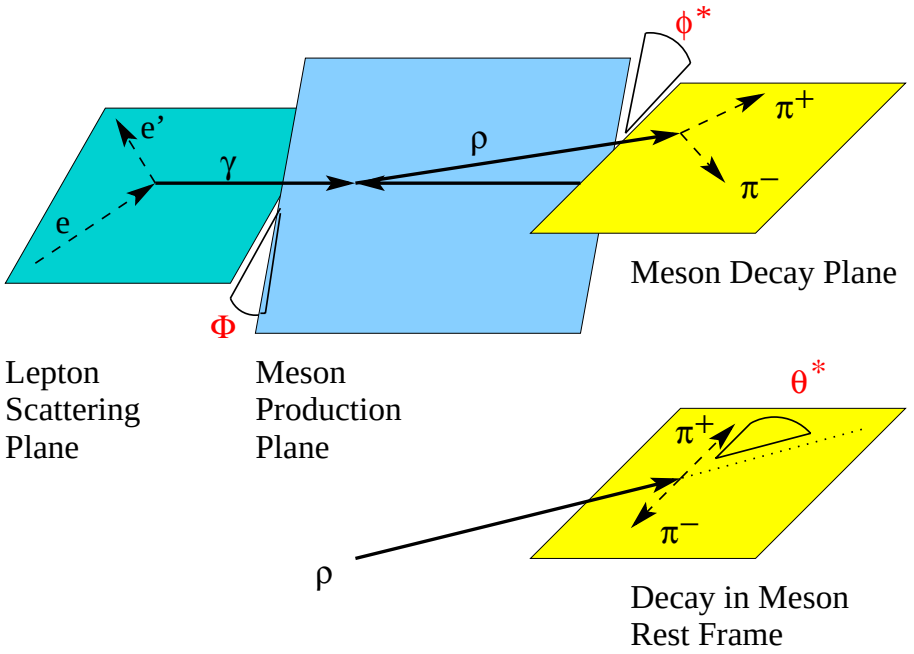

Figure 4.8: *An illustration of the production and decay angles used to analyse the polarisation of the ρ meson.*

meson production plane (defined as the plane containing the momentum vectors of the virtual photon and the vector meson) and the electron scattering plane in the γp centre of mass system. θ^* and ϕ^* represent, respectively, the polar and azimuthal angles of the positively charged decay particle in the vector meson helicity frame. This is the centre of mass frame of the vector meson with the vector meson direction in the γp centre of mass frame defining the quantisation axis. The azimuthal angle, ϕ^*, is defined as the angle between the vector meson production and decay planes in the γp centre of mass system. The polar angle, θ^*, is the angle of the positive decay particle with respect to the quantisation axis in the vector meson centre of mass system. In the case of photoproduction, the angle Φ is not measured since the direction of the scattered electron is not explicitly determined. Averaging over this angle reduces the necessary spin density matrix elements to three.

For a ρ meson decaying into two spin-0 pions, the normalised two-dimensional

angular distribution, averaged over Φ, can be written in terms of the SDMEs r^{04}_{ij} as

$$\begin{aligned}\frac{1}{\sigma}\frac{d^2\sigma}{d\cos\theta^* d\phi^*} &= \frac{3}{4\pi}\left[\frac{1}{2}(1-r^{04}_{00}) + \frac{1}{2}(3r^{04}_{00}-1)\cos^2\theta^*\right. \\ &\left. -\sqrt{2}\mathrm{Re}\left[r^{04}_{10}\right]\sin 2\theta^*\cos\phi^* - r^{04}_{1-1}\sin^2\theta^*\cos 2\phi^*\right]. \quad (4.22)\end{aligned}$$

Integrating over θ^*or ϕ^*, respectively, further reduces this to the one dimensional distributions

$$\frac{d\sigma}{d\cos\theta^*} \propto 1 - r^{04}_{00} + (3r^{04}_{00}-1)\cos^2\theta^* \quad (4.23)$$

and

$$\frac{d\sigma}{d\phi^*} \propto 1 - 2r^{04}_{1-1}\cos 2\phi^*. \quad (4.24)$$

The SDMEs are defined as bilinear combinations of the helicity amplitudes $M_{\lambda_\gamma\lambda_V}$, where $\lambda_\gamma, \lambda_V = -, 0, +$ are the respective helicities of the photon and the vector meson. Each helicity amplitude represents a possible transition between the photon and the vector meson. For photoproduction, where the photon is quasi-real, the longitudinal photon polarisation is negligible and only the transverse polarisation states remain. Thus, the allowable photon-meson transitions can be described in terms of three independent helicity amplitudes M_{++}, M_{+0}, M_{+-}[1], which represent no change in helicity (no-flip), a single change in helicity (single-flip) or a double change in helicity (double-flip) respectively. In this case, the matrix elements are related to the helicity amplitudes by

$$r^{04}_{00} = \frac{|M_{+0}|^2}{|M_{++}|^2 + |M_{+0}|^2 + |M_{+-}|^2} \sim |M_{+0}|^2 \quad (4.25)$$

$$r^{04}_{10} = \frac{1}{2}\frac{M_{++}M^*_{+0} - M_{+-}M^*_{+0}}{|M_{++}|^2 + |M_{+0}|^2 + |M_{+-}|^2} \sim \mathrm{Re}[M^*_{+0}(M_{++} - M_{+-})] \quad (4.26)$$

$$r^{04}_{1-1} = \frac{1}{2}\frac{M_{++}M^*_{+-} + M_{+-}M^*_{++}}{|M_{++}|^2 + |M_{+0}|^2 + |M_{+-}|^2} \sim \mathrm{Re}[M_{++}M^*_{+-}]. \quad (4.27)$$

Under the assumption of s-channel helicity conservation (SCHC), where the vector meson retains the helicity of the photon, only the amplitude M_{++} is non-zero and consequently it is predicted that r^{04}_{00}, r^{04}_{10} and r^{04}_{1-1} are all zero.

[1]The three corresponding amplitudes M_{--}, M_{-0} and M_{-+} also exist but are not independent since they satisfy $M_{++} = M_{--}$, $M_{+-} = M_{-+}$ and $M_{+0} = -M_{-0}$.

Vector Meson	Quark Content	Mass (MeV)	Width (MeV)
ρ	$\frac{1}{\sqrt{2}}(u\bar{u} - d\bar{d})$	775.8 ± 0.5	150.3 ± 1.6
ω	$\sim \frac{1}{\sqrt{2}}(u\bar{u} + d\bar{d})$	782.59 ± 0.11	8.49 ± 0.08
ϕ	$\sim s\bar{s}$	1019.456 ± 0.020	4.26 ± 0.05
J/ψ	$c\bar{c}$	3096.916 ± 0.011	0.091 ± 0.0032
$\psi(2s)$	$c\bar{c}$	3686.093 ± 0.034	0.281 ± 0.017
$\Upsilon(1s)$	$b\bar{b}$	9460.30 ± 0.26	0.053 ± 0.0015

Table 4.1: *An overview of the properties of the vector mesons studied at HERA [106]. The ρ' is omitted since its properties are not well known.*

4.3.2 Previous Measurements

The diffractive production of the mesons ρ, ω, ϕ, J/ψ, Υ and the excited states $\psi(2s)$ and ρ' have been studied at HERA in both the photoproduction ($Q^2 \approx 0$) and electroproduction ($Q^2 > 0$) regimes by H1 [63, 81–93] and ZEUS [62, 94–105]. The properties of these vector mesons are summarised in table 4.1. This section presents selected experimental results, concentrating primarily on the region of large momentum transfer relevant to this thesis.

Elastic vector meson production is predicted by Regge theory to have the same dependence on centre of mass energy as the total γp cross section. Hence, it follows from equation 4.11 (using $W^2 = ys$) that the W dependence of the cross section for elastic vector meson production can be parameterised as

$$\sigma_{\gamma p \to Vp} \sim W^{\delta} \tag{4.28}$$

where $\delta = 4(\langle \alpha_{I\!P}(t) \rangle - 1)$. For the parameterisation of the pomeron trajectory given in equation 4.18 and $1/\langle t \rangle = b \approx 10$ GeV^{-2} for the photoproduction of ρ meson [81, 98], one obtains a value $\delta \approx 0.22$. The measured energy dependence of the elastic vector meson production cross section in photoproduction is shown in figure 4.9. The ρ and ω cross sections are indeed similar to the total γp cross section

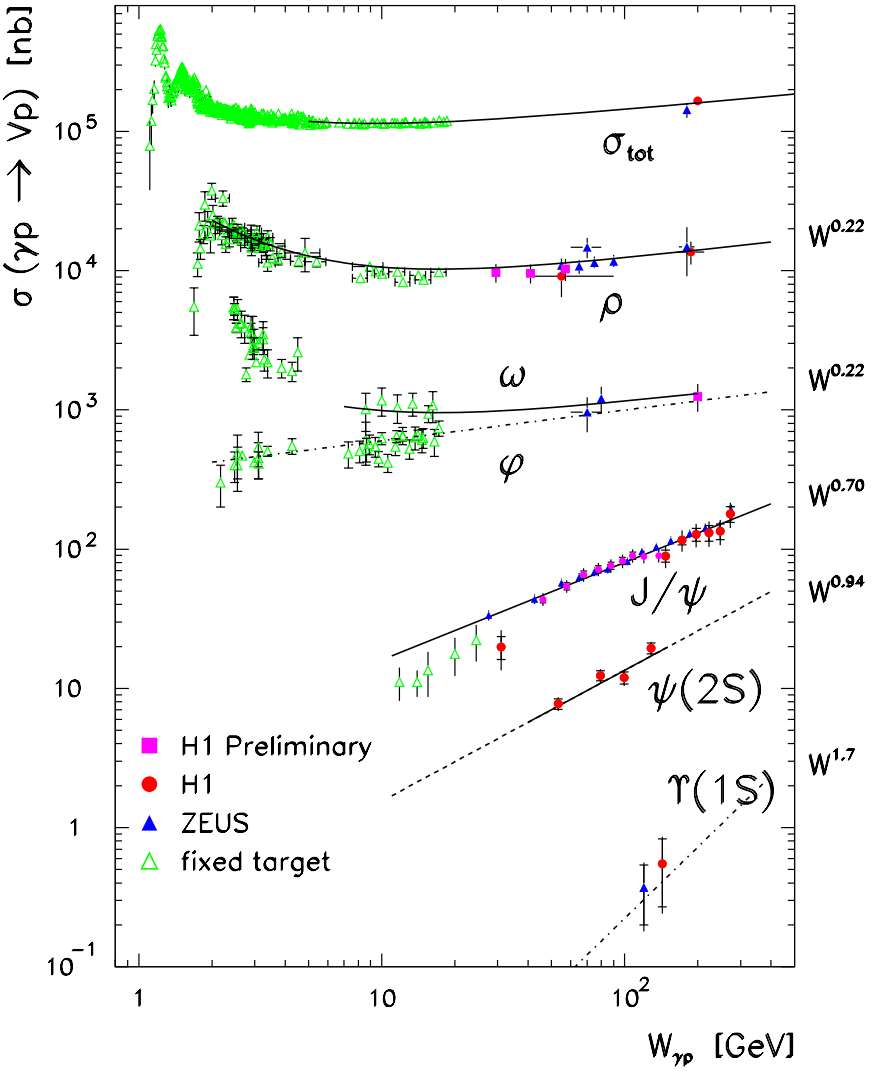

Figure 4.9: *The dependence of the total photon-proton cross section and the elastic vector meson photoproduction cross section on the centre of mass energy as measured at HERA and fixed target experiments [107]. The curves represent the prediction of Regge theory for a pomeron with* $\alpha_{I\!P}(0) = 1.08$ *and* $\alpha'_{I\!P} = 0.25$ GeV^{-2} *in the case of the light vector mesons (*ρ*,* ω *and* ϕ*) and a fit of the form* W^{δ} *for the heavier mesons.*

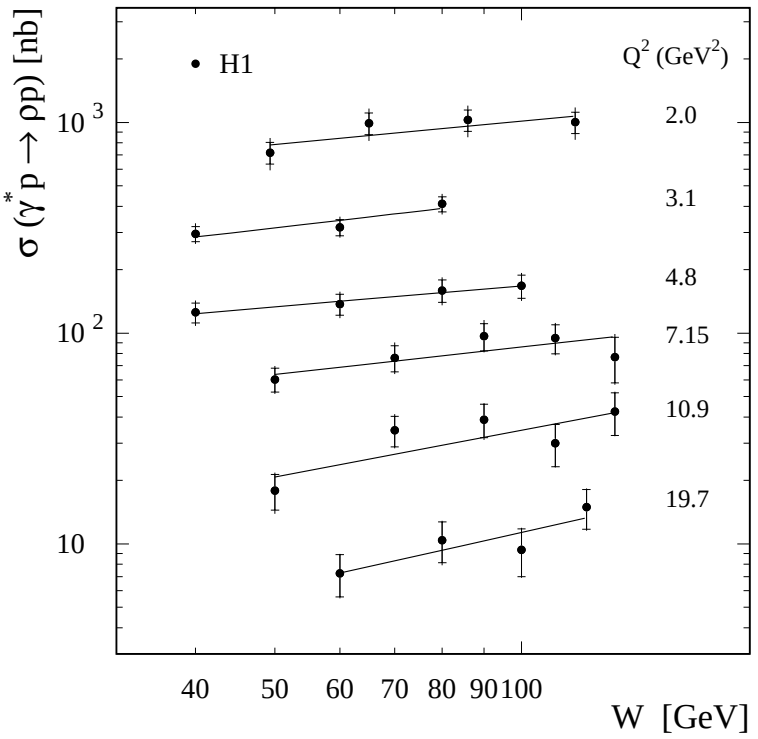

Figure 4.10: *The dependence of the ρ meson cross section in electroproduction on W for various Q^2 values as measured by the H1 Collaboration [81]. The curves represent the result of a fit of the form W^{δ}.*

and show an energy dependence consistent with the Regge expectation of $W^{0.22}$. It can be seen, however, that the cross section of the heavier J/ψ meson is significantly steeper with a value $\delta \approx 0.70$. This increase in the energy dependence of the cross section is indicative of a hard interaction and suggests that the mass of the vector meson may provide a hard scale.

The energy dependence of the vector meson production cross sections can also be studied in electroproduction. Figure 4.10 presents the energy dependence for ρ meson production [81] in several intervals in Q^2. The dependence of the cross section on energy is seen to steepen as Q^2 increases. This result suggests a transition from a soft interaction in photoproduction to an interaction displaying the characteristics of a hard process at large Q^2, the necessary hard scale being provided by Q^2.

The variation of the energy dependence of the cross section with other scales present in the process, such as the virtuality of the photon or the mass of the produced vector meson, indicates that the pomeron trajectory is not universal. The presence of such a hard scale enables the study of diffractive vector meson production in the framework of pQCD (see section 4.3.3). It may be expected that the momentum transfer at the proton vertex, t, provides a further hard scale. This will usually result in the break up of the proton. Events at such large momentum transfer would be extremely suppressed in Regge theory since the cross section for a pomeron with a sloping trajectory ($\alpha' \neq 0$) falls off very rapidly with increasing $|t|$ (see equation 4.12).

The diffractive photoproduction of vector mesons at large momentum transfer has been studied by both ZEUS [62] (ρ, ϕ, J/ψ) and H1 [63] (J/ψ only). The ZEUS measurements are for the energy range $80 < W < 120$ GeV and a photon virtuality restriction $Q^2 < 0.02$ GeV^2, which corresponds to $\langle Q^2 \rangle \sim 10^{-5}$ GeV^2. The selected data cover the range $M_Y \lesssim 25$ GeV. The corresponding region in x can be determined using

$$x = \frac{-t}{M_Y^2 - m_p^2 - t} \tag{4.29}$$

where m_p is the mass of the proton. The results are corrected to the fixed x range $0.01 < x < 1$, which is approximately the x range covered by the data at the average t value of the analysis. The accessible t range is $1.2 < |t| < 10$ GeV^2, with the exact upper bound depending on the vector meson considered.

The H1 measurement is performed in the energy range $50 < W < 150$ GeV for a photon virtuality $Q^2 < 1$ GeV^2 with $\langle Q^2 \rangle \sim 0.06$ GeV^2. Here a large rapidity gap is ensured by cutting on the elasticity variable z which is related to M_Y by

$$z \simeq 1 - (M_Y^2 - t)/W^2. \tag{4.30}$$

The elasticity is restricted to $z > 0.95$, corresponding to $M_Y \lesssim 30$ GeV. The data cover the range $2 < |t| < 30$ GeV^2 and significantly extend the earlier ZEUS result

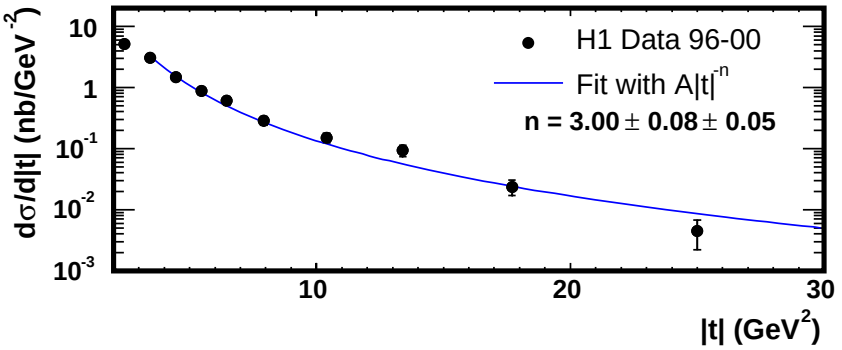

Figure 4.11: *The differential cross section $d\sigma/d|t|$ for J/ψ production [63]. The inner error bars show the statistical errors and the outer ones represent the sum of the statistical and systematic errors added in quadrature. The line represents the result of a fit to a power-law distribution $A|t|^{-n}$ in the region $|t| > 3.45$ GeV^2.*

for the J/ψ. In each case, both the t spectrum of the vector meson and the SDMEs are measured. The following outlines the main features of the results, beginning with the heavier J/ψ meson and then concentrating on the lighter ρ and ϕ mesons.

The H1 result for the differential J/ψ cross section as a function of t is presented in figure 4.11. It should be noted that, when the H1 analysis is repeated in the kinematic domain of the ZEUS measurement, good agreement is observed between the two results. For a hard production mechanism, the t cross section is expected to follow an approximate power-law dependence, with a power $n \sim 3-4$ [108]. To check this assumption, the data are fitted with a power-law parameterisation of the form $d\sigma/d|t| \sim |t|^{-n}$. The resulting power is $n = 3.00 \pm 0.08$ (stat.) $\pm$ 0.05 (syst.) which agrees well with the expectation. It should be noted, however, that the extracted power depends on the fitted t range, increasing systematically to a maximum value of $n = 3.78 \pm 0.17$ (stat.) $\pm$ 0.06 (syst.) for $|t| > 10.4$ GeV^2. Figure 4.12 shows the spin density matrix elements r^{04}_{00}, r^{04}_{1-1} and Re$\,[r^{04}_{10}]$ for J/ψ production as a function of t. In this case, the results of the ZEUS measurement are also shown and are in good agreement with those of H1 where the two sets overlap. It can be seen that, within experimental errors, the matrix elements are all compatible with zero. Hence

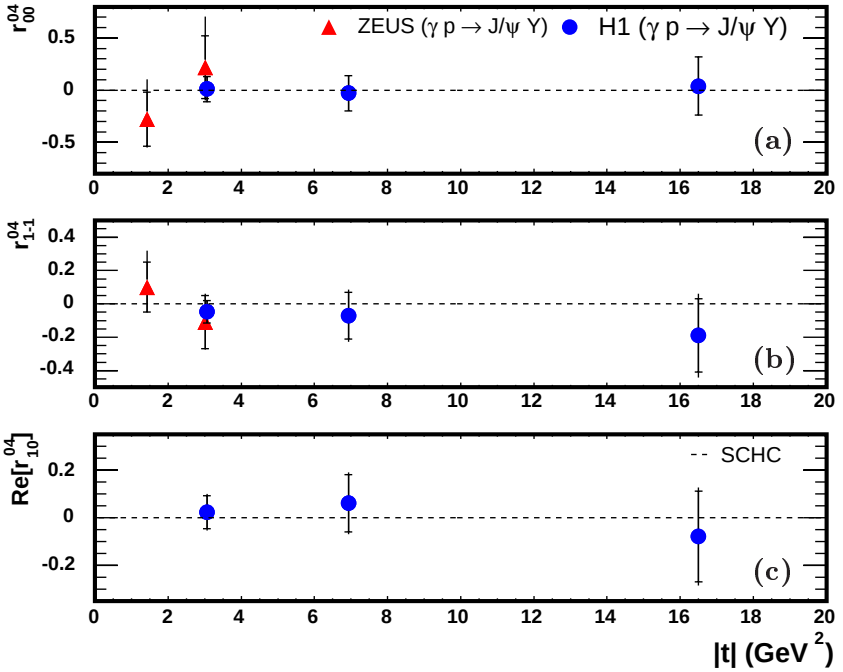

Figure 4.12: *The three spin density matrix elements (a) r^{04}_{00}, (b) r^{04}_{1-1} and (c) $\mathrm{Re}\,[r^{04}_{10}]$ for J/ψ production as measured by H1 [63] (circles) and ZEUS [62] (triangles) as a function of $|t|$. The inner error bars show the statistical errors and the outer ones represent the sum of the statistical and systematic errors added in quadrature. The dashed lines show the prediction from s–channel helicity conservation.*

J/ψ production is consistent with the expectation of SCHC.

It is the data on the light vector mesons that have proved particularly interesting. Figure 4.13 shows the differential cross section in t for both the ρ and the ϕ meson. In both cases the data are well described by a power law with a power $n = 3.21 \pm 0.04\,(\mathrm{stat.}) \pm 0.15\,(\mathrm{syst.})$ for the ρ and $n = 2.7 \pm 0.1\,(\mathrm{stat.}) \pm 0.2\,(\mathrm{syst.})$ for the ϕ. This is similar to the result observed for the J/ψ meson and all three data sets are consistent with a power $n \simeq 3$, in agreement with that expected for a hard production mechanism.

The extracted SDMEs for the ρ and the ϕ are shown in figure 4.14. In contrast to the heavier J/ψ meson, it can be seen that the results differ significantly from

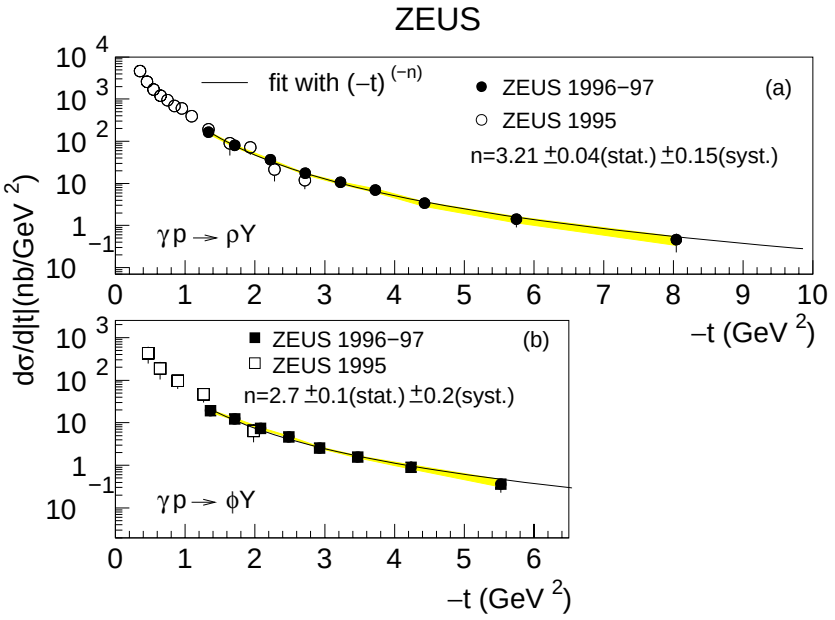

Figure 4.13: *The differential cross section $d\sigma/d|t|$ for (a) ρ and (b) ϕ mesons [62]. The inner error bars show the statistical errors and the outer ones represent the sum of the statistical and systematic errors added in quadrature. The shaded band indicates the correlated uncertainties due to the modelling of the dissociative system Y (an extra correlated uncertainty of $\pm 10\%$ is not shown). The lines represent the results of a fit to a power-law distribution $A|t|^{-n}$.*

zero, indicating a clear violation of SCHC. The relatively small value of the r_{00}^{04} matrix element indicates a low probability of producing a longitudinally polarised meson and suggests that the interaction is instead dominated by transverse mesons. Moreover, the finite negative value of r_{1-1}^{04} indicates the presence of a double helicity-flip contribution. It can be deduced that the leading contribution comes either from the no helicity-flip or double helicity-flip process.

Due to the clean experimental signature and the presence of the hard scale necessary for the application of pQCD calculations, diffractive photoproduction of vector mesons with large momentum transfer has been proposed as an ideal testing ground for BFKL dynamics [109, 110]. The theoretical challenge is to provide a

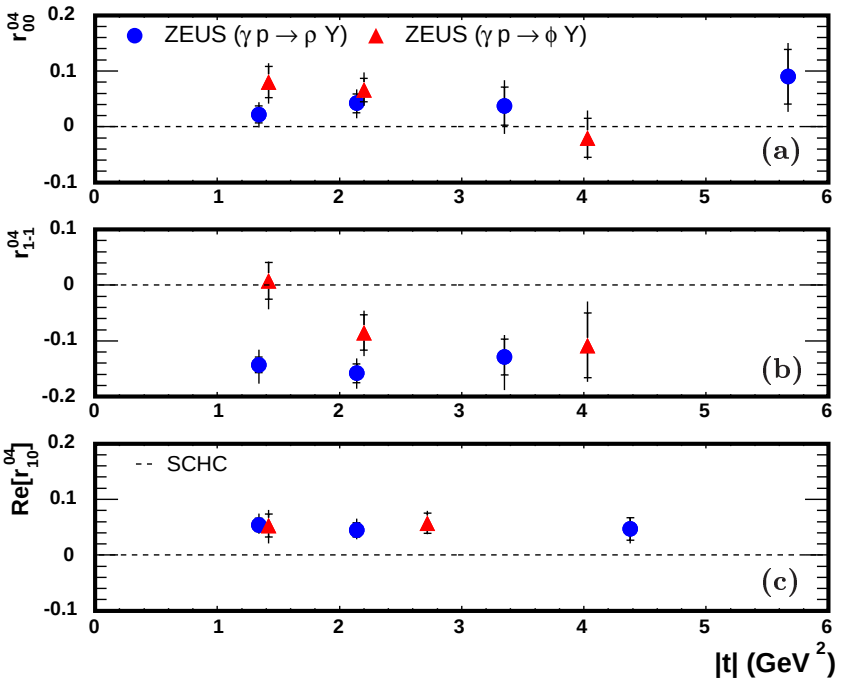

Figure 4.14: *The three spin density matrix elements (a) r^{04}_{00}, (b) r^{04}_{1-1} and (c) $\mathrm{Re}\,[r^{04}_{10}]$ for ρ (circles) and ϕ (triangles) production as a function of $|t|$ [62]. The inner error bars show the statistical errors and the outer ones represent the sum of the statistical and systematic errors added in quadrature. The dashed lines show the prediction from s−channel helicity conservation.*

simultaneous description of both the t spectrum and the SDMEs, in particular the largeness of r^{04}_{1-1} and the smallness of r^{04}_{00}.

4.3.3 Perturbative QCD Models

In the presence of a hard scale, the diffractive photoproduction of vector mesons, $\gamma p \to VY$, can be analysed in the framework of pQCD. In such models, the reaction is viewed as a series of three successive processes that are well separated in time (see figure 4.15): the photon fluctuates into a $q\bar{q}$ pair a long time before the interaction; the $q\bar{q}$ pair interacts with a single parton in the proton via a colour singlet exchange;

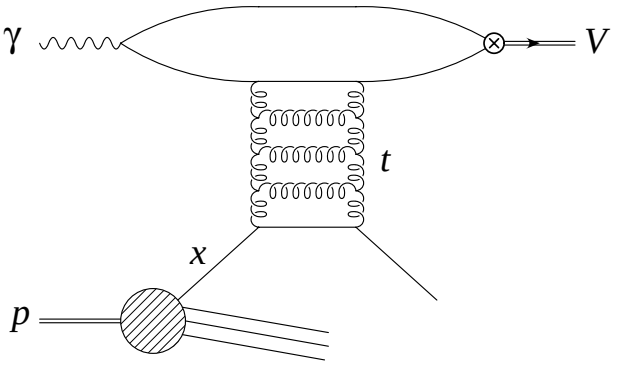

Figure 4.15: *Diffractive vector meson photoproduction at large momentum transfer [113].*

the $q\bar{q}$ pair recombine to form a bound vector meson a long time after the interaction. The probability of the photon fluctuating into the $q\bar{q}$ pair can be described in terms of a photon wavefunction $\Psi^{\gamma}_{q\bar{q}}$. At lowest order, the hard interaction between the $q\bar{q}$ pair and a parton in the proton proceeds via the exchange of two gluons in a colour singlet state. Higher order pQCD corrections result instead in the exchange of an effective gluon ladder. The production of the vector meson from the $q\bar{q}$ pair, which is a non-perturbative process, must be parameterised in terms of a meson wavefunction $\Psi^{V}_{q\bar{q}}$. Hence, the full amplitude can be written schematically as

$$M_{\gamma p \to VY} = \Psi^{\gamma}_{q\bar{q}} \otimes A^{p}_{q\bar{q}} \otimes \Psi^{V}_{q\bar{q}} \tag{4.31}$$

where $A^{p}_{q\bar{q}}$ represents the hard scattering amplitude. The first experimental data at sufficiently large $|t|$ from the HERA experiments has prompted significant interest in this process in recent years [109–111].

A leading order two gluon calculation has been performed by Ivanov *et al.* [111] based on a QCD-inspired wavefunction for the light mesons. Here, the current, or bare, quark mass is assumed and its contribution to the meson wave function is neglected. The results predict the vector meson production to be dominated by the single-flip amplitude at sufficiently large $|t|$. This is in contradiction with the experimental evidence (see section 4.3.2) but does, however, give rise to a $\sim |t|^{-3}$

dependence of the cross section. The experimentally dominant double-flip amplitude, on the other hand, predicts a steeper $\sim |t|^{-4}$ dependence. In order to explain this discrepancy, the authors postulated that the photon may fluctuate into a $q\bar{q}$ pair with a considerable chiral-odd[2] spin component. In principle, both chiral-even and chiral-odd components are possible but the latter vanishes in the limit that the quark mass may be neglected. If, however, the mass is interpreted as the constituent quark mass (the mass attributed to the quark in the potential of the vector meson) a significant chiral-odd contribution can survive. In this case, the chiral-odd amplitude with no helicity-flip is predicted to dominate for moderate $|t| \sim 10$ GeV^2.

Since diffraction occurs at values of s much larger than $|t|$, perturbative QCD corrections to the lowest order two gluon exchange will suffer from large logarithmic enhancements of the form $\log^n(s/|t|)$. This renders a leading order two gluon calculation insufficient and necessitates consideration of higher order terms in α_s [109]. At leading logarithm accuracy, these corrections can be summed to all orders in α_s using the BFKL equation (see section 3.3.2).

A leading logarithm approximation (LLA) BFKL calculation was carried out by Forshaw and Poludniowski [112] based on a non-relativistic delta-function approximation for the meson wavefunction. Here, the coupling constant α_s is treated as fixed and the constituent quark mass is used for the mesons. Perhaps surprisingly, the model is able to describe the t dependence of the light mesons as well as the heavy ones. The non-relativistic nature of the wavefunction prevents such a model from describing the deviations from SCHC and in order to improve this the BFKL equation must be coupled with a more realistic wavefunction approximation.

Recently, Poludniowski *et al.* [113] have performed a complete solution of the non-forward BFKL equation using a set of QCD light-cone wavefunctions for the vector meson [114]. Using this method, they are able, for the first time, to present analytical

[2]Chiral-even and chiral-odd configurations describe the coupling of the photon to a $q\bar{q}$ of opposite helicity and equal helicity, respectively.

solutions on the BFKL-evolved scattering amplitudes for all helicity combinations. The following outlines their prescription and compares the resulting predictions to the previous experimental measurements.

In the perturbative regime, where the size of the $q\bar{q}$ dipole is small, the BFKL pomeron couples predominantly to individual partons in the proton. This allows the cross section to be factorised into a product of partonic cross sections and PDFs,

$$\frac{d\sigma_{\gamma p\to VY}}{dtdx} = g(x,t)\frac{d\sigma_{\gamma g\to Vg}}{dt} + \sum_f [q_f(x,t) + \bar{q}_f(x,t)]\frac{d\sigma_{\gamma q\to Vq}}{dt}, \tag{4.32}$$

where $g(x,t)$ and $q_f(x,t)$ are the gluon and quark densities respectively, the latter being summed over the quark flavour f. At low x, the interaction with a gluon dominates. The differential cross section in t is then obtained by integrating over x,

$$\left\langle \frac{d\sigma_{\gamma p\to Vq}}{dt} \right\rangle = \int_{x_{min}}^{1} dx \frac{d\sigma_{\gamma p\to VY}}{dtdx}, \tag{4.33}$$

where x_{min} is the minimum value of x determined from the experimental cuts. For a particular t value, x_{min} may be calculated using equation 4.29. The resulting shape of the differential cross section in t is sensitive to the value of this cut.

The parton level cross section can be expressed in terms of the helicity amplitudes as:

$$\frac{d\sigma}{dt} = \frac{1}{16\pi\hat{s}}\left(|M_{++}(\hat{s},t)|^2 + |M_{+0}(\hat{s},t)|^2 + |M_{+-}(\hat{s},t)|^2\right) \tag{4.34}$$

where $\hat{s} = xW^2$ is the squared centre of mass energy involved in the partonic interaction. The value of W is taken according to the average value from the experimental data and Q^2 can be neglected in photoproduction. The SDMEs are constructed from the helicity amplitudes as stated in equations 4.25–4.27 and the parton level quantities are then integrated over x with the appropriate cuts in an analogous way to equation 4.33.

The production of the vector meson is factorised from the hard scattering process and, due to the small size of the dipole, the relevant hadronic matrix elements can be expanded on the light-cone. All expansions are performed up to twist-3, i.e.

next-to-leading twist[3], which is the lowest order able to accommodate a non-zero r^{04}_{1-1} matrix element. Instead of performing a similar separation for the photon, the QED coupling of the photon to the $q\bar{q}$ pair is utilised. The hard scattering amplitude itself can be written in the impact factor representation as

$$A = \Phi^{\gamma \to V} \otimes K_{BFKL} \otimes \Phi^{q \to q} \tag{4.35}$$

where Φ are the impact factors representing the coupling of the pomeron to the indicated vertices and K is the BFKL four-gluon amplitude, which describes the evolution of the gluon ladder. The constituent quark mass, $m = m_V/2$, is used to enhance the coupling of the photon to the chiral-odd $q\bar{q}$ configuration, thereby producing a strong transverse polarisation as supported by previous data.

The leading logarithm nature of the calculation prevents an absolute prediction for the normalisation of the cross sections, due to the presence of an undefined energy scale Λ. In [113], this scale is allowed to run with t according to $\Lambda^2 = m_V^2 - \gamma t$, where γ is a free parameter. The value of α_s is fixed since this is appropriate in the LLA and has proved successful in describing previous data [115]. There are actually two factors of the strong coupling, α_s^{IF} and α_s^{BFKL}, which describe the coupling of the two gluons to each impact factor and the gluon couplings within the ladder respectively. Both of these values are free parameters of the model, although it should be noted that, as ratios, the spin density matrix elements do not depend on α_s^{IF}.

The best-fit BFKL predictions for the ρ meson are presented in figures 4.16 and 4.17, along with the results of the lowest order two gluon exchange for comparison. Using a natural choice of parameters ($\alpha_s^{IF} = 0.17$, $\alpha_s^{BFKL} = 0.25$ and $\gamma = 1$), the BFKL model is able to provide a good description of the t dependence. The prediction from the two gluon exchange with a fixed strong coupling constant is seen to be too flat. Running the coupling can fix this problem and enables a good

[3]Each order in twist corresponds to a suppression by a factor $(m_V/|t|)$.

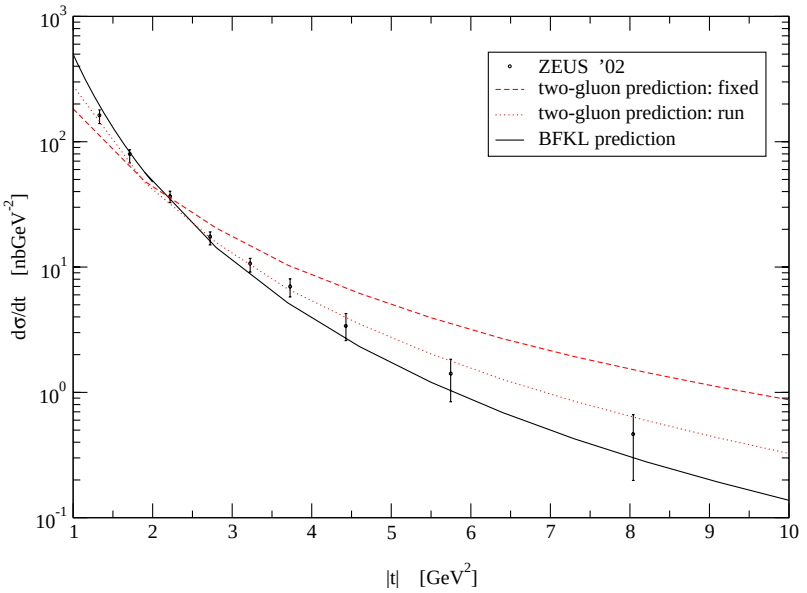

Figure 4.16: *The t dependence of the differential cross section for ρ photoproduction as measured by the ZEUS experiment (points). The data are compared to the predictions from two gluon exchange, with fixed (dashed line) and running (dotted line) coupling, and BFKL exchange with fixed coupling (solid line) [113].*

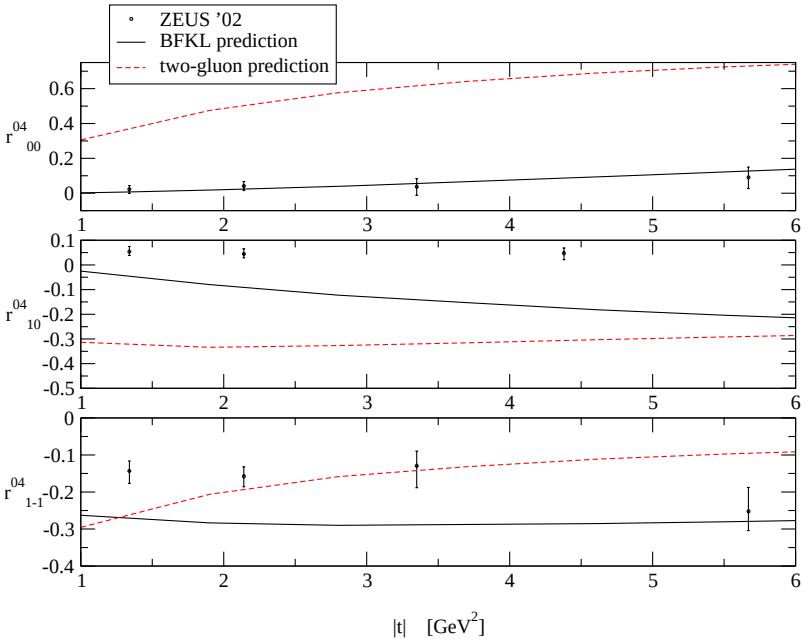

Figure 4.17: *The spin density matrix elements for ρ photoproduction as measured by the ZEUS experiment (points). The data are compared to the predictions from two gluon exchange (dashed line) and BFKL exchange (solid line) [113].*

fit to be obtained. However, even using the constituent quark mass, it can be seen that the two gluon exchange completely fails to reproduce the observed dominance of transverse vector meson production.

In contrast, the BFKL model does predict a predominantly transverse production with a hierarchy of helicity amplitudes given by: $|M_{++}| > |M_{+-}| > |M_{+0}|$. However, the results show that, while r_{00}^{04} is well described, the model prediction for r_{1-1}^{04} is too negative and it gives the wrong sign for $\mathrm{Re}\,[r_{10}^{04}]$. The underestimation of r_{1-1}^{04} can be understood to some extent since M_{+-} vanishes at leading twist and hence the model is only leading order in this quantity. The main obstacle to providing a good fit is, therefore, the inability to describe r_{10}^{04}, in particular the incorrect sign.

The difficulty in describing r_{10}^{04} suggests that the longitudinal helicity component, although reduced by BFKL resummation, is still not sufficiently under control. It is noteworthy that unnaturally increasing the quark mass gives rise to a suppression of the longitudinal helicity component with respect to the transverse without any significant change in the shape of the t cross section. In particular, for large enough m ($m \sim m_\rho$ where m_ρ is the mass of the ρ meson) the contribution from the M_{+0} amplitude is observed to switch sign, leading to a prediction for r_{10}^{04} that has the same sign as the experimental data [113]. Although such an increase in m provides an improved description of the data, it is difficult to explain a quark mass so far from the constituent mass. However, it should be noted that increasing the mass effectively suppresses the contribution from large $q\bar{q}$ dipoles and, hence, the data may suggest that the contribution from large dipoles is more strongly suppressed than the current model predicts. Due to the exclusive nature of the final state, there is a Sudakov suppression of radiation off the quark and antiquark and, given that large dipoles radiate more strongly, the authors of [113] postulate that such Sudakov factors may explain the reduced contribution from large dipoles [116]. However, this effect remains to be quantified.

Similar results are obtained for the ϕ meson. In contrast, for the heavier J/ψ

meson, the BFKL model is able to provide a good description of both the t distribution and the SDMEs, although it should be noted that the data have larger uncertainties.

Although the introduction of a large chiral-odd component in the theoretical analyses has proved a significant step forward, there is clearly still room for improvement. Coupled to this is the need for better experimental data to constrain the models. Here, the main goal is to extend the data out to larger values of $|t|$ for the light vector mesons and to reduce the uncertainties, in particular for the J/ψ.

Chapter 5

Data Reconstruction, Selection and Simulation

The subject of this thesis is the diffractive photoproduction of ρ mesons with large momentum transfer at the proton vertex,

$$\gamma p \to \rho Y. \tag{5.1}$$

The system Y represents either an elastically scattered proton or a low mass dissociated proton system. However, for the range of $|t|$ covered in this analysis, the contribution from elastic ρ production may be neglected due to its steep t dependence [81, 98]. The ρ is identified by its subsequent decay into two charged pions

$$\rho \to \pi^+\pi^-. \tag{5.2}$$

The cross section for this process is measured differentially as a function of t and, in order to provide information on the helicity structure of the interaction, the spin density matrix elements are extracted.

5.1 Selection Criteria

This analysis is based on data collected by the H1 experiment during the 2000 running period. Only in this period was a suitable trigger available to collect the data. The data are selected by applying a series of cuts, the purpose of which is to select good quality events in the kinematic regime of interest and remove unwanted background processes. These cuts are detailed in the following sections.

5.1.1 Run Selection

Data taking runs are classified as good, medium or poor quality depending on the high voltage and readout status of the detector components. Only those runs designated as good or medium quality are considered here. In addition, all selected runs are required to contain a minimum integrated luminosity of 0.2 nb^{-1}. Towards the end of 2000, a special class of runs were taken with the interaction vertex shifted in the forward direction. These runs are not included in the present analysis.

All detector components relevant to the analysis are required to be fully operational. The tracking detectors (CJC1, CJC2, CIP, COP, CIZ and COZ) and the LAr calorimeter are required to reconstruct the decay products of the ρ meson, while the 44 m electron tagger is necessary to detect the scattered electron. In addition, the luminosity system is essential for an accurate measurement of the luminosity and the time of flight system is needed to reduce non-ep background. In order for the events to be kept the subtrigger used in this analysis (see section 5.1.2) must also be active. For this reason, several further run periods are excluded due to known problems with the trigger elements that make up this subtrigger.

P_{109}	1	2	3	4	5	6	7	8	9	10
$\mathcal{L}$ (pb^{-1})	13.74	4.95	3.97	4.11	2.99	2.51	1.79	0.96	0.79	0.48

Table 5.1: *The integrated luminosity (unprescaled) collected as a function of the prescale of the s109 subtrigger.*

5.1.2 Subtrigger Selection

The data used in this analysis are collected by the subtrigger s109, which selects photoproduction events based on the detection of a scattered electron candidate in the 44 m electron tagger. The subtrigger can be expressed in terms of the component trigger elements as[1]

$$\text{s109} \quad = \quad \text{zVtx\_Cls \&\& DCRPh\_Ta \&\& !LAr\_IF \&\& etag\_44 \&\& VETOs} \quad (5.3)$$

where the individual elements have been described in detail in section 2.8. In addition to the trigger element from the 44 m electron tagger (etag_44), extra requirements must be placed on the information received from the central detector in order to reduce the event rate to an acceptable level. Consequently, the central tracking detectors are used to restrict the sample to those events containing at least one central track (DCRPH_Ta) and having a sharp peak in the z-vertex distribution (zVtx_Cls). The rate is then further reduced by limiting the energy deposited in the forward region of the LAr calorimeter (!LAr_IF). This has the consequence of limiting the proton remnant to low masses. The VETO conditions consist of extra timing requirements designed to reject the majority of non-ep background and are assumed to be 100% efficient. The prescale factors for the s109 subtrigger, along with the integrated luminosity collected for each, are shown in table 5.1. Over the period of interest, the subtrigger is prescaled by an average factor $\langle P_{109} \rangle \approx 1.8$, such that the integrated luminosity collected, after applying the prescale, is $\mathcal{L} = 20.1$ pb^{-1}.

[1]The symbol && indicates a logical AND.

5.1.3 Photoproduction Selection

Photoproduction events are selected by requiring an energy deposit of more than 15 GeV in the 44 m electron tagger. This energy deposit forms the scattered electron candidate and, consequently, restricts the virtuality of the exchanged photon to $Q^2 < 0.01$ GeV^2. The energy cut mirrors that applied by the high $|t|$ vector meson finder running on the L4 trigger (see section 2.8) and ensures the electron is efficiently triggered [28]. Additionally, it is required that there is no deposit in the photon detector with energy $E_{PD} > 0.6$ GeV, in order to reject background events where the tagged electron is faked by an overlapping Bethe-Heitler event [117]. Events with scattered electron candidates in the LAr or SpaCal are also vetoed.

The average acceptance of the ET44 as a function of y for the running period considered is shown in figure 5.1. Due to the poor energy resolution of the ET44, y is entirely reconstructed from the ρ meson via the Jacquet-Blondel method [118]:

$$y_{JB} = \frac{E_\rho - P_{z,\rho}}{2E_e} \tag{5.4}$$

where E_e is the energy of the incoming electron and E_ρ and $P_{z,\rho}$ are the energy and longitudinal momentum of the ρ meson respectively. Using equation 3.27, the γp centre of mass energy can then be calculated by $W_{JB} \approx \sqrt{y_{JB} s}$. In order for the scattered electron to lie well within the acceptance of the ET44, while simultaneously allowing the pion candidates to be detected inside the central tracker (see section 5.1.4), W is restricted to $75 < W_{JB} < 95$ GeV. This corresponds to a y range of $0.055 < y_{JB} < 0.089$.

Since the acceptance of the electron taggers is highly dependent on the HERA beam optics, which vary for each run, they are not included in the simulation of the H1 detector. Consequently, information on the tagged electron is not available by default in any MC model. It is therefore necessary to correct the reconstructed MC for the acceptance of the ET44 and the effect of the energy cut applied above.

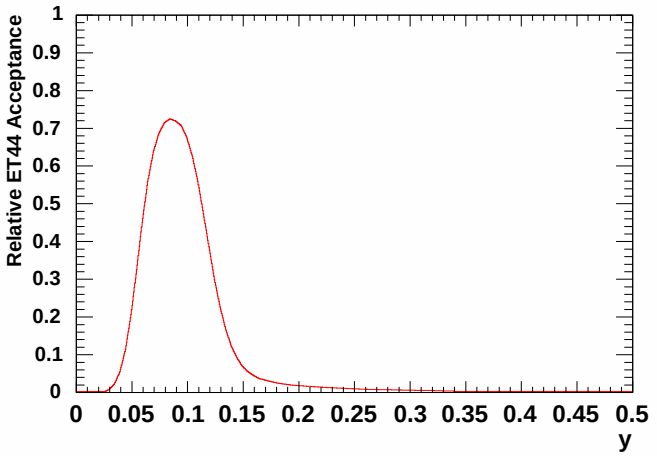

Figure 5.1: *The luminosity weighted relative acceptance of the 44 m electron tagger (for the range $Q^2 < 0.01$ GeV^2) as a function of y over the running period considered.*

The run-by-run acceptance of the ET44 has been measured and parameterised using a sample of Bethe-Heitler events, following the procedure described in [28]. This involves measuring the angular tilt of the electron beam using the PD and then tuning the MC simulation to the data by varying the electron beam offset. Using these values, the relative acceptance of the ET44 for events with a tagged electron, integrated over the range $Q^2 < 0.01$ GeV^2, can be determined. The resulting parameterisation was used to calculate the luminosity averaged relative acceptance, as a function of y, for the period of interest, as shown in figure 5.1. This distribution is used to weight the detector level MC events, depending on the generated y value.

In order to apply the energy cut in the MC, it is necessary to reproduce the energy distribution observed in the ET44. Such a distribution can be simulated using the correlation between the energy in the 44 m tagger, E_{44}, and the y value of the event observed in the data. Based on the reconstructed y value of the MC event, an energy can then be assigned according to this correlation using a 'hit or miss' technique. Firstly, a correlation matrix between y and E_{44} is formed from the data sample, see figure 5.2. Each entry in this matrix represents the number of data events in a particular range of y and E_{44}, $N(y, E_{44})$, normalised to lie between 0 and

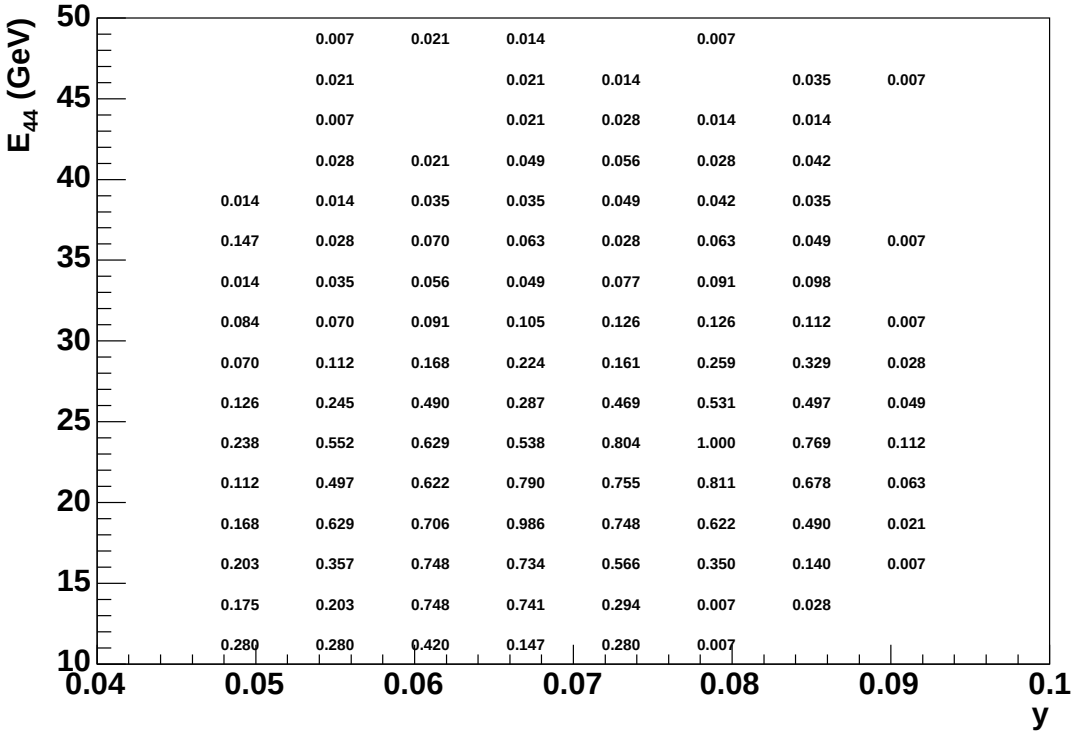

Figure 5.2: *The normalised correlation matrix between the energy deposited in the 44 m electron tagger, E_{44}, and y.*

1 by dividing by the maximum such value, $N(y, E_{44})_{max}$. Then, for each MC event, an energy is chosen randomly within the range of interest and allotted a random number, R, chosen uniformly between 0 and 1. This is compared to the entry in the correlation matrix at the appropriate energy and the y value corresponding to the event. If the random number is less than the value at that position in the matrix,

$$R < \frac{N(y, E_{44})}{N(y, E_{44})_{max}}, \tag{5.5}$$

the chosen energy is assigned to the event. Otherwise, a new energy is picked and the procedure repeated until the condition in equation 5.5 is fulfilled and an energy determined. The resulting description of the ET44 energy spectrum is presented in figure 5.3 before the cut at 15 GeV. All other cuts, as summarised in section 5.1.7, are applied along with the acceptance correction described above. A reasonable description of the energy distribution is observed allowing the MC to adequately simulate the effect of the energy cut.

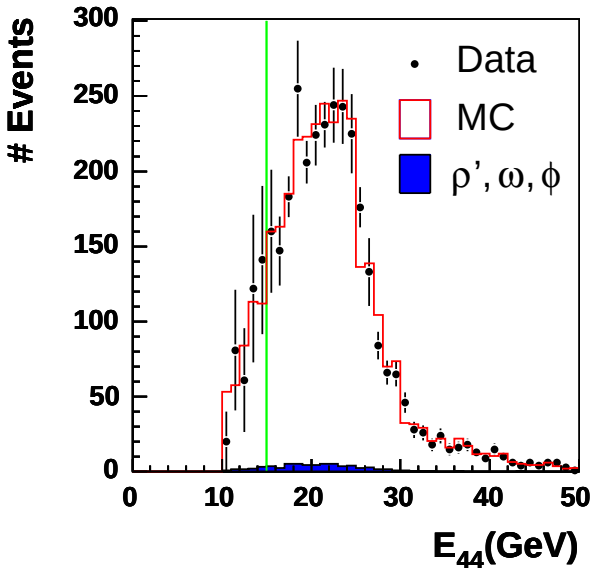

Figure 5.3: *The acceptance corrected energy spectrum of the 44 m electron tagger after all the reconstructed level cuts, except that on the energy itself which is indicated by the vertical line, are applied. The data (points) are compared to the sum of the MC contributions (open histogram) for the ρ signal and the remaining ω, ϕ and ρ' background contribution (shaded histogram). The error bars show the statistical uncertainty on the data.*

5.1.4 Track Selection

The ρ meson is identified via its decay into two charged pions, which are detected as tracks reconstructed in the central tracking detector. Hence, in order to select potential ρ candidates, events are required to contain exactly two good central tracks of opposite charge originating from the primary vertex. Here, good refers to those tracks passing a set of quality criteria known as the "Lee West" selection criteria, described in detail in [119]. For central tracks, the main requirements are a starting radius inside CJC1, $R_{start} < 50$ cm, and a length of more than 10 cm (5 cm) for tracks with a polar angle below (above) 150°. These tracks form the pion candidates and no other tracks, central or otherwise, are allowed.

Both pions are required to lie within the polar range $20° < \theta_\pi < 155°$, such

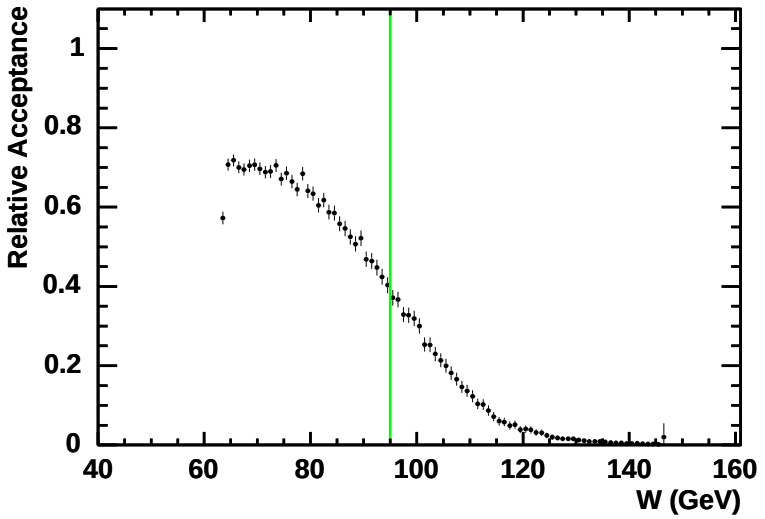

Figure 5.4: *The relative acceptance, as a function of W, for the two pion candidates to lie in the angular range $20^\circ < \theta < 155^\circ$. The vertical line indicates the position of the upper cut applied on W (at the lower end it is already limited to $W > 75$ GeV due to the acceptance of the ET44).*

that they may traverse the whole of CJC1. The upper bound further ensures that the tracks cross the COP, which is necessary for triggering purposes. The transverse momentum of the pions, p_t^π, must also exceed 150 MeV, to prevent the tracks curling up on themselves. Together, these cuts restrict the tracks to a region where the track reconstruction is well understood and well described by the MC. Additionally, the transverse momentum of the pion with the largest p_t, known as the lead pion, is required to be greater than 450 MeV. This avoids large uncertainties associated with the efficiency of the DCRPh_Ta trigger element in the threshold region (see section 6.3). In order to reduce the background due to non-ep interactions, the z position of the vertex reconstructed from the two tracks must lie within a window of 35 cm either side of the nominal interaction point.

The polar angle of the decay pions is related to the centre of mass energy W. Consequently, the angular cut limits the geometrical acceptance in W, causing it to decrease towards the lower and higher values of W. The resulting geometrical acceptance for the two tracks to lie in the range $20^\circ < \theta < 155^\circ$ is shown in

figure 5.4. It should be noted that this does not include the acceptance of the electron tagger. In order to prevent large uncertainties in the model description, it is necessary to avoid the region of W where the acceptance falls off most rapidly. Since the exact position of this cut-off is somewhat arbitrary, it was chosen to limit W to below 95 GeV, which keeps the relative acceptance above 40%. Coupled with the acceptance of the ET44 (see section 5.1.3), this confines W to the range $75 < W < 95$ GeV.

In order to provide the hard scale necessary for the application of pQCD calculations, $|t|$ must be sufficiently large. In photoproduction, t is well approximated by the negative transverse momentum squared of the ρ meson, $t \approx -(p_t^\rho)^2$, where the ρ four vector is formed from the vector addition of the individual pion four vectors. The present analysis is limited to the region $|t| = (P_t^\rho)^2 > 1.5$ GeV^2.

5.1.5 Selection on Energy Deposits in the LAr Calorimeter

The LAr calorimeter is used to identify additional energy deposits, or clusters, not associated to the tracks of the two pion candidates. This enables the rejection of background where the final state consists of two charged particles plus an additional neutral particle and, at the same time, is used to restrict the analysis to the diffractive regime, $M_Y \ll W$.

Such energy deposits can, however, also be the result of electronic noise in the readout of the calorimeter and it is important not to reject events on the basis of this inherent noise. Although calorimeter cells which have an energy consistent with noise are omitted during reconstruction [120], it is not sufficient. The remaining noise can be excluded by ignoring low energy isolated clusters. In line with previous analyses, e.g. [121], energy deposits below 400 MeV are considered as noise and consequently disregarded.

In order to determine whether an energy deposit is associated to the pion can-

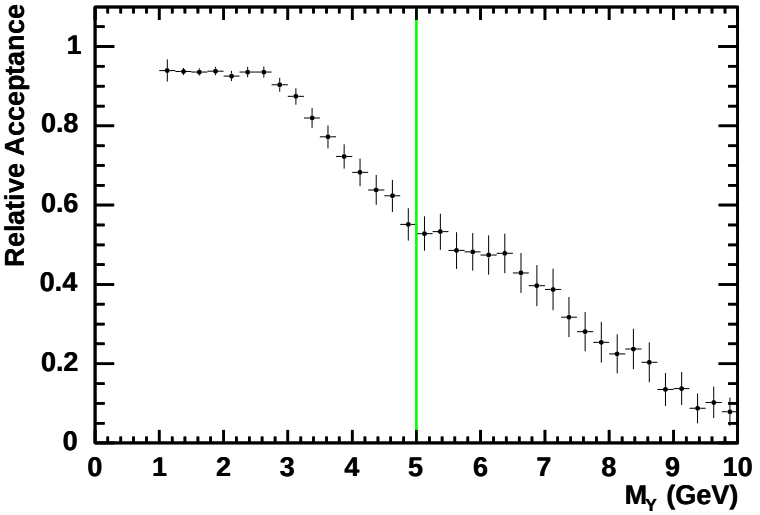

Figure 5.5: *The effect, as determined from the MC simulation, on the acceptance as a function of M_Y of rejecting events with an energy deposit in the LAr, that is not associated to the two pion tracks, which exceeds* 400 MeV. *All other selection criteria are applied. The vertical line represents the largest allowed M_Y value.*

didates, their impact position on the surface of the calorimeter is calculated, taking into account the curvature of the tracks due to the magnetic field. A cylinder is then constructed around the direction of the track, having a radius of 25 cm in the electromagnetic part and 50 cm in the hadronic part (the latter reflecting the greater spread of hadronic showers). An energy deposit is taken to be associated to the track if its centre of gravity lies within this cylinder [122]. Any event with an energy deposit of above 400 MeV reconstructed in the LAr, which is not associated to the tracks of the two pion candidates, is rejected.

In the forward region, energy deposits not associated to tracks can result from the break up of the proton, provided the dissociative mass, M_Y, is large enough. Consequently, the rejection of events containing such energy deposits limits the acceptance in M_Y, in particular, leading to a reduction in acceptance at high M_Y. It is necessary to correct the data to a particular M_Y range in order to quote a well defined cross section. Figure 5.5 shows the effect on the acceptance in M_Y of rejecting events, which would otherwise pass all remaining selection criteria, that contain an

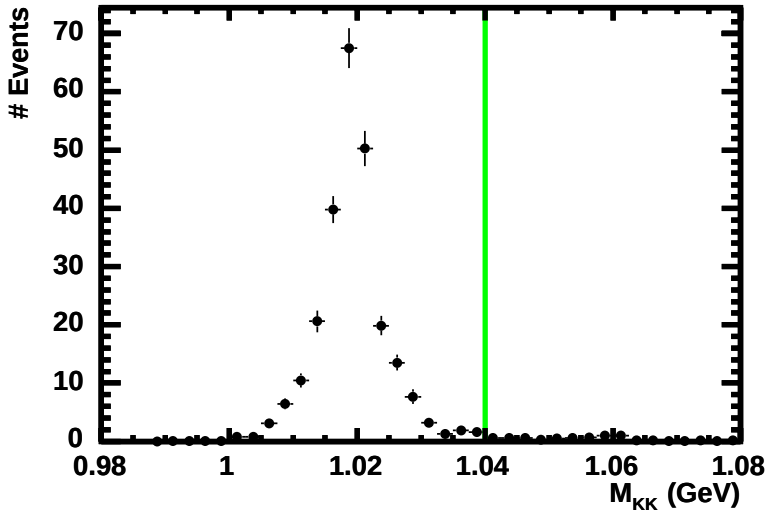

Figure 5.6: *The reconstructed M_{KK} invariant mass distribution for the proton dissociative ϕ MC sample. All selection criteria except for of the cuts on the invariant masses are applied. The vertical line represents the largest allowed M_{KK} value.*

energy deposit of above 400 MeV not associated to a track. The acceptance is determined from the MC simulation for proton dissociative ρ meson production. In order to maintain an acceptance of above 50%, this analysis is restricted to the region $M_Y < 5$ GeV and the data is subsequently corrected to this domain using the MC simulation (see section 5.1.8). This low proton remnant mass ensures $M_Y \ll W$, which limits the events to the diffractive regime and effectively produces a large rapidity gap (see equation 4.20).

5.1.6 Invariant Mass Selection

Restricting the invariant mass of the two tracks allows the selection of events corresponding to the signal process, while at the same time reducing the backgrounds described in section 5.3.

The diffractive production of ϕ mesons with their subsequent decay into K^+K^- produces a signal in the detector that is identical to the ρ meson but, due to the heavier mass of the ϕ (≈ 1020 MeV), should have a significantly different invariant

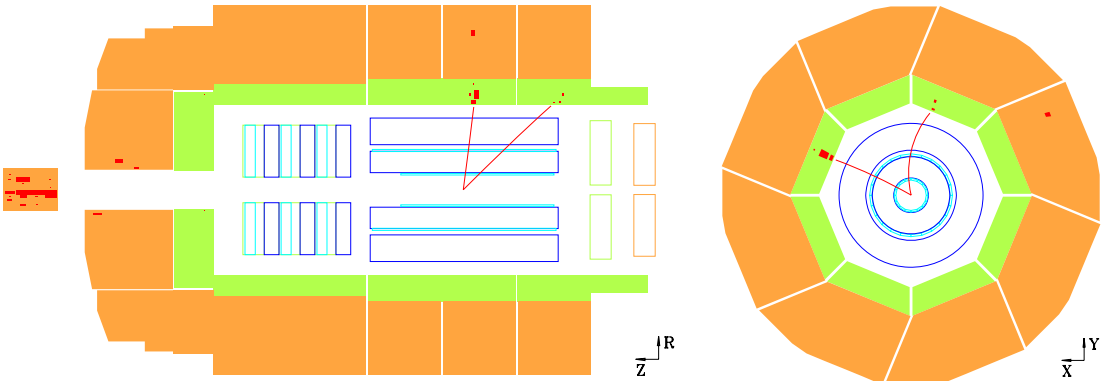

(a) **(b)**

Figure 5.7: *An example of a selected* $\rho \to \pi^+\pi^-$ *event in (a)* $r-z$ *and (b)* $r-\phi$ *view.*

mass. Consequently, this background can be excluded by rejecting events based on the invariant mass reconstructed under the assumption that the two tracks are kaons, M_{KK}. Taking into account the width of the ϕ meson, as shown in figure 5.6, a suitable cut is $M_{KK} > 1.04$ GeV, .

Events corresponding to the resonant production of two pions are selected by requiring the invariant mass, reconstructed under the assumption that the two tracks are pions, to be in the range $0.6 < M_{\pi\pi} < 1.1$ GeV, spanning the ρ mass. In addition, this cut reduces the contamination due to open pion pair production (see section 6.4) and eliminates background coming from the decay of the ρ' into two charged particles.

5.1.7 Selection Summary

The full set of reconstructed level cuts used to select the event sample for this analysis is summarised in table 5.2. The number of final selected events is 2628, an example of which is shown in figure 5.7.

Electron candidate	$E_{44} > 15$ GeV
	$E_{PD} < 2$ GeV
	$75 < W_{JB} < 95$ GeV
	Veto additional electrons
Pion candidates	$N_{tracks} = 2$
	Opposite Charge
	Both from primary vertex
	$\|z_{vtx}\| < 35$ cm
	$20^\circ < \theta_\pi < 155^\circ$
	$p_t^\pi > 150$ MeV
	$p_t^{lead\ \pi} > 450$ MeV
	$\|t\| = (P_t^\rho)^2 > 1.5$ GeV
LAr Calo.	E(Neutral LAr cluster) < 400 MeV
Invariant mass	$0.6 < M_{\pi\pi} < 1.1$ GeV
	$M_{KK} > 1.04$ GeV

Table 5.2: *A summary of the event selection.*

5.1.8 Kinematic Regime

In order to correct the data to a well defined kinematic regime, the kinematic cuts applied at the detector level, which reflect both the acceptance of the H1 detector and the theoretical phase space requirements, must be mirrored on the generator level of the MC. These cuts define the kinematic domain of the measured cross sections and are as follows:

- $Q^2 < 0.01$ GeV^2
- $75 < W < 95$ GeV
- $1.5 < |t| < 10.0$ GeV^2

- $M_Y < 5$ GeV.

The Q^2 and W ranges represent the acceptance of the 44 m electron tagger and, in the latter case, also the central tracker. The cut on t ensures a large momentum transfer, which provides the hard scale necessary for the application of pQCD calculations. Finally, the restriction in M_Y limits the events to the diffractive regime. It should be noted that the diffractive nature of the events is imposed at the reconstructed level by the absence of any further activity, other than the two pion candidates, in the LAr calorimeter and the data is then subsequently corrected back to a well defined kinematic region by applying this cut on M_Y at the generator level of the MC simulation. Such a tight restriction on M_Y is necessary due to the restriction on the energy in the forward region of the LAr calorimeter imposed by the !LAr_IF element of the trigger. On allowing the proton remnant system to enter the LAr, it is observed that the efficiency of the !LAr_IF trigger element is highly dependent on the mass of the proton remnant, giving rise to a unacceptably large systematic uncertainty upon varying M_Y. Preventing the proton remnant from dissociating into the LAr ensures the !LAr_IF efficiency is 100% and prevents this large uncertainty. Theoretically, such a tight restriction on the proton remnant mass ensures one does not approach $M_Y \sim W$ and, therefore, remains well within the diffractive regime.

5.2 The DIFFVM Monte Carlo Generator

The DIFFVM event generator [38] simulates the diffractive production of vector mesons based on the framework of Regge theory and the VDM (see section 3.4). In this approach, the incident electron emits a photon which fluctuates into a virtual vector meson before interacting diffractively with the proton via pomeron exchange (at high centre of mass energies, $W \gtrsim 10$ GeV, the contribution due to reggeon

exchange is negligible). The generator includes the possibility of proton dissociation and implements a detailed description of the dissociative final state.

Events are generated in the kinematic range $Q^2_{min} < Q^2 < Q^2_{max}$ and $W_{min} < W < W_{max}$, chosen by the user. The Q^2 and W dependencies are implemented according to the VDM-inspired parameterisation

$$\sigma_{\gamma p}(Q^2, W) \propto \left(\frac{W}{W_0}\right)^{4\epsilon} \left(1 + \frac{Q^2}{m_V^2}\right)^{-a} \tag{5.6}$$

where $\epsilon = \alpha_{IP}(0) - 1$ and a are free parameters to be chosen by the user. Here ϵ is taken to be 0.08, in accordance with the Donnachie and Landshoff parameterisation of the pomeron [78], while a is set to 2.4, as measured previously by H1 [86].

The invariant mass of the generated vector meson is assumed to follow a non-relativistic Breit-Wigner distribution. For the ρ meson, this is subsequently reweighted to the more appropriate relativistic formula. Possible distortion of the ρ signal, known as skewing, arising from contamination due to open pion pair production is also taken into account where necessary. The parameterisation of the invariant mass distribution is described in detail in section 6.4.

The t dependence is taken as an exponential

$$\frac{d\sigma}{dt} \sim e^{bt} \tag{5.7}$$

where b is a free parameter. In the current analysis, this exponential is reweighted to a power law $d\sigma/dt \sim |t|^{-n}$, more suitable for describing the high $|t|$ regime. The value of n for the ρ meson is taken from the results presented here and the other vector mesons are assumed to follow the same distribution.

In the case of proton dissociation, the dependence of the cross section on the mass of the dissociative system M_Y is parameterised as

$$\frac{d\sigma}{dM_Y^2} \propto \frac{f(M_Y^2)}{M_Y^{2(1+\epsilon)}}. \tag{5.8}$$

The function $f(M_Y^2)$ describes the low mass behaviour, including the possibility of resonances, and is the result of a fit to diffractive proton-deuteron data [123]. The

subsequent fragmentation and hadronisation of the dissociative system is performed by the JETSET program [124]. It should be noted that, when the proton dissociates, the minimum generated t value is no longer negligible and can be approximated by

$$t_{min} \approx \frac{(m_V^2 + Q^2)(M_Y^2 - m_p^2)}{W^2}. \tag{5.9}$$

The ratio of the cross sections for longitudinally and transversely polarised photons is implemented according to

$$R(Q^2) = \frac{\xi \frac{Q^2}{M_V^2}}{1 + \xi\chi\frac{Q^2}{M_V^2}} \tag{5.10}$$

where χ is a purely phenomenological parameter. For $\chi = 0$ this reduces to the VDM formula quoted in equation 3.32. Here the free parameters are taken to be $\xi = 0.42$ and $\chi = 1.11$, as determined in [121].

For a two-prong vector meson decay, DIFFVM generates the angular decay distributions according to the SCHC approximation. In order to take into account the observed violation of SCHC, the distribution for the ρ meson is reweighted to the form given in equation 4.22 with the values of r_{00}^{04}, r_{1-1}^{04} and $\mathrm{Re}\,[r_{10}^{04}]$ from the present analysis.

In this analysis, the DIFFVM event generator is used to simulate the diffractive production of ρ, ρ', ω and ϕ mesons[2].

[2]The detailed structure [106] of the states previously described as the $\rho'(1600)$ meson is not relevant for the present study. The name ρ' is, therefore, used to imply both the $\rho'(1450)$ and the $\rho'(1700)$. In the DIFFVM simulation, the ρ' mass and width are taken as 1450 MeV and 300 MeV, respectively.

5.3 Background Processes

Background processes are those which can mimic the signal process and may, therefore, contaminate the sample of events selected. Two different classes of background must be considered: those which directly imitate the signal process through the production of a typologically identical final state and those which fake the final state of interest due to the failure to detect one or more particles. In this analysis the main backgrounds arise from diffractive production of ω, ϕ and ρ' mesons. The contributions from the different vector mesons are estimated using Monte Carlo simulations, which are normalised according to previous measurements of the ω, ϕ and ρ' production cross sections relative to that of the ρ.

5.3.1 Diffractive ω and ϕ Production

The diffractive photoproduction of ω and ϕ mesons can mimic the signal process via both the above methods, depending on the decay mechanism of the vector meson. Firstly, the vector meson can directly mimic the two-prong ρ signature by its decay into exactly two charged particles:

$$\omega \rightarrow \pi^+\pi^- \quad (1.70\ \%) \tag{5.11}$$

$$\phi \rightarrow K^+K^- \quad (49.1\ \%) \tag{5.12}$$

where the number in parentheses indicates the branching fraction for that particular decay. In the case of the ϕ meson, this channel is suppressed by applying a cut on the invariant mass reconstructed under the assumption that the two tracks are kaons (M_{KK}). For the ω meson, such a cut is prevented by the closeness of its mass (≈ 783 MeV) to that of the ρ, making such a decay indistinguishable from the signal process. In addition, the ω and ϕ mesons can decay into two charged particles plus

an additional neutral particle by way of the channels

$$\omega \rightarrow \pi^+\pi^-\pi^0 \quad (89.1\ \%) \tag{5.13}$$

$$\phi \rightarrow \pi^+\pi^-\pi^0 \quad (15.4\ \%) \tag{5.14}$$

$$\phi \rightarrow K^0_S K^0_L \quad (34.0\ \%) \tag{5.15}$$

where the second reaction may proceed either directly or through an intermediate ρ resonance and the K^0_S decays via

$$K^0_S \rightarrow \pi^+\pi^-. \tag{5.16}$$

These processes can fake the ρ signal if the K^0_L or the photons resulting from the decay of the π^0 remain undetected. This can happen if the energy of the neutral particles is deposited in a crack in the detector, associated to a charged pion track or is less than the 0.4 GeV noise threshold.

The background due to ω and ϕ mesons is simulated using the DIFFVM Monte Carlo generator with the relative cross sections fixed from the measured ratio of the production cross section to that of the ρ. For the ω meson, the ratio is fixed to the value $\sigma_\omega/\sigma_\rho = 0.106 \pm 0.011$ (stat.) ± 0.016 (syst.) obtained by the ZEUS experiment in photoproduction at $|t| < 0.6$ GeV^2 [101]. This ratio is consistent with the SU(4) prediction in equation 3.31 and is almost flat with Q^2, although little is known about its t dependence. In contrast, the ratio of the cross section for the ϕ to the ρ increases with both Q^2 and $|t|$. Consequently the ratio is fixed to the photoproduction value $\sigma_\phi/\sigma_\rho = 0.156 \pm 0.011$ (stat.) $^{+0.023}_{-0.010}$ (syst.) $^{+0.014}_{-0.013}$ (model.) measured by the ZEUS experiment at an average t similar to that of the present analysis [62]. This is slightly below the SU(4) prediction given in equation 3.31. The contribution to the final event sample coming from diffractive production of ω and ϕ mesons is 0.49 % and 0.21 % respectively.

5.3.2 Diffractive ρ' Production

The diffractive photoproduction of ρ' mesons contributes to the background through the two-stage decay process

$$\rho' \to \rho^{\pm}\pi^{\mp}\pi^0 \tag{5.17}$$

with the subsequent decay of the $\rho^{\pm}$ via

$$\rho^{\pm} \to \pi^{\pm}\pi^0 \tag{5.18}$$

if, as in the case of the ω and ϕ mesons, the decay photons from both the π^0 mesons escape detection.

Background due to ρ' mesons is once again simulated using the DIFFVM Monte Carlo generator. The ratio of the production cross sections for the ρ' and the ρ is known to evolve strongly with Q^2. At low Q^2, including photoproduction, several fixed target experiments have measured the ρ' cross section in the channel $\rho' \to \pi^+\pi^-\pi^+\pi^-$. From the compilation of results presented in [125], the ratio $\sigma(\rho' \to \pi^+\pi^-\pi^+\pi^-)/\sigma(\rho \to \pi^+\pi^-)$ can be estimated to be 0.1 ± 0.05. Under the naïve assumption that the branching ratios satisfy the relation

$$\frac{\sigma(\rho' \to \rho^+\pi^-\pi^0) + \sigma(\rho' \to \rho^-\pi^+\pi^0)}{\sigma(\rho' \to \pi^+\pi^-\pi^+\pi^-)} = 2, \tag{5.19}$$

the ratio $\sigma(\rho' \to \pi^+\pi^-\pi^0\pi^0)/\sigma(\rho \to \pi^+\pi^-)$ can then be predicted to be 0.2 ± 0.1. The diffractive production of ρ' mesons provides the largest background, forming a contribution to the final event sample of 1.24 %.

5.4 Control Distributions

This section presents the comparison between the data sample selected using the cuts listed in table 5.2 and the DIFFVM MC simulation. The MC includes the backgrounds described in section 5.3 and is normalised to the number of events observed

in the data. The simulation is corrected for the effects discussed in section 5.2 and the trigger efficiency reweights described in section 6.3.

Figure 5.8 presents the description of the kinematic variables t and W and the decay angles, θ^* and ϕ^*. The shape of the W distribution is due to the effect of the ET44 acceptance, which is reasonably described by the MC. In order to describe the observed high $|t|$ data, the t dependency is reweighted to a power law $|t|^{-n}$ with the value of n measured in section 7.1. The distributions of the decay angles are reweighted according to equation 4.22 using the spin density matrix elements measured in the present analysis (see section 7.2). Since the matrix elements are independent of t within errors, an average value is taken. In both cases, the reweights are applied iteratively. The shape of the ϕ^* distribution is due to the low acceptance for one of the pions when the ρ meson production and decay planes coincide ($\phi^* \approx 0, 180, 360^\circ$), see section 6.1.2.

Figure 5.9 shows the description of the tracks in terms of the longitudinal, p_z, and transverse, p_t, momentum and the angles θ and ϕ. All distributions are reasonably well described, showing a good understanding of the two pion candidates. Finally, the invariant mass of the two pion candidates is presented in figure 5.10. The simulated mass distribution for the ρ meson has been reweighted, as described in section 6.4, to take into account the relativistic nature of the resonance and its distortion due to interference arising from open pion pair production. A reasonable description is obtained, including the position of the peak, although the MC somewhat underestimates the data at high mass values.

Overall, a reasonable description of the data is observed, indicating that the MC simulation can be reliably used to correct the data for the acceptance and smearing effects associated with the H1 detector.

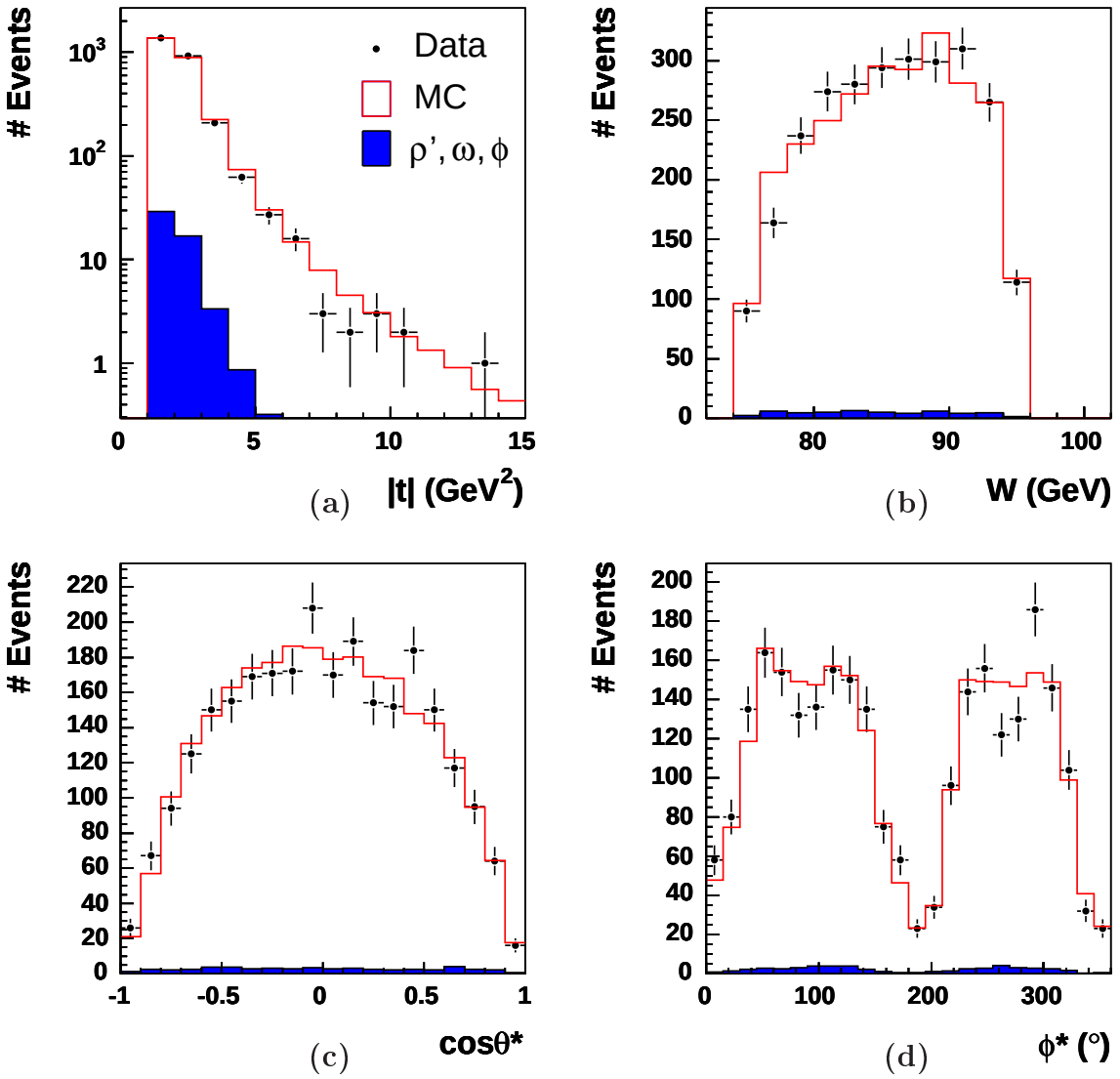

Figure 5.8: *The (a) $|t|$, (b) W, (c) $\cos\theta^*$ and (d) ϕ^* distributions. The data (points) are compared to the sum of the MC contributions (open histogram) for the ρ signal and the remaining ω, ϕ and ρ' background contribution (shaded histogram). The error bars show the statistical uncertainty on the data.*

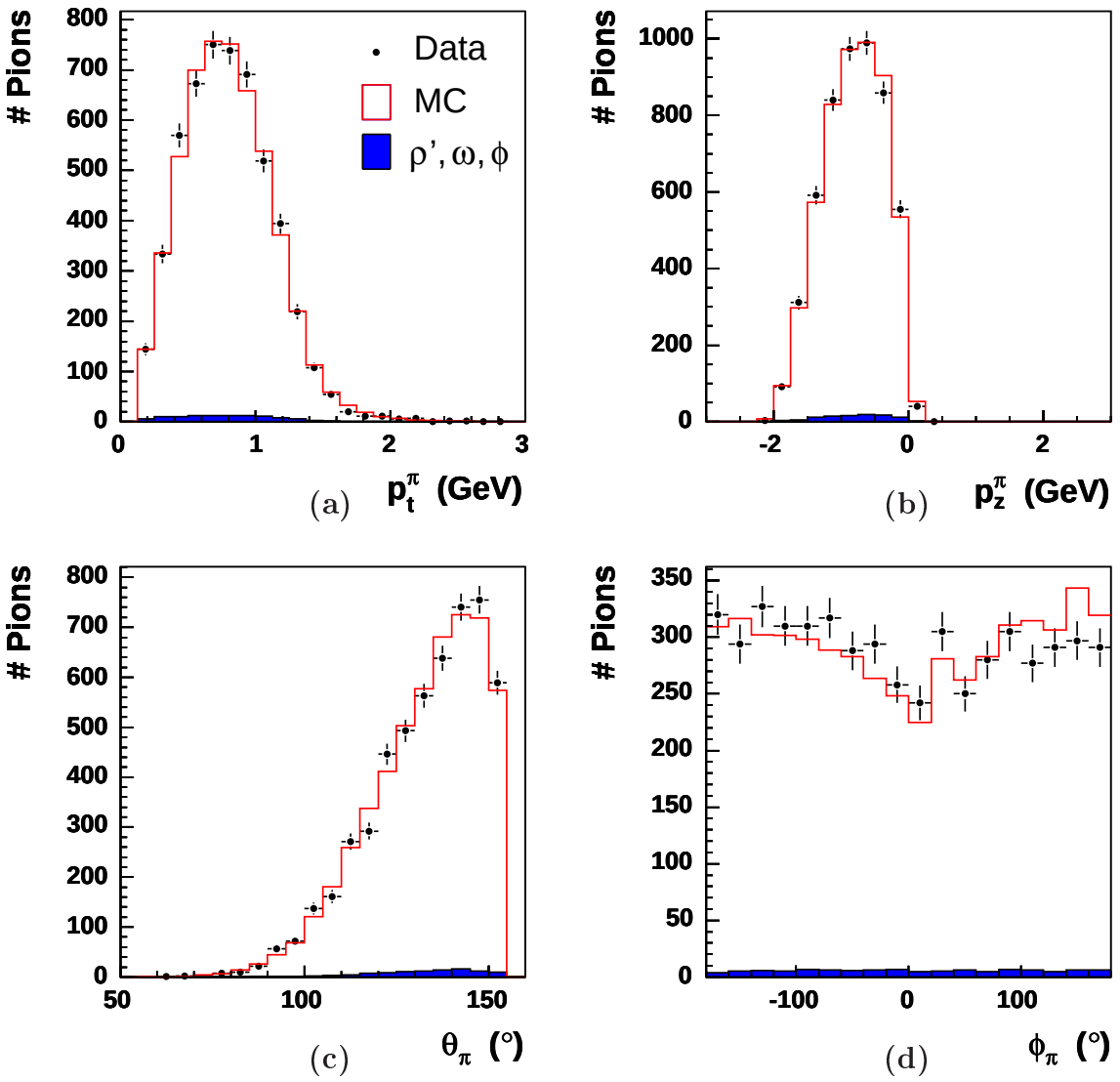

Figure 5.9: *Distributions of the (a) transverse and (b) longitudinal momentum and the (c) polar and (d) azimuthal angles for the two pion candidates. The data (points) are compared to the sum of the MC contributions (open histogram) for the ρ signal and the remaining ω, ϕ and ρ' background contribution (shaded histogram). The error bars show the statistical uncertainty on the data.*

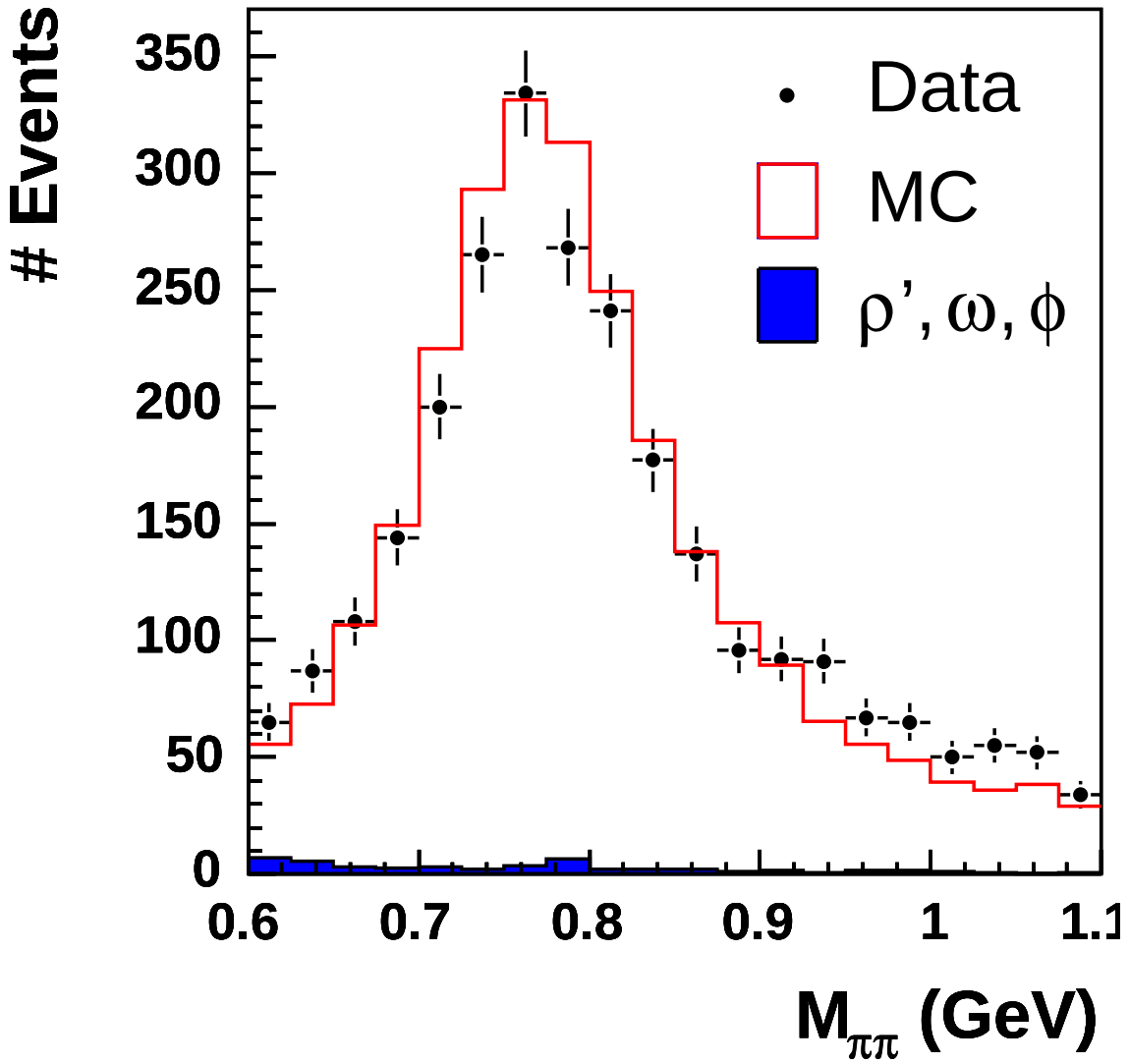

Figure 5.10: *The $\pi^+\pi^-$ invariant mass distribution. The data (points) are compared to the sum of the MC contributions (open histogram) for the ρ signal and the remaining ω, ϕ and ρ' background contribution (shaded histogram). The error bars show the statistical uncertainty on the data.*

Chapter 6

Cross Section Extraction

This chapter describes the prescription used to measure the differential cross sections presented in chapter 7. The differential ep cross section for each bin i, σ_i, in a distribution is defined as

$$\sigma_i = \frac{N^i_{data} - N^i_{bkg}}{A_i \epsilon_i \Delta_i \mathcal{L}} C_{mass} C_{skewing} \tag{6.1}$$

where N^i_{data} is the number of data events reconstructed in bin i and N^i_{bkg} is the MC estimate of the number of background events in the bin. A_i and ϵ_i are, respectively, the acceptance, including the effect of smearing, and trigger efficiency of the bin, as estimated from the MC simulation. Δ_i is the volume of the bin, which reduces to the width in the case of a one dimensional cross section, and $\mathcal{L}$ is the integrated luminosity of the measurement. By convention, cross sections pertaining to the ρ meson are defined for the invariant mass interval $2m_\pi < M_{\pi\pi} < m_\rho + 5\Gamma_\rho$ [81,94], where m_ρ and Γ_ρ are the nominal mass and decay width of the ρ meson, respectively. In order to extrapolate from the measured mass window ($0.6 < M_{\pi\pi} < 1.1$ GeV) one can define a correction factor C_{mass}, which is determined via the ratio of the ρ mass distribution (see equation 6.9) integrated over the appropriate invariant mass ranges. The factor $C_{skewing}$ further corrects the cross section for the contamination of the ρ signal due to open pion pair production and is described in section 6.4.

In this analysis the shape of the cross sections, and not their absolute normalisations, are of primary interest. Consequently, each cross section is normalised to unity in the relevant kinematic range. This has the advantage that the correlated systematic errors, which affect only the normalisation and not the shape, can be neglected. In this case, the extrapolation factor C_{mass}, included above for completeness, is no longer necessary.

The following sections detail the measurements of the acceptance, migrations, and trigger efficiency necessary to determine the cross section. The invariant mass distribution is then studied and the correction factor $C_{skewing}$ determined. Finally, the sources of uncertainty on the measurement are considered.

6.1 Resolution, Acceptance and Migrations

Any real detector will have a limited geometric acceptance, finite measurement resolution and will never be 100% efficient. The resulting inaccuracies in the measured quantities can cause events to enter or leave the selected sample and allow migrations between the various bins that make up the cross section. Provided it describes the data with sufficient accuracy, the Monte Carlo simulation can be used to estimate these effects and hence extract, from the number of observed events, the true cross section. The size of these corrections is minimised by choosing the binning scheme such that the bins contain sufficient statistics and have a width larger than the resolution, reducing the number of migrations.

6.1.1 Resolution

The resolution is measured by comparing the reconstructed level quantity, after detector simulation, to that generated. For a variable x, the absolute resolution σ_x

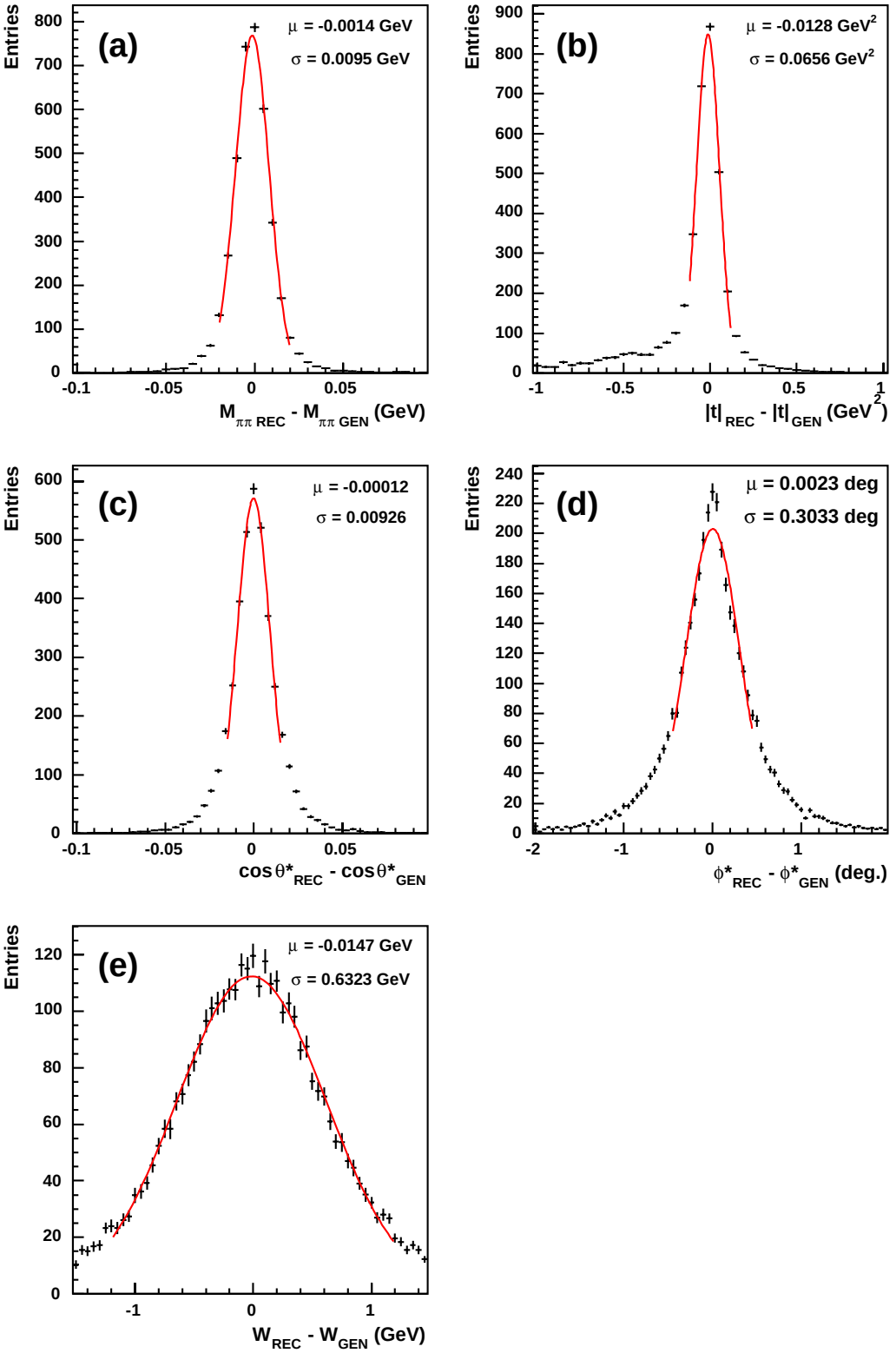

Figure 6.1: *Absolute resolutions for (a) $M_{\pi\pi}$, (b) $|t|$, (c) $\cos\theta^*$, (d) ϕ^* and (e) W. The points show the MC results and the line indicates the result of a Gaussian fit.*

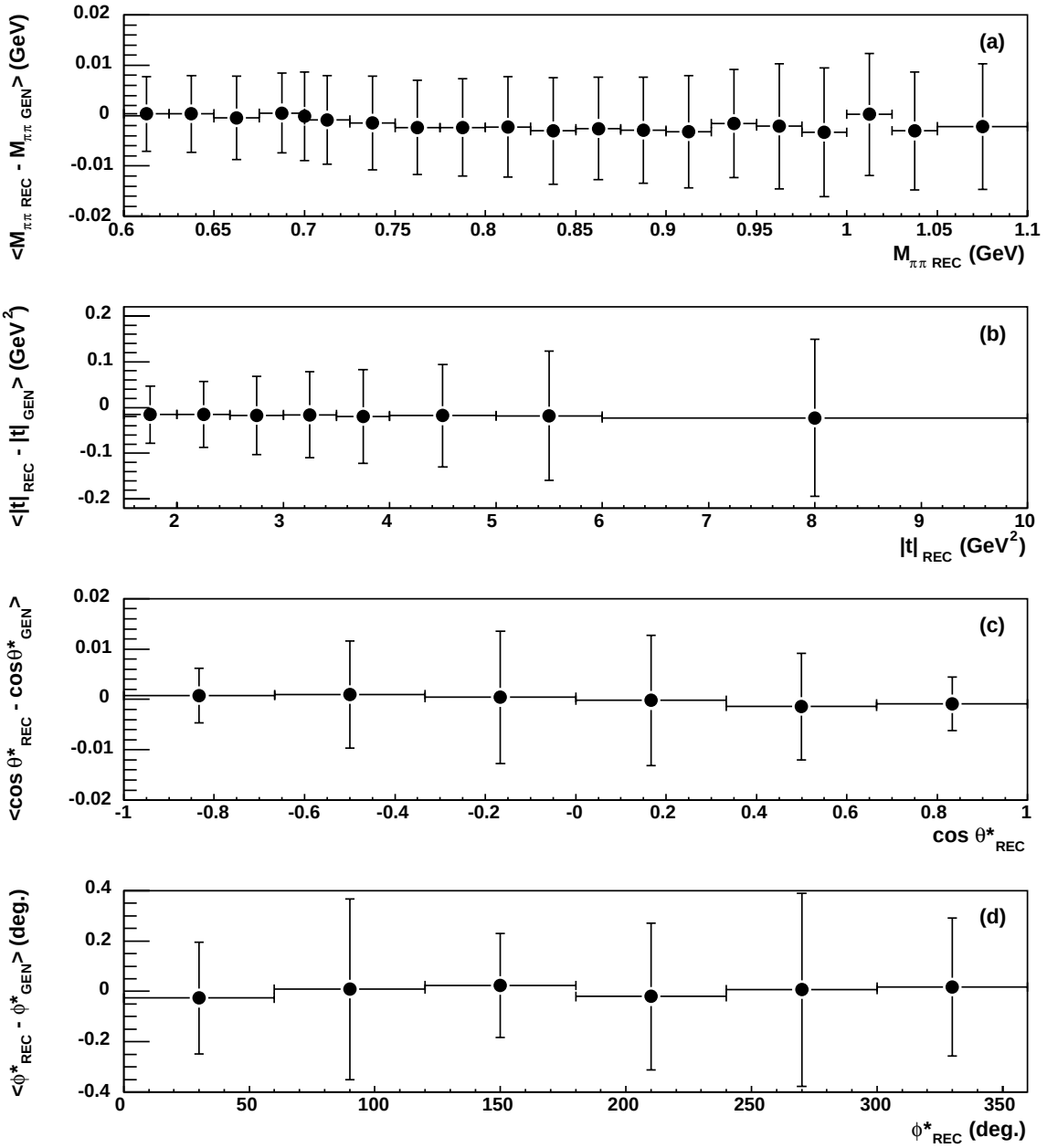

Figure 6.2: *The mean value of a Gaussian fit to the absolute resolutions for (a) $M_{\pi\pi}$, (b) $|t|$, (c) $\cos\theta^*$ and (d) ϕ^* as a function of the corresponding variable. The vertical error bars represent the resolutions and the horizontal ones show the chosen bin widths. It should be noted that the horizontal and vertical axes are plotted on different scales*

is calculated by

$$\sigma_x = x_{GEN} - x_{REC} \tag{6.2}$$

where x_{GEN} and x_{REC} are the generated and reconstructed values respectively.

The resolutions in $M_{\pi\pi}$, $|t|$, $\cos\theta^*$, ϕ^* and W are shown in figure 6.1. Figure 6.2 plots the mean of a Gaussian fit to the resolution for the bins of the appropriate variable used in this analysis. The vertical error bars represent the resolutions and the horizontal error bars represent the width of the bins. In all cases, the resolution is better than the chosen width of the bins.

6.1.2 Acceptance

The acceptance, A, compares the number of reconstructed events to the number of generated events on a bin-by-bin basis. For a bin i, the acceptance is defined as

$$A_i = \frac{N^i_{REC}}{N^i_{GEN}} \tag{6.3}$$

where N^i_{GEN} and N^i_{REC} are the number of events generated and reconstructed in the bin i respectively. The overall acceptance, used in the calculation of the cross section, is the product of the ET44 acceptance and that of the main detector. Only the latter is described here since the ET44 acceptance has already been discussed in section 5.1.3.

Figure 6.3 shows the acceptances as a function of $M_{\pi\pi}$ and t. For the invariant mass, the acceptance is relatively flat with an average value of around 40%. The acceptance in t is also relatively flat at high $|t|$, with a value of around 45%, but falls off sharply to just above 30% at low $|t|$. This decrease is due not only to the minimum p_t requirement on the tracks, but also to the upper limit on the polar angle, since low p_t tracks form a smaller angle to the beampipe.

The acceptances for the decay angles are shown in figure 6.4 for the different t bins used in this analysis. For ease of visualisation, only the one-dimensional projections

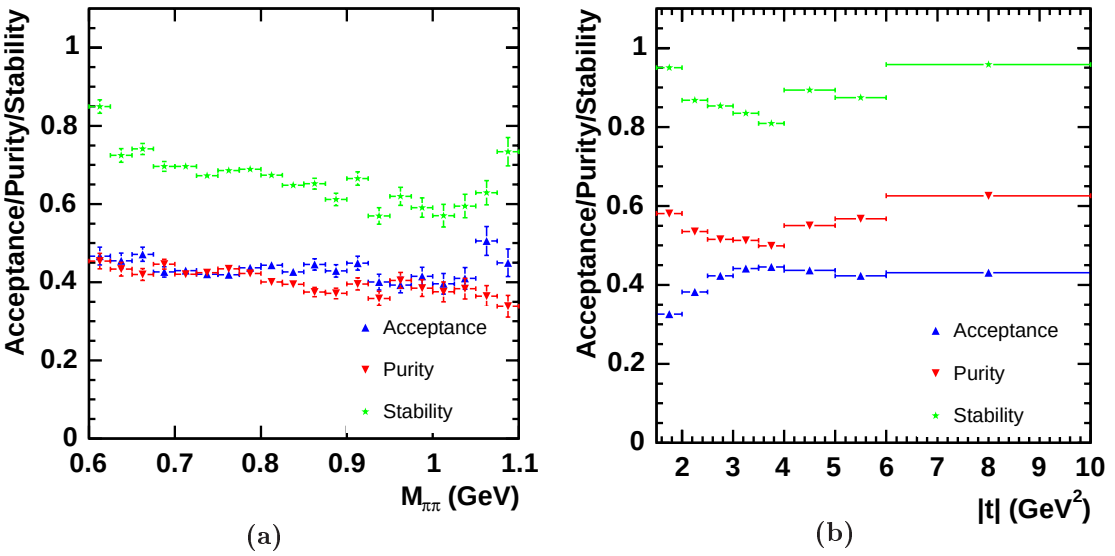

Figure 6.3: *The acceptance, purity and stability for (a) $M_{\pi\pi}$ and (b) $|t|$.*

in $\cos\theta^*$ and ϕ^* are shown, rather than the full two-dimensional distribution. In the lowest $|t|$ range, the acceptance in $\cos\theta^*$ is relatively flat with an average value of approximately 30%. As $|t|$ increases, the acceptance rises to around 45% and begins to develop a convex shape, which increases gently from $|\cos\theta^*| = 1$ to a maximum at $\cos\theta^* \approx 0$. Remembering that θ^* is defined in the ρ rest frame, in order to understand this effect one must consider what happens when the two pions are boosted to the laboratory frame. In the former case, one pion is emitted parallel to the ρ direction and the other anti-parallel. Consequently, the effect of any boost in the ρ direction is to increase the momentum of one pion while simultaneously decreasing the momentum of the other. This asymmetric momentum configuration increases the probability of the lower momentum track failing the p_t cuts described in section 5.1.4, resulting in a lower acceptance. In the latter case, however, the pions are emitted in the direction perpendicular to the ρ line of flight. This time, the boost will affect both pions equally and so no reduction in acceptance is observed. As a function of ϕ^*, the acceptance shows a distinctive double peak structure with maxima at $\phi^* \approx 90$ and 270° and minima at $\phi^* \approx 0, 180$ and 360°. This is due to

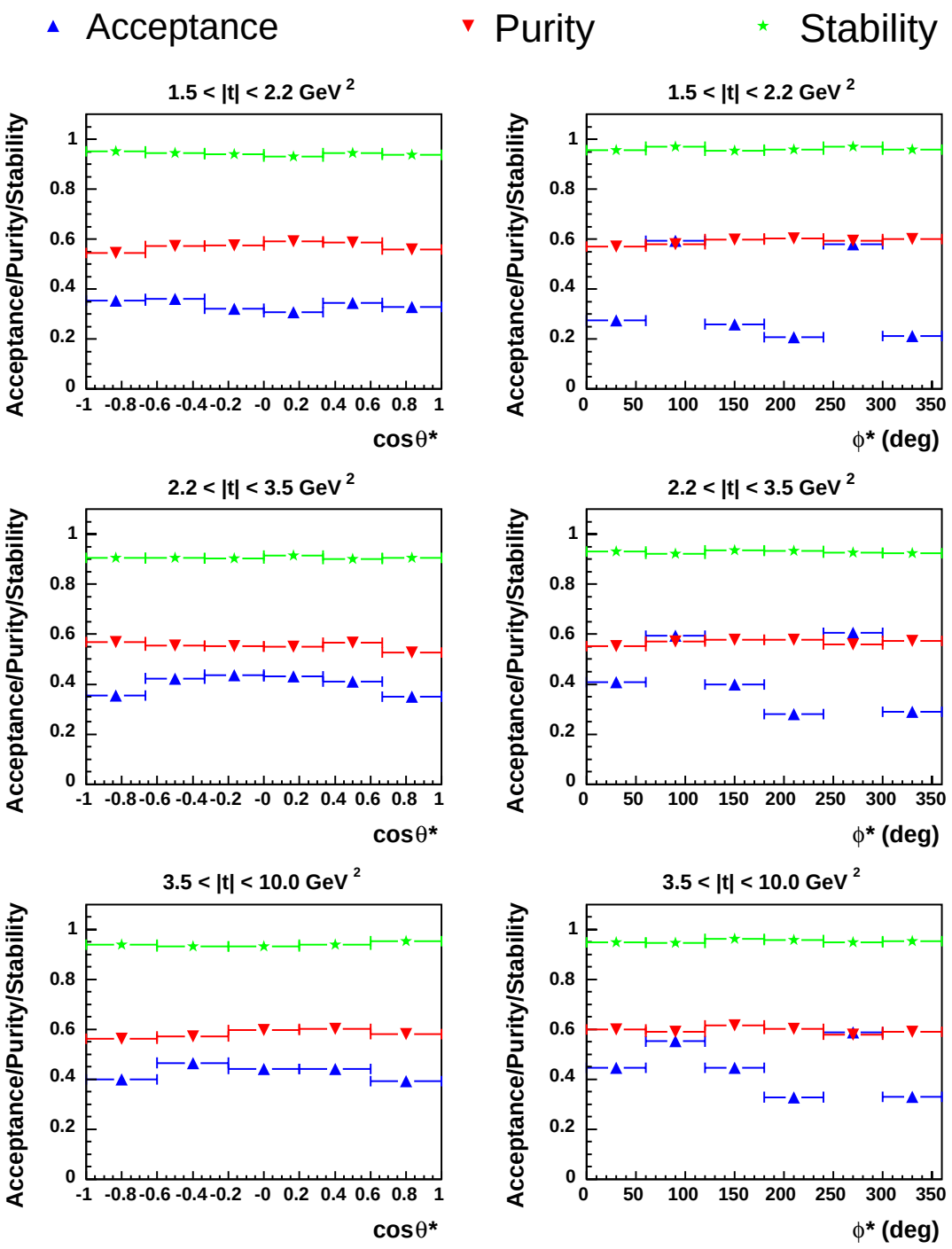

Figure 6.4: *The acceptance, purity and stability for* $\cos\theta^*$ *(left) and* ϕ^* *(right) in bins of* $|t|$.

the requirement that the polar angle of both pions be less than 155° and can be understood by considering figure 4.8. In the former case, the meson decay plane is perpendicular to its production plane, resulting in both pions being emitted at the same polar angle as the ρ meson. Hence, providing the ρ meson satisfies the upper limit on the polar angle, the two pions will also do so. In the latter case, however, the meson production and decay planes coincide, resulting in one pion being emitted with a polar angle less than the ρ meson and the other with a polar angle greater than the ρ meson. The pion with the larger polar angle may fail the upper cut on the polar angle even if the ρ meson passes it, leading to the event being rejected and consequently reducing the acceptance.

6.1.3 Purity

Migrations into a bin are studied using the purity, P, which looks at the number of events reconstructed in a particular bin that were also generated in that bin. The purity for a bin i is given by

$$P_i = \frac{N^i_{GEN+REC}}{N^i_{REC}} \tag{6.4}$$

where $N^i_{GEN+REC}$ is the number of events which where both generated and reconstructed in that bin.

The purities as a function of $M_{\pi\pi}$ and t are shown in figure 6.3. The purity for the invariant mass distribution is reasonably flat with an average value of around 40%. In the case of the t distribution, the purity is greatest in the lowest and highest $|t|$ bins with a dip inbetween, reflecting the relative size of the resolution compared to the bin width. In general, the purity in t ranges between 50% and 60%. Figure 6.4 shows the one dimensional purities for the decay angles $\cos\theta^*$ and ϕ^* in bins of t. In both cases, the purity is flat at around 55%.

6.1.4 Stability

The stability, S, considers the migrations out of a bin and is complementary to the purity. Specifically, it quantifies the number of events generated in a bin which, given they were not lost from the sample, were also reconstructed in that bin. In other words, the stability for a bin i is defined as

$$S_i = \frac{N^i_{GEN+REC}}{N^i_{GEN+REC'}} \tag{6.5}$$

where $N^i_{GEN+REC'}$ is the number of events generated in a bin i that were reconstructed somewhere in the final event sample.

The stabilities as a function of $M_{\pi\pi}$ and t are shown in figure 6.3. The stability decreases slowly with increasing invariant mass, tending to approximately 60% at the highest $M_{\pi\pi}$. For the t distribution, the stability is a similar shape to the purity, but with a higher absolute value in the range $80 - 95\%$. Figure 6.4 shows the one dimensional stabilities for the decay angles $\cos\theta^*$ and ϕ^* in bins of t. The stability is flat in both cases with an average value above 90%.

6.2 Bin Centre Corrections

The cross section measured in a particular bin does not correspond to that at the centre of the bin but rather at the average value of the variable within that bin. For a rapidly changing distribution, such as the t cross section measured here, these two points are sufficiently displaced that it is necessary to correct for this difference. One way to do this is to shift the measured point to the true centre of gravity for each bin. For a bin in t which spans the range $|t_1|$ to $|t_2|$, this centre of gravity, $|t_0|$, can be determined using

$$\frac{d\sigma}{dt}(|t_0|) = \frac{1}{|t_1| - |t_2|} \int_{|t_1|}^{|t_2|} \frac{d\sigma}{dt}(|t|)\, dt \tag{6.6}$$

where the t distribution is assumed to follow a power law $d\sigma/dt \sim |t|^{-n}$. The correction is performed recursively with the value of n being obtained from a fit to the data using the corrected bin centres at each iteration.

6.3 Trigger Efficiency

In order to measure a cross section, any inefficiencies in the triggers used to collect the data must be understood and corrected for. The efficiency can be measured either from the data or the MC simulation. In the case of the data, the trigger efficiency can be calculated using an unbiased data sample collected by an independent trigger, known as a monitor trigger, which has no trigger elements in common with the trigger of interest. Unfortunately, no such monitor trigger exists in the photoproduction regime relevant for this analysis and, consequently, the trigger efficiency must be measured from the MC simulation. The MC description of the trigger efficiencies can, however, be cross-checked in the electroproduction regime.

The efficiency of the electron tagger trigger element (etag_44) may be excluded since it is well known and already accounted for in the correction of the electron tagger acceptance. The MC description of the remaining trigger element efficiencies is cross-checked, and where necessary tuned, using a sample of high Q^2 electroproduction ρ events. In this kinematic regime, the events are triggered on the basis of the scattered electron detected in the SpaCal using the s0 subtrigger. Since this trigger is purely based on the SPCLe_IET > 2 trigger element, which requires an energy deposit of at least 6 GeV in the outer region of the SpaCal, it is independent of the trigger elements forming the s109 subtrigger used in this analysis.

The event selection used is based on the H1 preliminary measurement of the elastic electroproduction of ρ mesons at high Q^2, for which details can be found in [121], and is summarised in table 6.1. This is similar to the event selection

Electron candidate	$E_e > 17$ GeV $153 < \theta_e < 176.5°$ $Q^2_{DA} > 5$ GeV^2 $40 < W_{DA} < 160$ GeV SpaCal Fiducial Cut: a) $-16 < x < 9$ cm b) $-9 < y < 16$ cm
Pion candidates	$N_{tracks} = 2$ Opposite Charge Both from primary vertex $\|z_{vtx}\| < 35$ cm $20° < \theta_\pi < 155°$ $p_t^\pi > 150$ MeV $p_t^{lead\ \pi} > 450$ MeV $\|t_{DA}\| < 5$ GeV
LAr and SpaCal calorimeter	E(Neutral LAr cluster) < 400 MeV E(Non-e SpaCal cluster) < 300 MeV
Invariant mass	$0.6 < M_{\pi\pi} < 1.1$ GeV $M_{KK} > 1.04$ GeV
Event	$\sum(E - p_z) > 52$ GeV

Table 6.1: *An overview of the selection of ρ electroproduction events used to calculate the trigger efficiencies.*

described in chapter 5, with the exception of the scattered electron. Here, an electron with an energy $E_e > 17$ GeV is required in the angular range $153 < \theta_e < 176.5°$, corresponding to the SpaCal. Events where the centre of gravity of the electron energy deposit lies in the inner region $-16 < x < 9$ cm and $-9 < y < 16$ cm, which is not covered by the s0 trigger, are rejected. Additional fiducial cuts are made to remove inefficient cells and hence ensure the s0 trigger is 100% efficient. To veto additional particles in the SpaCal, the energy of the most energetic cluster not associated to the scattered electron must be less than 0.3 GeV. The detection of the scattered electron allows the reconstruction of the total $E - p_z$ of the final state. Since this is a conserved quantity, a well reconstructed physics event must have an $E - p_z$ comparable to that of the incident particles, $\sum(E - p_z) \approx 55.2$ GeV. Consequently, the selected events are required to have $\sum(E - p_z) > 52$ GeV. The resulting kinematic regime is $Q^2_{DA} > 5$ GeV^{2}and $40 < W_{DA} < 160$ GeV. All the kinematic quantities are reconstructed using the double angle method (DA) [126], which uses the polar angles of the scattered electron and the ρ meson.

The selected events are compared to the results of the DIFFVM MC simulation, which includes both proton elastic and proton dissociative components as well as the contribution from ρ', ω and ϕ mesons, in figure 6.5. The purpose of this comparison is to check that a clean event sample has been selected and is reasonably described by the MC simulation, in particular the pion tracks since these are the main factors affecting the DCRPh_Ta and zVtx_Cls trigger elements. This study is not intended to describe the intricacies of the ρ electroproduction analysis. With this in mind, the overall agreement between the data and the MC is considered sufficient.

The efficiency, ϵ_t, of a particular trigger element, t, is calculated from the independent data sample by

$$\epsilon_t = \frac{N_{m\&\&t}}{N_m} \tag{6.7}$$

where N_m is the number of events, which pass the cuts listed in table 6.1, saved by the s0 monitor trigger and $N_{m\&\&t}$ is the number of those events which subsequently

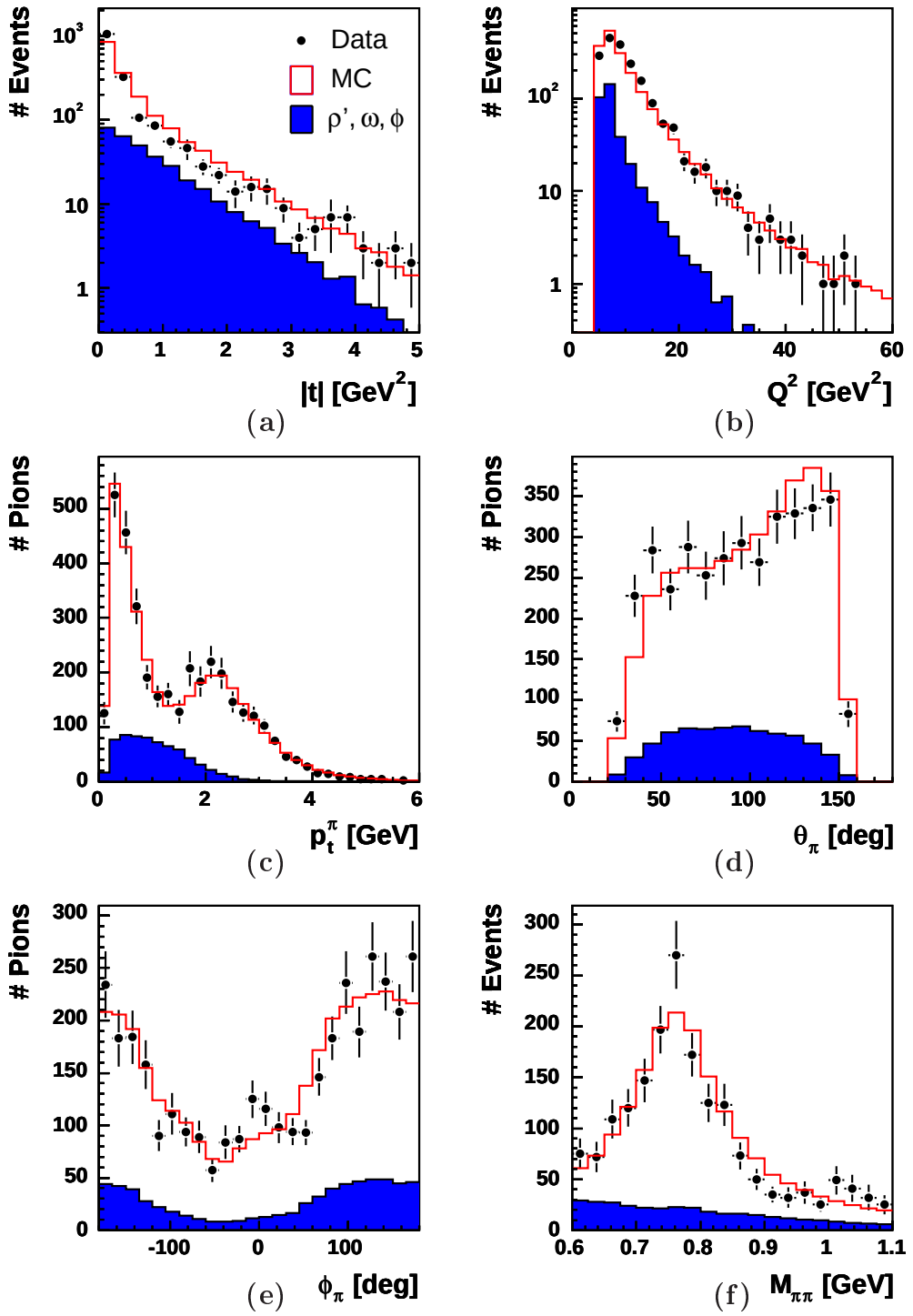

Figure 6.5: *The distributions in (a) $|t|$ and (b) Q^2 along with the (c) transverse momentum, (d) polar angle and (e) azimuthal angle of the two pion tracks and (f) the two-pion invariant mass. The data (points) are compared to the sum of the MC contributions (open histogram) for the ρ signal and the remaining ω, ϕ and ρ' background contribution (shaded histogram).*

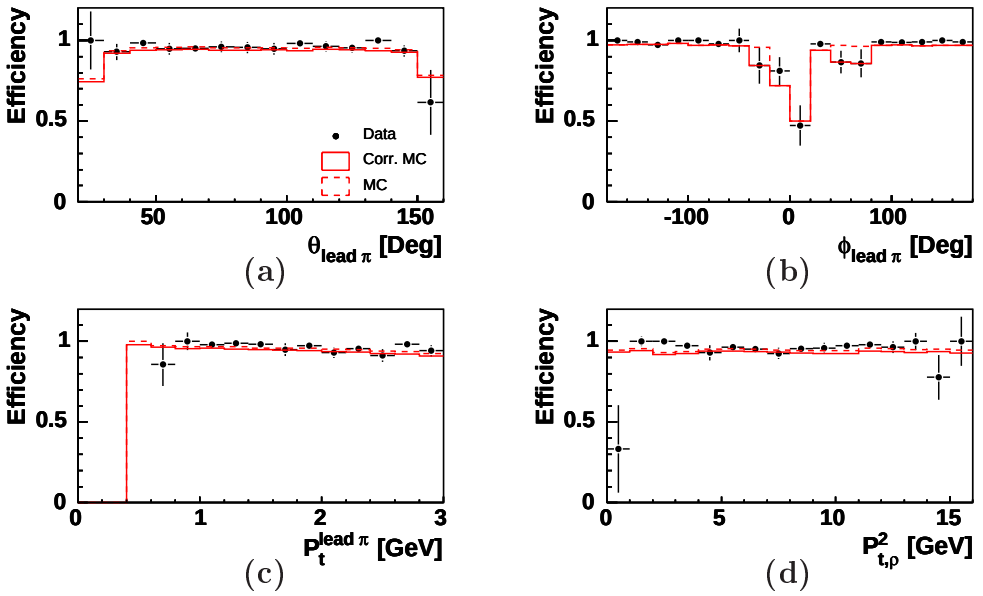

Figure 6.6: *The efficiency of the* DCRPh_Ta *trigger element as a function of (a) the polar angle, (b) azimuthal angle and (c) the transverse momentum of the lead pion and (d) the transverse momentum squared of the ρ meson. The data (points) are compared to the uncorrected MC (dashed line) and the corrected MC (solid line).*

also pass the trigger element t. In the MC sample, unlike the data sample, the number of selected events before any trigger requirement, N, is accessible. Hence, the efficiency of the trigger element t can be calculated directly via

$$\epsilon_t = \frac{N_t}{N} \tag{6.8}$$

where N_t is the number of selected events that pass the trigger element t. The simulated efficiency for each trigger element is then compared to that observed in the data and corrected where necessary.

Figure 6.6 shows the efficiency of the DCRPh_Ta trigger element as a function of the polar angle, azimuthal angle and transverse momentum of the leading pion track, which fires the DCRPh_Ta element, plus the p_t^2 of the ρ meson. The error bars show binomial errors with the errors for bins having 100% efficiency estimated on the basis of one less event in that bin. Overall, the efficiency is approximately 95%.

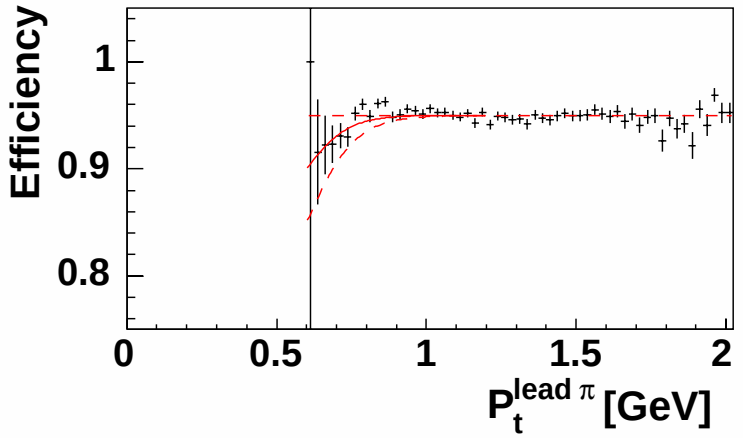

Figure 6.7: *The systematic variations of the* DCRPh_Ta *efficiency in the* $P_t^{lead\ \pi}$ *threshold region. The points show the results of the* γp *MC after the application of all the selection criteria described in section 5.1.7 and the solid line indicates a parameterisation of this based on a Fermi function. The dashed lines indicate the effect of the systematic variations to a flat dependence or a steeper Fermi function.*

The original MC, shown by the dashed line, provides a good overall description of the efficiency, including the significant drop in efficiency at $\phi \approx 0°$, which is due to a dead region in the CJC2. There are, however, a small number of bins in ϕ, in particular the region $40 < \phi < 80°$, where the MC overestimates the efficiency. The efficiency in these bins is corrected to the data and the resulting corrected MC is shown by the solid line. As part of the systematic error treatment (see section 6.5), the correction factors applied are either removed or doubled in order to account for the uncertainty on the data efficiency.

A further systematic error must be assigned to cover the uncertainty in the Monte Carlo modelling of the rise of the DCRPh_Ta efficiency with $P_t^{lead\ \pi}$ near the threshold region. However, this cannot be studied with the s0 sample as this low P_t data is not triggered since the s0 subtrigger does not cover the inner region of the SpaCal. Consequently, this rise is investigated using the photoproduction MC following its correction for the reweights described above. The resulting efficiency, after the application of the full selection procedure outlined in section 5.1.7, is shown

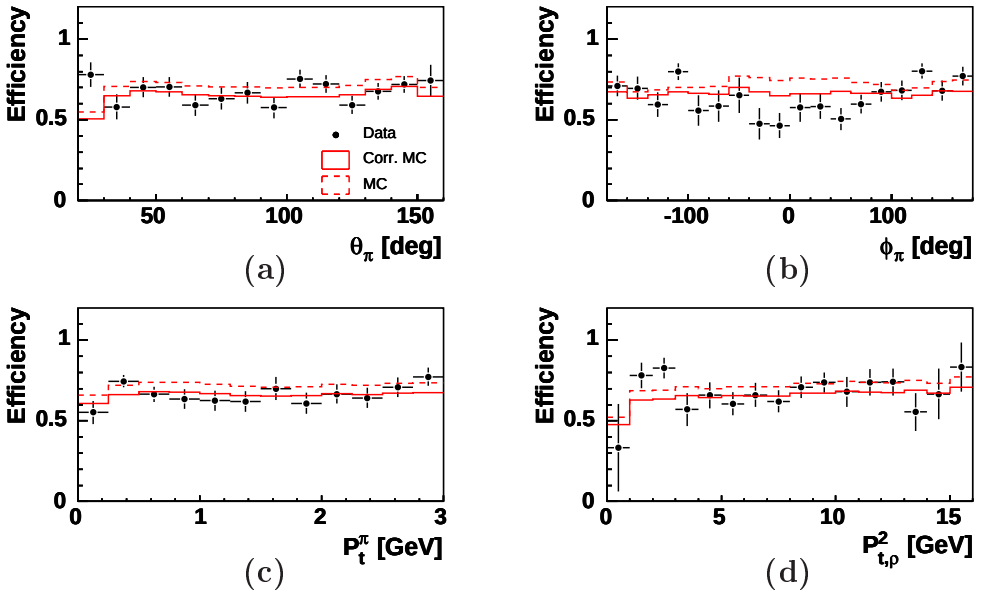

Figure 6.8: *The efficiency of the* zVtx_Cls *trigger element as a function of (a) the polar angle, (b) azimuthal angle and (c) the transverse momentum of the pion tracks and (d) the transverse momentum squared of the ρ meson. The data (points) are compared to the uncorrected MC (dashed line) and the corrected MC (solid line).*

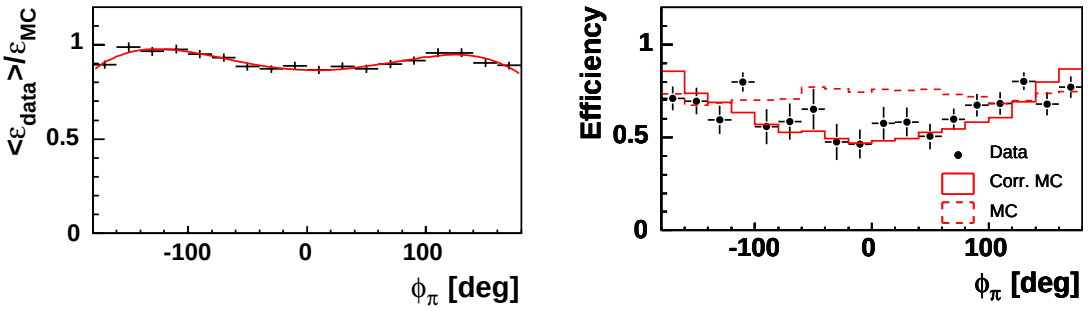

Figure 6.9: *(a) The ratio of the average data efficiency to the MC efficiency for* zVtx_Cls *as a function of ϕ_π (points) fitted with a polynomial of order four (line). (b) The systematic variations of the* zVtx_Cls *MC efficiency as a function of ϕ_π: uncorrected (dashed line) and reweighted to a quadratic in ϕ_π (full line).*

in figure 6.7. This rise in efficiency can be described by a Fermi function [127], the result of which is shown by the solid line. As a systematic error, the efficiency is alternatively reweighted to a flat dependency or a steeper Fermi function, indicated by the dotted lines in figure 6.7, which corresponds to a variation of roughly 5% at the lowest observed P_t values.

Figure 6.8 shows the efficiency of the zVtx_Cls trigger element as a function of the polar angle, azimuthal angle and transverse momentum of both pion tracks plus the p_t^2 of the ρ meson. It can be seen that the uncorrected MC provides a rather poor description of the efficiency, in particular, the ϕ dependence. A correction function is derived by taking the ratio of the average data efficiency, which is 67%, to the bin-by-bin efficiency in the MC as a function of ϕ and fitting it with a polynomial of degree four (see figure 6.9(a)). This function is used to calculate the correction factor for each of the two tracks, which are then averaged and applied to the MC event. This results in an approximately flat ϕ dependence as shown by the solid line in figure 6.8(b). The systematic uncertainty is estimated by alternatively reweighting the MC trigger efficiency to a quadratic in ϕ, as shown in figure 6.9(b), or removing the reweight entirely. The quadratic reweight was chosen as a systematic because it was observed to give a degraded description of the photoproduction sample.

As expected, the efficiency of the !LAr_IF trigger element is 100% due to the veto on additional activity in the LAr calorimeter.

6.4 The Invariant Mass Distribution $M_{\pi\pi}$ and Skewing

As mentioned in section 5.2, the DIFFVM MC generates the ρ meson mass peak according to a simple non-relativistic Breit-Wigner distribution. In reality there is a contamination of the ρ signal resulting from non-resonant $\pi^+\pi^-$ pair production,

which gives rise to an effect known as skewing. Consequently, the MC must be reweighted in order to describe the data and this contamination corrected for in the final cross section. This section details the various parameterisations of the $\pi^+\pi^-$ invariant mass distribution and investigates the effect of skewing for the current analysis.

6.4.1 Parameterisation of the Invariant Mass Distribution

The invariant mass of the two decay pions $M_{\pi\pi}$ is parameterised in terms of a relativistic Breit-Wigner distribution

$$BW_\rho(M_{\pi\pi}) = \frac{M_{\pi\pi} m_\rho \Gamma(M_{\pi\pi})}{(m_\rho^2 - M_{\pi\pi}^2)^2 + m_\rho^2 \Gamma^2(M_{\pi\pi})} \tag{6.9}$$

where m_ρ is the nominal ρ mass and $\Gamma(M_{\pi\pi})$ is the relativistic width of the resonance. The momentum dependent relativistic width can be expressed in terms of the non-relativistic width of the ρ meson, Γ_ρ, in several ways [128]:

$$\Gamma(M_{\pi\pi}) = \Gamma_\rho \left(\frac{q^*}{q_0^*}\right)^3 \frac{2}{1 + (q^*/q_0^*)^2} \tag{6.10}$$

$$\Gamma(M_{\pi\pi}) = \Gamma_\rho \left(\frac{q^*}{q_0^*}\right)^3 \frac{m_\rho}{M_{\pi\pi}} \tag{6.11}$$

$$\Gamma(M_{\pi\pi}) = \Gamma_\rho \left(\frac{q^*}{q_0^*}\right)^3 \tag{6.12}$$

where q^* is the momentum of the pions in the $\pi^+\pi^-$ centre of mass frame and q_0^* is this momentum under the assumption $M_{\pi\pi} = m_\rho$. In this analysis, the parameterisation given in equation 6.11 is chosen. The effect of varying this choice of parameterisation is taken into account for the determination of the skewing described below.

Previous measurements of the ρ meson have shown evidence for a distortion of the invariant mass distribution with respect to the simple Breit-Wigner description given in equation 6.9. The peak of the distribution is observed to be shifted to a

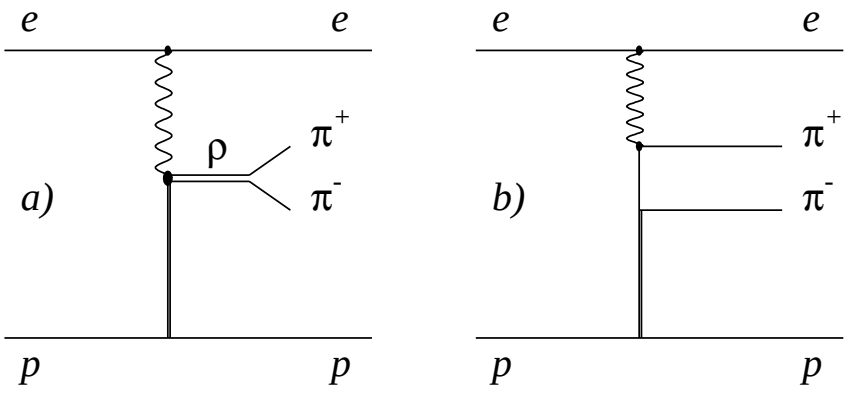

Figure 6.10: *Schematic diagrams illustrating (a) production of $\pi^+\pi^-$ via a ρ resonance and (b) non-resonant (open) $\pi^+\pi^-$ production.*

lower invariant mass and there is an enhancement (suppression) of the cross section below (above) the nominal ρ mass. This asymmetric nature of the ρ resonance is known as skewing and can be explained in terms of an interference between resonant (see figure 6.10(a)) and non-resonant (see figure 6.10(b)) $\pi^+\pi^-$ production. Two different parameterisations of this skewing effect have been suggested.

In the phenomenological prescription of Ross and Stodolsky [129], the relativistic Breit-Wigner is multiplied by a skewing factor $(m_\rho/M_{\pi\pi})$ such that

$$\frac{dN}{dM_{\pi\pi}} = f_\rho BW_\rho(M_{\pi\pi}) \left(\frac{m_\rho}{M_{\pi\pi}}\right)^{n_{RS}}, \tag{6.13}$$

where f_ρ is a normalisation constant and n_{RS} is the skewing parameter, which must be determined experimentally. In the Söding approach [130], the skewing is explained as an interference of the resonant $\rho \to \pi^+\pi^-$ amplitude with the p-wave Drell type $\pi\pi$ background. The resulting parameterisation,

$$\frac{dN}{dM_{\pi\pi}} = f_\rho BW_\rho(M_{\pi\pi}) + f_I I(M_{\pi\pi}) + f_{NR}, \tag{6.14}$$

consists of a resonant Breit-Wigner term, a non-resonant term, f_{NR}, plus an additional interference term, $I(M_{\pi\pi})$, given by

$$I(M_{\pi\pi}) = \frac{m_\rho^2 - M_{\pi\pi}^2}{(m_\rho^2 - M_{\pi\pi}^2)^2 + m_\rho^2\Gamma^2(M_{\pi\pi})} \tag{6.15}$$

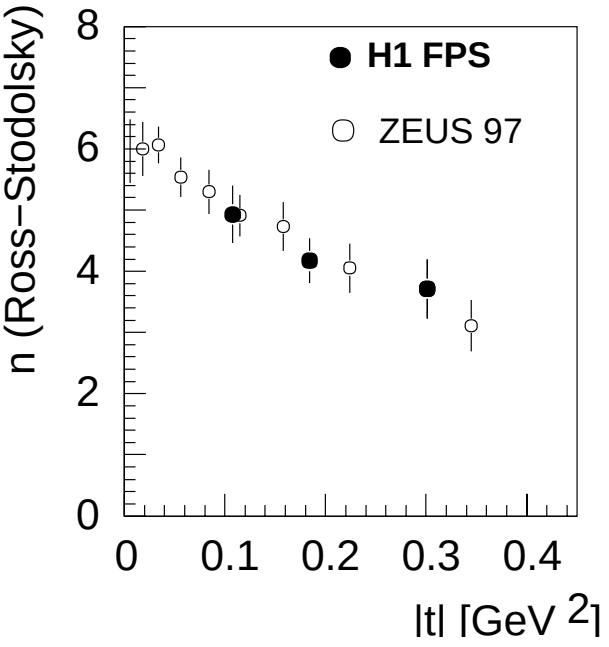

Figure 6.11: *Measurements of the Ross-Stodolsky skewing parameter, n_{RS}, as a function of $|t|$ in photoproduction at H1 [131] and ZEUS [98]. The error bars indicate the statistical and systematic errors added in quadrature.*

where f_I represents the relative normalisation of the interference term. Due to the phase uncertainty between the resonant and non-resonant terms, no constraint is imposed on the relative sizes of the two contributions.

Previous measurements of the Ross-Stodolsky skewing parameter in photoproduction [98, 131], see figure 6.11, show a decrease in n_{RS} with increasing $|t|$ for low values of $|t|$. At larger $|t|$, the ZEUS Collaboration observe that the contribution from skewing in the Söding parametrisation tends to zero above $|t| = 2.5$ GeV^2 [62]. It is therefore expected that the effect due to skewing in the present analysis will be small, particularly at the higher $|t|$ values.

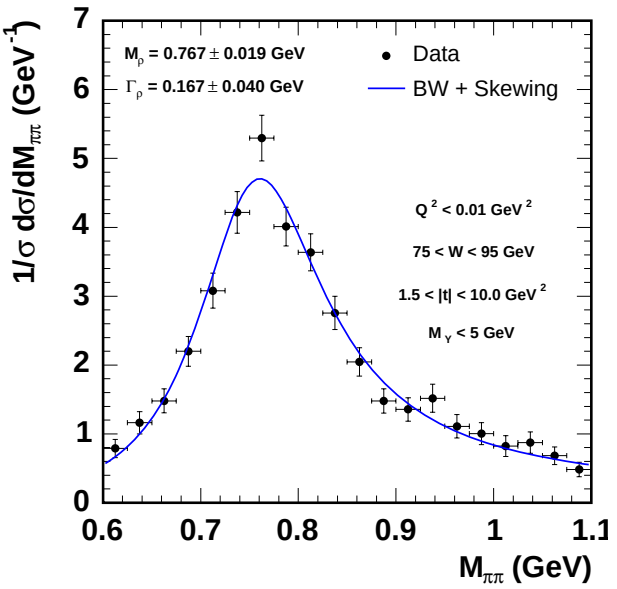

Figure 6.12: *The normalised differential cross section as a function of the two-pion invariant mass for the stated kinematic range. The curve shows the result of a fit using the Ross-Stodolsky parameterisation (equation 6.13). Only statistical errors are shown.*

6.4.2 The Effect of Skewing

The invariant mass distribution of the two decay pions is studied in the range $0.6 \leq M_{\pi\pi} \leq 1.1$ GeV and for the kinematic domain presented in section 5.1.8. Figure 6.12 shows the differential cross section $d\sigma/dM_{\pi\pi}$, after background subtraction and correction for the acceptance, migration and efficiency described above. The curve represents the result of a fit using the Ross-Stodolsky parameterisation presented in equation 6.13, with m_ρ, Γ_ρ, f_ρ and n_{RS} as free parameters. The extracted values of $m_\rho = 0.767 \pm 0.019$ GeV and $\Gamma_\rho = 0.167 \pm 0.040$ GeV are in agreement with those quoted by the Particle Data Group (PDG) [106] and the χ^2 per degree of freedom is $\chi^2/ndf = 15.73/16$. The overall skewing factor $n_{RS} = 0.06 \pm 1.49$ is compatible with zero, suggesting no significant non-resonant pion contribution. Repeating the fit using a pure Breit-Wigner distribution (equation 6.9) yields consistent results for m_ρ and Γ_ρ.

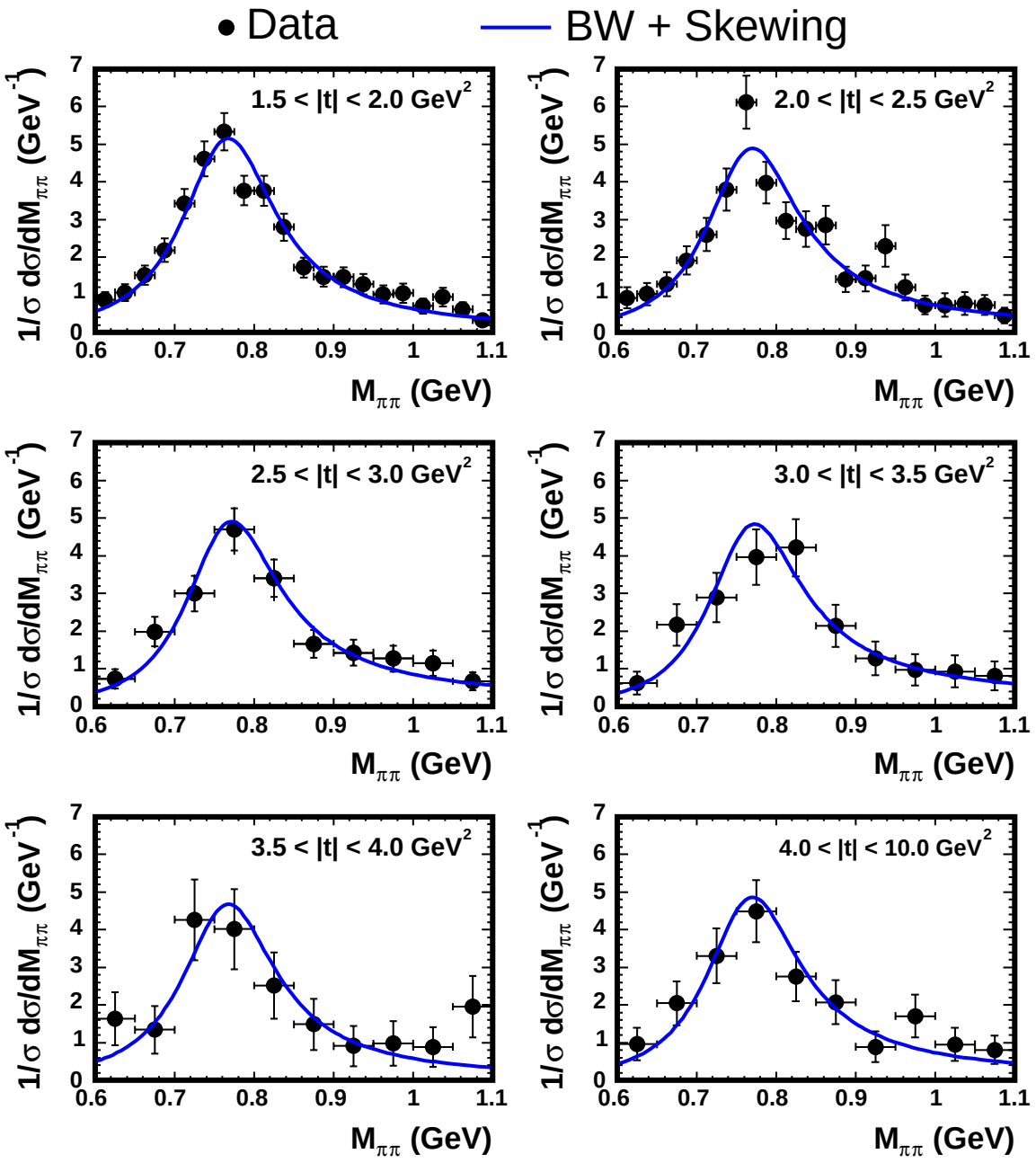

Figure 6.13: *The normalised differential cross section* $1/\sigma\ d\sigma/dM_{\pi\pi}$ *in different* t *intervals. The curves show the result of a fit using the Ross-Stodolsky parameterisation (equation 6.13). Only statistical errors are shown.*

$\|t\|$ range (GeV^2)	$\langle\|t\|\rangle$ (GeV^2)	n_{RS}
$1.5 - 2.0$	1.72	$0.93 \pm 0.33\ ^{+0.34}_{-0.07}$
$2.0 - 2.5$	2.22	$0.15 \pm 0.44\ ^{+0.32}_{-0.08}$
$2.5 - 3.0$	2.71	$-0.43 \pm 0.56\ ^{+0.30}_{-0.08}$
$3.0 - 3.5$	3.20	$-0.68 \pm 0.74\ ^{+0.34}_{-0.09}$
$3.5 - 4.0$	3.72	$0.85 \pm 1.57\ ^{+0.14}_{-0.01}$
$4.0 - 10.0$	5.27	$0.10 \pm 1.02\ ^{+0.23}_{-0.06}$

Table 6.2: *The value of the Ross-Stodolsky skewing parameter n_{RS} extracted from the fits presented in figure 6.13 as a function of t. The first error is statistical and the second errors represent the systematic uncertainties due to varying the relativistic Breit-Wigner width.*

Since the effect of skewing is expected to depend on t, the invariant mass distribution is further studied in several t intervals. Figure 6.13 shows $d\sigma/dM_{\pi\pi}$ for 6 bins of t which, where statistics allow, are chosen to be the same as those used in the extraction of the t dependence. The curves again represent the result of a fit using the Ross-Stodolsky formalism but now with m_ρ and Γ_ρ fixed to their PDG values. The χ^2/ndf for all bins is satisfactory. In order to take into account the dependence of the skewing on the choice of the relativistic Breit-Wigner width, each fit is repeated for the alternative parameterisations given in equations 6.10 and 6.12 and the variation included in the uncertainty on n_{RS}. The resulting skewing parameters are presented in table 6.2 and figure 6.14 as a function of the mean t value for each bin. A significant skewing effect is only observed in the lowest $|t|$ bin, $1.5 < |t| < 2.0$ GeV^2, above this it is consistent with zero. In this t range the value of the skewing parameter is $n_{RS} = 0.93\ ^{+0.48}_{-0.34}$, where the error is the result of the statistical error and the systematic error due to the choice of relativistic Breit-Wigner width added in quadrature.

The invariant mass distribution in the MC was reweighted to the form given in

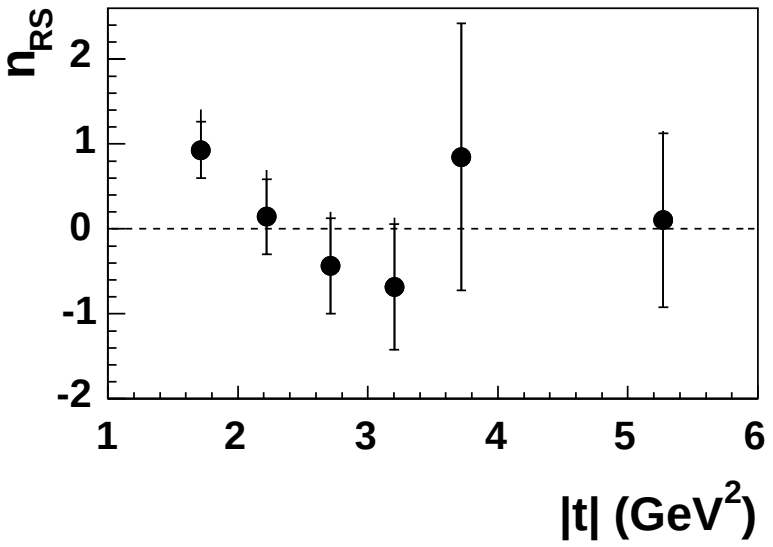

Figure 6.14: *The value of the Ross-Stodolsky skewing parameter n_{RS} extracted from the fits presented in figure 6.13 as a function of t. The inner error bars show the statistical error and the outer ones represent the sum of the statistical error and the systematic error due to varying the relativistic Breit-Wigner width added in quadrature.*

equation 6.13 with the skewing factor n_{RS} implemented according to the result of the fit for the range $1.5 < |t| < 2.0$ GeV^2 and set to zero elsewhere. This procedure was applied iteratively until no further change was observed in the fit parameters.

In order to correct the cross section for the effect of skewing, a correction factor $C_{skewing}$ is introduced. This factor is simply the ratio of the original Breit-Wigner distribution (equation 6.9) to the skewed distribution (equation 6.13) integrated over the measured invariant mass interval:

$$C_{skewing} = \frac{\int_{0.6}^{1.1} BW_\rho}{\int_{0.6}^{1.1} (BW_\rho + \text{skewing})}. \tag{6.16}$$

Using the skewing parameters determined above, the resulting correction factor is $C_{skewing} = 1.026\ ^{+0.009}_{-0.008}$ for the range $1.5 < |t| < 2.0$ GeV^2 and zero elsewhere. The error represents the uncertainty on the skewing factor obtained from the fit described above, including the error due to the choice of relativistic Breit-Wigner width, and

is included in the sources of systematic error (see section 6.5) for the measurement of the t dependence.

6.5 Error Determination

Two types of error contribute to the uncertainty of the final measurement: statistical and systematic. For a sample of N events, each having a weight w_i, the statistical error is calculated according to

$$\sigma_{stat} = \sqrt{\sum_{i=1}^{N} w_i^2}, \tag{6.17}$$

which reduces to $\sqrt{N}$ in the case that all weights are unity. The systematic errors estimate the systematic uncertainty on the detector measurements and the model dependencies used in the MC simulation. In the latter case, only one MC simulation is used and the systematic error is estimated by reweighting the input parameters. These errors can be split into uncorrelated errors, which affect each bin independently, and correlated errors, which affects all the bins equally. Since all cross sections are normalised to unity and only the shape is important, the latter has no effect on the results and is ignored. The remaining systematic errors, which are treated as uncorrelated, are estimated on a bin-by-bin basis using the MC simulation. For each quantity considered, the value is shifted first up and then down by its estimated error and the result recalculated in each case. The difference between the shifted result and the nominal result in each case determines the systematic error due to that source. The individual sources of systematic error are then combined in quadrature. The addition is performed separately for those sources which lead to an increase in the result and those which lead to a decrease, allowing the possibility of asymmetric error contributions.

The sources of systematic error considered can be split into three main categories and are as follows:

- **Uncertainties in the ρ simulation**

  The slope of the t distribution, used to compute acceptances and smearing effects and to adjust the measurements to the mean t value for each t interval, is varied by reweighting the Monte Carlo t distribution by $(1/|t|)^{\pm 0.5}$. A conservatively large variation is assigned to this uncertainty in order to cover possible variations of the measured exponent with the fitted t range (see section 7.1). The uncertainty in the modelling of the dissociative proton system Y is estimated by reweighting the proton remnant mass distribution by $(1/M_Y^2)^{\pm 0.3}$. For the angular distributions, the spin density matrix elements are varied around the values measured in the current data according to the spread of the observed results with t: $\pm$ 0.033 for r_{00}^{04} (which encompasses the prediction of SCHC), $\pm$ 0.02 for $\mathrm{Re}\,[r_{10}^{04}]$ and $^{+0.02}_{-0.04}$ for r_{1-1}^{04}. Finally, in the low $|t|$ region where non-zero skewing is observed in the ρ line shape, the skewing parameter is varied according to the uncertainty of the fit result, as discussed in section 6.4.

- **Uncertainties on the background distributions**

  The normalisations of the background contributions are varied by modifying the ratio of each background's cross section to the ρ cross section within the error limits quoted in section 5.3, namely: $\pm$ 0.02 for $\sigma_\omega/\sigma_\rho$ [101], $\pm$ 0.05 for σ_ϕ/σ_ρ [62] and $\pm$ 0.1 for $\sigma_{\rho'}/\sigma_\rho$ [125]. The t dependence of the ρ' distribution, which provides the largest background, is further varied using weighting factors of $(1/|t|)^{\pm 2.0}$.

- **Uncertainties in the detector description**

  The uncertainties on the tracking description at large θ and their effect on the stability of the dip in the ϕ^* acceptance (see section 6.1.2) are estimated by varying the cut on the θ angle of the reconstructed tracks between 150° and 160°. For the LAr, the energy threshold for the detection of energy deposits that are not associated to the two pion candidates is varied from 300 MeV to

500 MeV. The error on the description of the electron tagger is estimated by shifting the acceptance sideways by 3% as a function of y. Finally, the errors on the trigger efficiency and its reweight, as discussed in section 6.3, are taken into account.

For the t dependence, the largest sources of systematic uncertainty are the slope of the t distribution in the MC, the LAr noise subtraction and the variation of the upper θ cut. Additionally, in the case of the spin density matrix elements, the parameterisation of the matrix elements in the MC provides a significant effect. For all contributions, the effect on the t dependence is less than $\pm 1\%$, and less than ± 0.015 in the spin density matrix elements.

Chapter 7

Results and Discussion

This chapter presents the results of the analysis for the kinematic range stated in section 5.1.8. Firstly, the normalised differential cross section in t, $1/\sigma\ d\sigma/d|t|$, is studied. The helicity structure of diffractive ρ meson production, and its dependence on t, is then investigated. The results are compared to the predictions arising from the LL BFKL model of Poludniowski *et al.* described in section 4.3.3. Here, the free parameters of the theory are taken as $\alpha_s^{IF} = 0.21$, $\alpha_s^{BFKL} = 0.20$ and $\gamma = 1$. These values represent a recent parameterisation [132], which provides as good a fit of the previous data as those parameter values presented in section 4.3.3. The predictions are generated using the CTEQ5L PDFs, with $|t|$ as the hard scale, and a mean $W \approx 87$ GeV.

7.1 The t Dependence

Figure 7.1 presents the normalised differential cross section in t. The data are plotted at the mean t value for each of the eight t intervals, as determined in section 6.2 using a power-law parameterisation of the data. The inner error bars show the binomial statistical error, which is the dominant uncertainty, and the outer error bars show

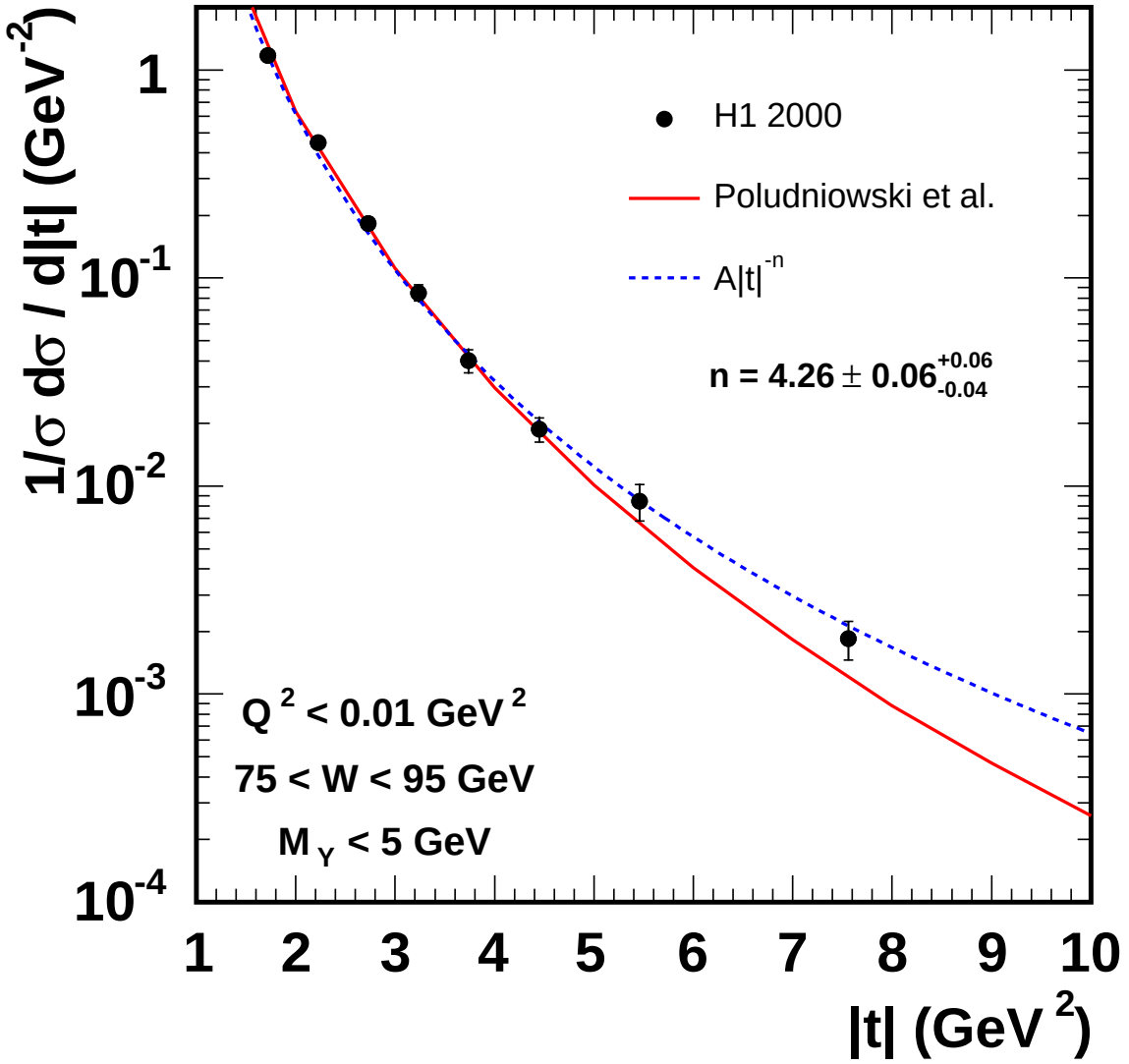

Figure 7.1: *The t dependence of the cross section. The inner error bars show the statistical errors, which are the dominant uncertainty, and the outer ones represent the sum of the statistical and point-to-point systematic errors added in quadrature. The dashed line is the result of a fit to a power-law distribution* $A|t|^{-n}$*, which results in a power* $n = 4.26 \pm 0.06\ (\text{stat.})\ ^{+0.06}_{-0.04}\ (\text{syst.})$*. The solid line shows the prediction from the BFKL model of Poludniowski* et al.

the sum of the statistical and systematic errors added in quadrature.

As mentioned earlier, the t cross section for a hard production mechanism is expected to follow an approximate power-law dependence, with a power given by $n \sim 3-4$ [108]. Hence, the data are first compared to a power-law parameterisation of the form $1/\sigma\ d\sigma/d|t| = A|t|^{-n}$ (see dotted line in figure 7.1). For the measured t range, the data are reasonably described by a power

$$n \ = \ 4.26 \ \pm \ 0.06 \ (\text{stat.}) \ ^{+0.06}_{-0.04} \ (\text{syst.}) \tag{7.1}$$

with a $\chi^2/ndf \ = \ 10.64/6$. The first error is the statistical uncertainty and the second are the systematic uncertainties, the latter being derived as outlined in section 6.5. The data are incompatible ($\chi^2/ndf \ = \ 54.30/6$) with an exponential behaviour $d\sigma/dt \propto e^{-b|t|}$, which is observed to give a good description of the elastic ρ cross section at low $|t|$ [98, 131].

The power-law parameterisation is only an approximation. In the case of the previous H1 J/ψ measurement discussed in section 4.3.2, the extracted power was seen to vary depending on the region in t included in the fit. Consequently, the fit procedure is repeated in several different t ranges to check for any variation of the power, n, on the fitted t range. Each time, the fit range is limited by excluding one more bin in $|t|$, starting with the lowest. The extracted values of n are shown in figure 7.2 as a function of the mean $|t|$ value for the lowest bin included, $|t_0|$. Within the experimental uncertainties, no significant variation of the extracted power on t is observed.

The solid line in figure 7.1 shows the prediction from the BFKL model of Poludniowski *et al.* The theoretical cross section has been normalised to unity by dividing by the predicted integrated cross section for the range $1.5 < |t| < 10.0$ GeV^2, which is 33.3 nb. The final result gives a satisfactory description of the t dependence, although there is a tendency for the model to underestimate the data at the largest $|t|$. It should be noted, however, that the model parameters are tuned to the previ-

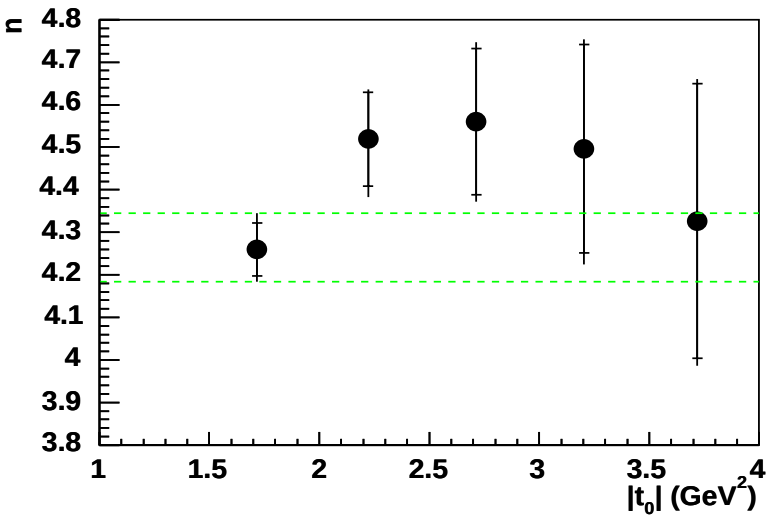

Figure 7.2: *The variation of the measured power, n, with the fitted t range, as a function of the starting point of the fit, $|t_0|$. The inner error bars show the statistical error and the outer ones show the sum of the statistical and systematic errors added in quadrature.*

ous ZEUS data [62], which is measured in a different kinematic range to the results presented here. Tuning the parameters to the present data is likely to provide an improved description.

Let us now compare this result to that of the ZEUS Collaboration discussed in section 4.3.2. They measure a power $n = 3.21 \pm 0.04$ (stat.) ± 0.15 (syst.) for the ρ meson in the range $1.2 < |t| < 10$ GeV^2, $80 < W < 120$ GeV and $x > 0.01$ [62]. This is significantly shallower than the result obtained here but, as seen in section 4.3.3, is also well described by the BFKL model using similar parameters. The difference in slope can be understood in terms of the difference in the kinematic region over which the two measurements are made, in particular the minimum value of x which enters into the integral in equation 4.33. Using equation 4.29, the restriction $M_Y < 5$ GeV applied in this analysis corresponds to $x_{min} \simeq 0.06$ at $|t| = 1.5$ GeV^2 and $x_{min} \simeq 0.3$ at $|t| = 10.0$ GeV^2. It is this more restrictive value of x_{min}, compared to the ZEUS value of $x_{min} = 0.01$, which accounts for the increased steepness of the t spectrum presented here.

7.2 Helicity Structure

As discussed in section 4.3.1, measurements of the angular production and decay distributions for diffractive vector meson production provide a handle by which to investigate the helicity structure of the interaction. Here, the angular decay distributions $\cos\theta^*$ and ϕ^* are measured and the spin density matrix elements extracted using a two-dimensional log likelihood fit of equation 4.22 to the data in several $|t|$ intervals. The equation is fitted to the uncorrected data with all corrections, including the adjustment for background contributions, being applied instead to the fit function. The details of the fit procedure are given in appendix A.1. The two-dimensional fit has the advantage that the matrix element $\mathrm{Re}\,[r^{04}_{10}]$ can be extracted in addition to the r^{04}_{00} and r^{04}_{1-1} elements obtainable from the one-dimensional distributions (equations 4.23 and 4.24). The values of r^{04}_{00} and r^{04}_{1-1} obtained from the two-dimensional fit are consistent with those obtained from the corresponding one-dimensional fit.

Figure 7.3 shows the normalised single differential distributions in $\cos\theta^*$ and ϕ^* for three intervals in $|t|$. Again, the inner error bars show the statistical error and the outer error bars show the sum of the statistical and systematic errors added in quadrature. The solid curves show the projection of the two-dimensional fit described above and the dashed lines represent the prediction from SCHC. In the case of the ϕ^* distribution, a flat behaviour is clearly disfavoured (χ^2/ndf ranges from 12.00/5 to 41.59/5), indicating a violation of SCHC. However, the two-dimensional fit provides a good description of the data for both distributions.

The values of the three extracted matrix elements are given in table 7.1 and figure 7.4 as a function of $|t|$. The correlations between the different parameters (see appendix A.2) are generally small and have been neglected here. Also shown in figure 7.4 are the previous measurements obtained by the ZEUS Collaboration [62]. Good agreement is observed between the results of the two experiments. Within the

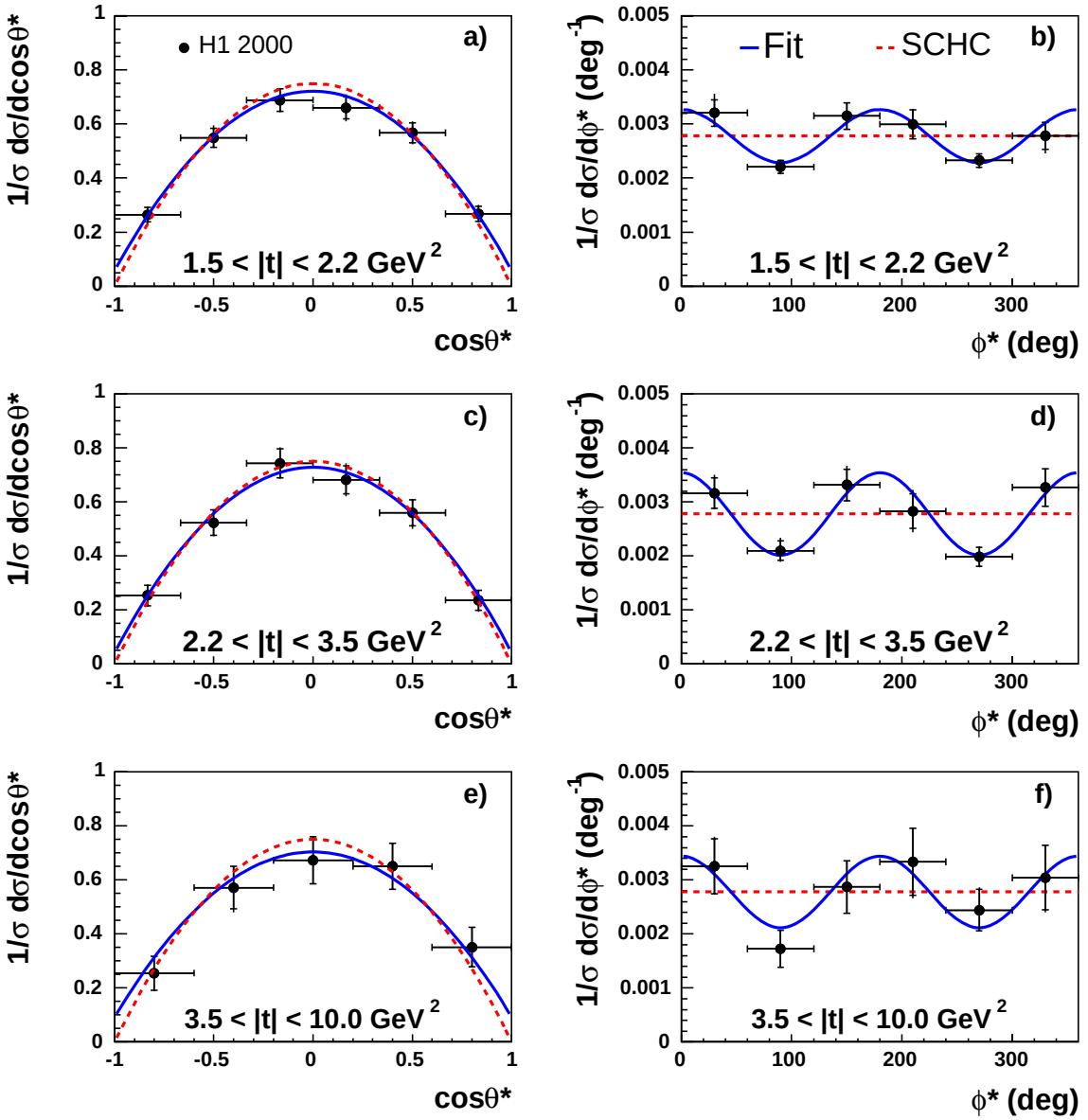

Figure 7.3: *The normalised decay angular distributions for ρ meson production in three bins of $|t|$: (a,b) $1.5 < |t| < 2.2$ GeV^2; (c,d) $2.2 < |t| < 3.5$ GeV^2 and (e,f) $2.5 < |t| < 10.0$ GeV^2. The left column (a,c,e) shows the polar decay distribution, $\cos\theta^*$, and the right column (b,d,f) shows the azimuthal decay distribution, ϕ^*. The inner error bars show the statistical errors, while the outer ones represent the sum of the statistical and point-to-point systematic errors added in quadrature. The dashed line shows the prediction from s-channel helicity conservation and the solid lines show the results of two-dimensional fit to the data described in the text.*

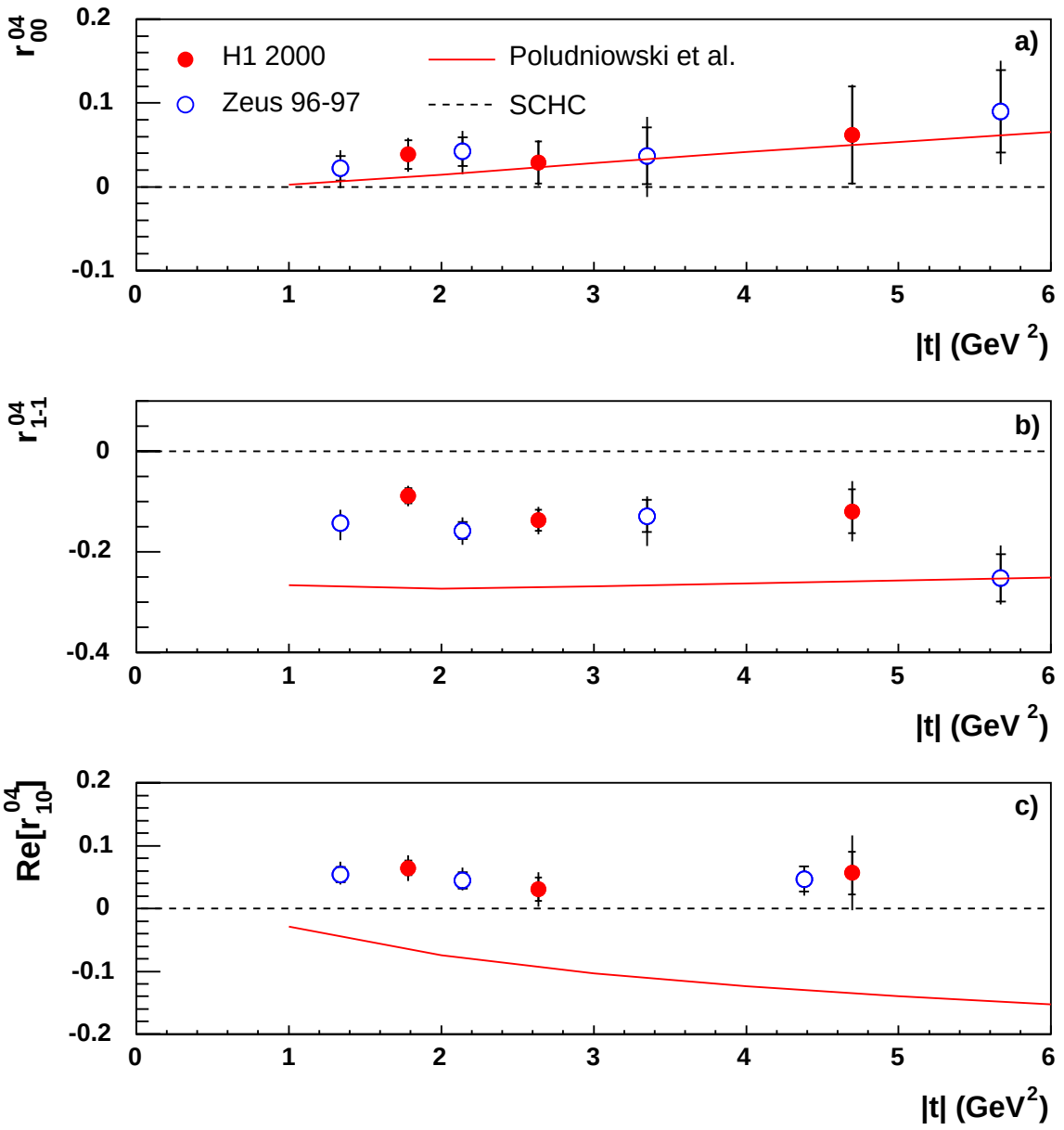

Figure 7.4: *The three spin density matrix elements (a) r_{00}^{04}, (b) r_{1-1}^{04} and (c) $\mathrm{Re}\,[r_{10}^{04}]$ for the ρ meson as a function of $|t|$ (filled points) together with previous ZEUS measurements [62] (open points). The inner error bars show the statistical errors, while the outer ones represent the sum of the statistical and systematic errors added in quadrature. The dashed lines show the prediction from s–channel helicity conservation and the solid lines show the prediction from the BFKL model of Poludniowski* et al.

$\|t\|$ range (GeV^2)	$\langle\|t\|\rangle$ (GeV^2)	r_{00}^{04}	r_{1-1}^{04}	$\mathrm{Re}\,[r_{10}^{04}]$
$1.5 - 2.2$	1.79	$0.038 \pm 0.017\ ^{+0.011}_{-0.012}$	$-0.088 \pm 0.015\ ^{+0.007}_{-0.014}$	$0.064 \pm 0.012\ ^{+0.005}_{-0.015}$
$2.2 - 3.5$	2.64	$0.029 \pm 0.025\ ^{+0.010}_{-0.013}$	$-0.138 \pm 0.021\ ^{+0.011}_{-0.011}$	$0.031 \pm 0.019\ ^{+0.007}_{-0.011}$
$3.5 - 10.0$	4.69	$0.062 \pm 0.058\ ^{+0.015}_{-0.012}$	$-0.119 \pm 0.044\ ^{+0.011}_{-0.009}$	$0.057 \pm 0.034\ ^{+0.004}_{-0.007}$

Table 7.1: *The three spin density matrix elements r_{00}^{04}, r_{1-1}^{04} and $\mathrm{Re}\,[r_{10}^{04}]$ for ρ meson production as a function of $|t|$ for the kinematic region defined in section 5.1.8. The first error is statistical and the second errors are systematic.*

experimental uncertainty, no strong dependence on t is observed. The small values of r_{00}^{04}, which is directly proportional to the single-flip helicity amplitude M_{+0}, signify that the probability of producing a longitudinally polarised ρ from a transversely polarised photon is low, varying from $(4 \pm 2)\%$ at $|t| = 1.79$ GeV^2 to $(6 \pm 6)\%$ at $|t| = 4.69$ GeV^2. The non-zero values of $\mathrm{Re}\,[r_{10}^{04}]$ indicate that, although small, a single-flip contribution is present. The production of transversely polarised ρ mesons must, therefore, dominate and the finite negative values of r_{1-1}^{04} show clear evidence for a helicity double-flip contribution. Both these observations indicate a violation of the SCHC hypothesis, the prediction of which is shown by the dashed lines.

Comparing the results to the BFKL predictions arising from the model of Poludniowski *et al.*, which are shown by the solid lines in figure 7.4, one can see that only r_{00}^{04} is well described. The model prediction for r_{1-1}^{04} is too large in magnitude and it gives the wrong sign for $\mathrm{Re}\,[r_{10}^{04}]$. With respect to the overestimation of r_{1-1}^{04}, it is again noted that the model is only leading order in this quantity. The inability to describe the sign of $\mathrm{Re}\,[r_{10}^{04}]$ remains the major obstacle to providing a good description of the data. As mentioned in section 4.3.3, future improvements in the description of $\mathrm{Re}\,[r_{10}^{04}]$ may come about through inclusion of Sudakov factors to suppress the emission of radiation off the quark-antiquark pair, although this remains to be studied.

Chapter 8

Summary

Exclusive vector meson production provides a powerful means by which to probe the structure of the diffractive exchange. In this analysis, the diffractive photoproduction of ρ mesons with large momentum transfer is studied in ep interactions at HERA. The ρ meson is identified via its decay into two charged pions. The data correspond to an integrated luminosity of 20.1 pb^{-1} and cover the kinematic range $Q^2 < 0.01$ GeV^2, $75 < W < 95$ GeV and $M_Y < 5$ GeV. Such reactions have been proposed as an ideal testing ground for BFKL dynamics and the results are compared to the leading logarithm (LL) BFKL model of Poludniowski *et al.*

The invariant mass distribution of the two decay pions is studied in the range $0.6 < M_{\pi\pi} < 1.1$ GeV. Clear evidence for a ρ signal is observed, with a mass and decay width compatible with that quoted by the PDG. Possible distortion of the mass distribution due to the interference with open $\pi^+\pi^-$ production is investigated using the Ross-Stodolsky parameterisation. Only at the lowest $|t|$ values is a noticeable skewing effect observed with $n_{RS} = 0.93\ ^{+0.48}_{-0.34}$ for the range $1.5 < |t|$ 2.0 GeV^2.

The dependence of the cross section on the square of the four momentum transfer of the diffractive exchange, $|t|$, is measured in the range $1.5 < |t| < 10.0$ GeV^2. The resulting distribution is reasonably described by the BFKL model prediction. Includ-

ing the current experimental results in the tuning of the model parameters is likely to further improve this description. Fitting the data with a power-law parameterisation of the form $d\sigma/dt \propto |t|^{-n}$, yields a power $n = 4.26 \pm 0.06$ (stat.) $^{+0.06}_{-0.04}$ (syst.) for the measured t range. Further, the data are incompatible with an exponential distribution, which describes the data well at low $|t|$.

The helicity structure of the reaction is studied using an analysis of the decay angular distributions and the spin density matrix elements r^{04}_{00}, r^{04}_{1-1} and $\mathrm{Re}\,[r^{04}_{10}]$ are extracted in three $|t|$ intervals. The $\mathrm{Re}\,[r^{04}_{10}]$ and r^{04}_{1-1} matrix elements differ significantly from zero, signifying the presence of a helicity single-flip and double-flip contribution respectively. This violates the hypothesis of s-channel helicity conservation. The small value of the r^{04}_{00} matrix element, which depends directly on the helicity single-flip amplitude, indicates that the probability of producing a longitudinally polarised ρ meson is small and, hence, that the production of transversely polarised ρ mesons dominates. These results are in good agreement with those previously measured by the ZEUS Collaboration. Unlike previous two-gluon calculations, the BFKL model is able to qualitatively reproduce the observed dominance of transverse ρ production. However, although able to describe the small value of r^{04}_{00}, it overestimates the magnitude of r^{04}_{1-1} and predicts the wrong sign for $\mathrm{Re}\,[r^{04}_{10}]$. The inability to describe the sign of $\mathrm{Re}\,[r^{04}_{10}]$ is the major obstacle in providing a good description of the data at present. Future improvements of the theoretical model through the inclusion of Sudakov suppression factors may reduce this discrepancy but their effect has yet to be studied.

In summary, HERA data on diffractive production of light vector mesons at large momentum transfer are proving difficult to explain. LL BFKL models are able to explain the t spectra of the vector mesons but at present are unable to provide a satisfactory description of the helicity structure. Hopefully, the higher luminosity afforded by the HERA II era will enable the measurement to be extended to larger values of $|t|$ and the uncertainties reduced.

Appendix A

Extraction of Spin Density Matrix Elements

This appendix outlines the log likelihood [133] fit procedure used in the extraction of the spin density matrix elements described in section 7.2 of this thesis. The correlations between the resulting fit parameters are also considered.

A.1 Log Likelihood Fit Procedure

The spin density matrix elements are extracted from the distribution of the decay angles $\cos\theta^*$ and ϕ^*. Let the number of data events in a particular bin of $\cos\theta^*$ and ϕ^* be D_k, where $k = 1...n$ and n is the total number of bins in the distribution. One recalls from equation 4.22 that the normalised angular distribution is given by

$$\begin{aligned} W_k(r_{ij}^{04}) &= \frac{3}{4\pi}\left[\frac{1}{2}(1-r_{00}^{04}) + \frac{1}{2}(3r_{00}^{04}-1)\cos^2\theta^* \right. \\ &\quad \left. -\sqrt{2}\mathrm{Re}\left[r_{10}^{04}\right]\sin 2\theta^*\cos\phi^* - r_{1-1}^{04}\sin^2\theta^*\cos 2\phi^*\right], \end{aligned} \tag{A.1}$$

where r_{ij}^{04} are the spin density matrix elements, to be determined by the fit procedure. In order to compare this equation to the data one must first correct for

detector acceptances and efficiencies, C_k, and background contributions, B_k, which are described in chapter 6. Due to the Poisson nature of the likelihood function, these corrections are applied to the fit function rather than the data. Hence, the function describing the data can be written as

$$F_k(r_{ij}^{04}) = \frac{N(r_{ij}^{04})W_k(r_{ij}^{04})C_k}{\sum_{k=1}^{n} W_k(r_{ij}^{04})C_k} + B_k, \tag{A.2}$$

where $N(r_{ij}^{04})$ is an extra normalisation parameter, to be determined by the fit for each set of matrix elements.

For each bin k, the probability of observing D_k data events for an expectation of $F_k(r_{ij}^{04})$ is given by the Poisson formula

$$P(D_k : F_k(r_{ij}^{04})) = \frac{e^{-F_k(r_{ij}^{04})} F_k(r_{ij}^{04})^{D_k}}{D_k!}. \tag{A.3}$$

The binned likelihood is defined as the product of the probabilities for each bin:

$$\mathcal{L}(r_{ij}^{04}) = \prod_{k=1}^{n} P(D_k : F_k(r_{ij}^{04})). \tag{A.4}$$

This can then be converted into the more mathematically useful log likelihood,

$$\begin{aligned} \ln \mathcal{L}(r_{ij}^{04}) &= \sum_{k=1}^{n} \ln \left[P(D_k : F_k(r_{ij}^{04})) \right] \\ &= \sum_{k=1}^{n} \left[D_k \ln F_k(r_{ij}^{04}) - F_k(r_{ij}^{04}) - \ln D_K! \right], \end{aligned} \tag{A.5}$$

which has the advantage of transforming the product over bins into a sum. Using Sterling's approximation, $\ln a! \approx a \ln a - a$, the final expression for the log likelihood as a function of r_{ij}^{04} is given by

$$-2 \ln \mathcal{L}(r_{ij}^{04}) = \sum_{k=1}^{n} \left[2(F_k(r_{ij}^{04}) - D_k) + 2D_k \ln \left(\frac{D_k}{F_k(r_{ij}^{04})} \right) \right] \tag{A.6}$$

where the factor of -2 has been introduced such that $-2 \ln \mathcal{L}$ mimics a χ^2 and the most probable parameter set corresponds to its minimum.

Having defined the likelihood function, one can scan the parameter space and minimise equation A.6 as a function of the spin density matrix elements r_{ij}^{04}. This is performed iteratively using the MINUIT minimisation package [134]. The minimum value of $-2\ln\mathcal{L}$ then defines the preferred values of the matrix elements and the contours give the corresponding uncertainties.

A.2 Correlations

This section discusses to what extent the parameters resulting from the two-dimensional fit are correlated with each other. The correlation matrices for $(r_{00}^{04}, \mathrm{Re}\left[r_{10}^{04}\right], r_{1-1}^{04}, N)$ in the three t intervals are:

$$\begin{pmatrix} 1.000 & -0.002 & 0.142 & 0.005 \\ -0.002 & 1.000 & 0.110 & 0.000 \\ 0.142 & 0.110 & 1.000 & 0.003 \\ 0.005 & 0.000 & 0.003 & 1.000 \end{pmatrix} \quad \text{for} \quad 1.5 < |t| < 2.2 \text{ GeV}^2,$$

$$\begin{pmatrix} 1.000 & 0.005 & 0.087 & 0.009 \\ 0.005 & 1.000 & 0.194 & -0.003 \\ 0.087 & 0.194 & 1.000 & 0.003 \\ 0.009 & -0.003 & 0.003 & 1.000 \end{pmatrix} \quad \text{for} \quad 2.2 < |t| < 3.5 \text{ GeV}^2 \text{ and}$$

$$\begin{pmatrix} 1.000 & 0.152 & 0.173 & 0.004 \\ 0.152 & 1.000 & 0.100 & -0.003 \\ 0.173 & 0.100 & 1.000 & 0.003 \\ 0.004 & -0.003 & 0.003 & 1.000 \end{pmatrix} \quad \text{for} \quad 3.5 < |t| < 10.0 \text{ GeV}^2.$$

Both r_{00}^{04} and $\mathrm{Re}\left[r_{10}^{04}\right]$ show some correlation with r_{1-1}^{04}, the largest of which is around 20%. Due to the relatively small size of the correlations, they are neglected in the calculation of the final results.

Bibliography

[1] R. K. Ellis, W. J. Stirling and B. R. Webber, *QCD and Collider Physics* Cambridge University Press (1996).

[2] T. Regge, *Introduction To Complex Orbital Momenta*, Nuovo Cim. **14** (1959) 951;
T. Regge, *Bound States, Shadow States And Mandelstam Representation*, Nuovo Cim. **18** (1960) 947.

[3] J. R. Forshaw and D. A. Ross, *Quantum Chromodynamics And The Pomeron*, Cambridge University Press (1997).

[4] M. Derrick *et al.* [ZEUS Collaboration], *Observation of events with a large rapidity gap in deep inelastic scattering at HERA*, Phys. Lett. B **315** (1993) 481;
T. Ahmed *et al.* [H1 Collaboration], *Deep inelastic scattering events with a large rapidity gap at HERA*, Nucl. Phys. B **429** (1994) 477.

[5] H1 Collaboration, *Diffractive photoproduction of ρ mesons with large momentum transfer at HERA*, Proceedings of XIII International Workshop on Deep Inelastic Scattering (2005), Madison, USA.

[6] H1 Collaboration, *H1 measurements of deeply virtual Compton scattering and vector meson production*, Talk presented at the Workshop on Low x Physics (2005), Sinaia, Romania.

[7] H1 Collaboration, *ep Physics beyond 1999*, H1 Internal Note, **H1–IN–531 (10/1997)**.

[8] I. Abt *et al.* [H1 Collaboration], *The H1 Detector at HERA*, Nucl. Instrum. Meth. A **386** (1997) 310; 348.

[9] D. Pitzl *et al.*, *The H1 silicon vertex detector*, Nucl. Instrum. Meth. A **454** (2000) 334 .

[10] W. Eick *et al.*, *Development of the H1 backward silicon strip detector*, Nucl. Instrum. Meth. A **386** (1997) 81.

[11] J. Burger *et al.*, *The Central Jet Chamber of the H1 Experiment*, Nucl. Instrum. Meth. A **279** (1989) 217.

[12] S. Egli *et al.*, *The Central–Inner Z–Drift Chamber of the H1 Experiment*, Nucl. Instrum. Meth. A **283** (1989) 487.

[13] K. Müller *et al.*, *Construction and Performance of a Thin Cylindrical Multiwire Proportional Chamber with Cathode Pad Readout for the H1 Experiment*, Nucl. Instrum. Meth. A **312** (1992) 457.

[14] S. Burke *et al.*, *Track finding and fitting in the H1 forward track detector*, Nucl. Instrum. Meth. A **373** (1996) 227.

[15] I. Abt *et al.* [H1 Collaboration], *Technical Proposal for the Upgrade of the Backward Region of the H1 Detector*, DESY Internal Report, **PRC-93-02**.

[16] B. Andrieu *et al.* [H1 Calorimeter Group], *The H1 Liquid Argon Calorimeter System*, Nucl. Instrum. Meth. A **336** (1993) 460.

[17] H. Wellisch *et al.*, *Hadronic Calibration of the H1 LAr Callorimeter using Software Weighting techniques*, H1 Internal Note, **H1–IN–346 (02/1994)**.

[18] B. Andrieu *et al.* [H1 Calorimeter Group], *Beam Tests and Calibration of the H1 Liquid Argon Calorimeter with Electrons*, Nucl. Instrum. Meth. A **350** (1994) 57.

[19] B. Andrieu *et al.* [H1 Calorimeter Group], *Results from Pion Calibration Runs for the H1 Liquid Argon Calorimeter and Comparisons with Simulations*, Nucl. Instrum. Meth. A **336** (1993) 499.

[20] R. D. Appuhn *et al.* [H1 SpaCal Group], *The H1 Lead/Scintillating–fibre Calorimeter*, Nucl. Instrum. Meth. A **386** (1997) 397.

[21] T. Nicholls *et al.* [H1 SpaCal Group], *Performance of an Electromagnetic Lead/Scintillating–fibre Calorimeter for the H1 Detector*, Nucl. Instrum. Meth. A **374** (1996) 149.

[22] R. D. Appuhn *et al.* [H1 SpaCal Group], *H1 Backward Upgrade with a SPACAL Calorimeter: The Hadronic Section*, DESY Report, **DESY-96-013**.

[23] R. D. Appuhn *et al.* [H1 SpaCal Group], *Hadronic Response and e/π– Separation with the H1 Lead/Fiber Calorimeter*, Nucl. Instrum. Meth. A **382** (1996) 395.

[24] T. Ahmed *et al.* [H1 Collaboration], *The H1 Forward Muon Spectrometer*, Nucl. Instrum. Meth. A **340** (1994) 304.

[25] H1 Collaboration, *Luminosity Measurement in the H1 Experiment at HERA*, contributed paper to *ICHEP96, Warsaw 1996*, **ICHEP96pa17-026**.

[26] H. Bethe and W. Heitler, *On the Stopping of Fast Particles and on the Creation of Positive Electrons*, Proc. Roy. Soc. Lond. **A146** (1934) 83.

[27] H1 Collaboration, *H1 Luminosity Summary*, http://www-h1.desy.de/h1det/lumi/summary_tables/summary.html (2000).

[28] V. Andreev, *Acceptance Determination of Electon Tagger (ET44) in 1995*, H1 Internal Note, **H1–IN–493 (10/1996)**.

[29] H1 Collaboration, *A Fast Track Trigger with Higher Resolution for H1*, DESY Internal Report, **PRC-99-06**.

[30] E. Elsen, *The H1 Trigger and Data Acquisition*, contributed paper to *International Symposium on Electronic Instrumentation in Physics, Dubna 1991*, H1 Internal Note, **H1-IN-262 (01/1993)**;
F. Sefkow *et al.*, *Experience with the First Level trigger of H1*, contributed paper to *The 1994 IEEE Nuclear Science Symposium, Virginia 1994*, H1 Internal Note, **H1-IN-407 (11/1994)**.

[31] J. C. Bizot *et al.*, *Status of Simulation for a Topological Level 2 Trigger*, H1 Internal Note, **H1-IN-212 (02/1992)**;
J. C. Bizot *et al.*, *Strategy Studies for the H1 Topological L2–Trigger (L2TT)*, H1 Internal Note, **H1-IN-508 (01/1997)**.

[32] J. H. Köhne *et al.*, *Realization of a Second Level Neural Network Trigger for the H1 experiment at HERA*, H1 Internal Note, **H1-IN-509 (01/1997)**.

[33] S. Aid *et al.* [H1 Collaboration], *Guide to the Simulation Program H1Sim*, H1 Internal Report (1995).

[34] S. Eichenberger *et al.*, *A Fast Pipelined Trigger for the H1 Experiment based on Multiwire Proportional Chamber Signals*, Nucl. Instrum. Meth. A **323** (1992) 532.

[35] H. Beck, *Principles and Operation of the z-Vertex Trigger*, H1 Internal Note, **H1-IN-479 (05/1996)**.

[36] J. Riedlberger, *The H1 Trigger with emphasis on Tracking Triggers*, H1 Internal Note, **H1-IN-419 (01/1995)**.

[37] M. zur Nedden and B. Reisert, *The H1 Liquid Argon Trigger Calibration: Overview, Description and Performance*, H1 Internal Note, **H1-IN-593 (04/2001)**.

[38] B. List and A. Mastroberardino, *DIFFVM: A Monte Carlo generator for diffractive processes in ep Scattering*, Prepared for Workshop on Monte Carlo Generators for HERA Physics (Plenary Starting Meeting), Hamburg, Germany, 27-30 Apr 1998.

[39] R. Brun *et al.*, *GEANT3 User's Guide*, **CERN-DD/DD-84-1**.

[40] ZEUS Collaboration, *Combined ZEUS & H1 Plots for Moriond EW 2004*, http://www-zeus.desy.de/physics/sfew/PUBLIC/sfew_results/preliminary/moriond04/zeush1.php (2004).

[41] B. Foster, *Lectures on HERA physics*, Lectures given at Corfu Summer Institute on Elementary Particle Physics (Corfu 2001), Corfu, Greece, 31 Aug - 20 Sep 2001 [hep-ex/0206011].

[42] F. Halzen and A. Martin, *Quarks and Leptons*, Wiley (1984).

[43] C. Adloff *et al.* [H1 Collaboration], *Measurement and QCD analsis of neutral and charged current cross sections at HERA*, Eur. Phys. J. C **30** (2003) 1.

[44] S. Chekanov *et al.* [ZEUS Collaboration], *Measurement of the neutral current cross section and F_2 structure function for deep inelastic e^+p scattering at HERA*, Eur. Phys. J. C **21** (2001) 443.

[45] A. C. Benvenuti *et al.* [BCDMS Collaboration], *A High Statistics Measurement Of The Deuteron Structure Functions F_2 (X, Q^2) And R From Deep Inelastic Muon Scattering At High Q^2*, Phys. Lett. B **237** (1990) 592.

[46] M. Arneodo *et al.* [New Muon Collaboration.], *Measurement of the proton and the deuteron structure functions, F_2^p and F_2^d*, Phys. Lett. B **364** (1995) 107

[47] E. D. Bloom *et al.*, *High-Energy Inelastic E P Scattering At 6-Degrees And 10-Degrees*, Phys. Rev. Lett. **23** (1969) 930;
M. Breidenbach *et al.*, *Observed Behavior Of Highly Inelastic Electron - Proton Scattering*, Phys. Rev. Lett. **23** (1969) 935;
J. I. Friedman and H. W. Kendall, *Deep Inelastic Electron Scattering*, Ann. Rev. Nucl. Part. Sci. **22** (1972) 203.

[48] J. D. Bjorken, *Inequality for Backward Electron–Nucleon and Muon–Nucleon Scattering at High Momentum Transfer*, Phys. Rev. **163** (1967) 1767.

[49] R. Feynman, *Very High Energy Collisions of Hadrons*, Phys. Rev. Lett. **23** (1969) 1415;
J. D. Bjorken and E. Paschos, *Inelastic Electron–Proton and γ–Proton Scattering and the Structure of the Nucleon*, Phys. Rev. **185** (1969) 1975.

[50] C. G. Callan and D. J. Gross, *High-Energy Electroproduction And The Constitution Of The Electric Current*, Phys. Rev. Lett. **22** (1969) 156.

[51] G. Altarelli and G. Martinelli, *Transverse Momentum Of Jets In Electroproduction From Quantum Chromodynamics*, Phys. Lett. B **76** (1978) 89;
M. Gluck and E. Reya, *Transverse Momenta Of Partons And Dimuons In QCD*, Nucl. Phys. B **145** (1978) 24.

[52] C. Adloff *et al.* [H1 Collaboration], *Measurement of neutral and charged current cross-sections in positron proton collisions at large momentum transfer*, Eur. Phys. J. C **13** (2000) 609.

[53] S. Aid *et al.* [H1 Collaboration], *A Measurement and QCD Analysis of the Proton Structure Function $F_2(x, Q^2)$ at HERA*, Nucl. Phys. B **470** (1996) 3.

[54] M. Derrick *et al.* [ZEUS Collaboration], *Measurement of the F_2 structure function in deep inelastic e^+p scattering using 1994 data from the ZEUS detector at HERA*, Z. Phys. C **72** (1996) 399.

[55] Y. L. Dokshitzer, *Calculation of the Structure Functions for Deep Inelastic Scattering and e^+ and e^- Annihilation by Perturbatio n Theory in Quantum Chromodynamics*, Sov. Phys. JETP **46** (1977) 641;
V. N. Gribov and L. N. Lipatov, *Deep Inelastic ep Scattering in Perturbation Theory*, Sov. J. Nucl. Phys. **15** (1972) 438 and 675;
G. Altarelli and G. Parisi, *Asymptotic Freedom in Parton Language*, Nucl. Phys. **B126** (1977) 298.

[56] J. A. M. Vermaseren, A. Vogt and S. Moch, *The third-order QCD corrections to deep-inelastic scattering by photon exchange* Nucl. Phys. B **724** (2005) 3.

[57] E. A. Kuraev, L. N. Lipatov and V. S. Fadin, *The Pomeranchuk Singularity in Non–Abelian Gauge Theories*, Sov. Phys. JETP **45** (1977) 199;
I. I. Balitsky and L. N. Lipatov, *The Pomeranchuk Singularity in Quantum Chromodynamics*, Sov. J. Nucl. Phys. **28** (1978) 822.

[58] C. Adloff *et al.* [H1 Collaboration], *On the rise of the proton structure function F2 towards low x*, Phys. Lett. B **520** (2001) 183.

[59] R. S. Thorne, *Parton distributions*, Int. J. Mod. Phys. A **19** (2004) 1074.

[60] C. Adloff *et al.* [H1 Collaboration], *Forward jet and particle production at HERA*, Nucl. Phys. B **538** (1999) 3.

[61] A. Aktas *et al.* [H1 Collaboration], *Forward pi0 production and associated transverse energy flow in deep-inelastic scattering at HERA*, Eur. Phys. J. C **36** (2004) 441.

[62] S. Chekanov *et al.* [ZEUS Collaboration], *Measurement of proton dissociative diffractive photoproduction of vector mesons at large momentum transfer at HERA*, Eur. Phys. J. C **26** (2003) 389.

[63] A. Aktas *et al.* [H1 Collaboration], *Diffractive photoproduction of J/psi mesons with large momentum transfer at HERA*, Phys. Lett. B **568** (2003) 205.

[64] C. F. von Weizsäcker, *Radiation Emitted In Collisions Of Very Fast Electrons*, Z. Phys. **88** (1934) 612;
E. J. Williams, *Nature Of The High-Energy Particles Of Penetrating Radiation And Status Of Ionization And Radiation Formulae*, Phys. Rev. **45** (1934) 729.

[65] T. H. Bauer, R. D. Spital, D. R. Yennie and F. M. Pipkin, *The Hadronic Properties Of The Photon In High-Energy Interactions*, Rev. Mod. Phys. **50** (1978) 261 [Erratum-ibid. **51** (1979) 407].

[66] J. J. Sakurai, *Theory Of Strong Interactions*, Annals Phys. **11** (1960) 1;
J. J. Sakurai, *Vector Meson Dominance And High-Energy Electron Proton Inelastic Scattering*, Phys. Rev. Lett. **22** (1969) 981.

[67] J. J. Sakurai and D. Schildknecht, *Generalized Vector Dominance And Inelastic Electron - Proton Scattering*, Phys. Lett. B **40** (1972) 121.

[68] M. Greko, Nucl. Phys. B **63** (1973) 398.

[69] H1 Collaboration *Measurement of the Inclusive Cross Section for Diffractive Deep Inelastic Scattering at High* Q^2, Conf. paper 090, Intern. Europhysics Conf. on HEP, EPS03, Aachen (2003).

[70] A. Donnachie and P. V. Landshoff, *Small x: Two pomerons!*, Phys. Lett. B **437** (1998) 408.

[71] A. Sommerfeld, *Partial Differential Equations in Physics*, Academic Press (1949).

[72] A. C. Irving and R. P. Worden, *Regge Phenomenology*, Phys. Rept. **34** (1977) 117.

[73] G. F. Chew and S. C. Frautschi, *Principle Of Equivalence For All Strongly Interacting Particles Within The S Matrix Framework*, Phys. Rev. Lett. **7** (1961) 394;

G. F. Chew and S. C. Frautschi, *Regge Trajectories And The Principle Of Maximum Strength For Strong Interactions*, Phys. Rev. Lett. **8** (1962) 41.

[74] A. V. Barnes *et al.*, *Pion Charge Exchange Scattering At High-Energies*, Phys. Rev. Lett. **37** (1976) 76.

[75] A. S. Carroll *et al.*, *Total Cross-Sections Of $Pi^{\pm}$, $K^{\pm}$, P And Anti-P On Protons And Deuterons Between 200-Gev/C And 370-Gev/C*, Phys. Lett. B **80** (1979) 423;
G. Carboni *et al.*, *Evidence Of A Rise In The Anti-Proton - Proton Total Cross-Section At The Cern Intersecting Storage Rings*, Phys. Lett. B **113** (1982) 87.

[76] I. Y. Pomeranchuk, Sov. Phys. **3** (1956) 306;
L. B. Okun and I.Y. Pomeranchuk, Sov. Phys. JETP **3** (1956) 307.

[77] L. F. Foldy and R. F.Peierls, Phys. Rev. **130** (1963) 1585.

[78] A. Donnachie and P. V. Landshoff, *Total cross-sections*, Phys. Lett. B **296** (1992) 227;
A. Donnachie and P. V. Landshoff, *Elastic Scattering And Diffraction Dissociation*, Nucl. Phys. B **244** (1984) 322;
A. Donnachie and P. V. Landshoff, *P P And Anti-P P Elastic Scattering*, Nucl. Phys. B **231** (1984) 189.

[79] S. Aid *et al.* [H1 Collaboration], *Measurement of the Total Photon Proton Cross Section and its Decomposition at 200 GeV Centre of Mass Energy*, Z. Phys. C **69** (1995) 27.

[80] K. Schilling and G. Wolf, *How To Analyze Vector Meson Production In Inelastic Lepton Scattering*, Nucl. Phys. B **61** (1973) 381.

[81] S. Aid *et al.* [H1 Collaboration], *Elastic Photoproduction of ρ^0 Mesons at HERA*, Nucl. Phys. B **463** (1996) 3.

[82] S. Aid *et al.* [H1 Collaboration], *Elastic Electroproduction of ρ^0 and J/ψ Mesons at large Q^2 at HERA*, Nucl. Phys. B **468** (1996) 3.

[83] S. Aid *et al.* [H1 Collaboration], *Elastic and Inelastic Photoproduction of J/ψ Mesons at HERA*, Nucl. Phys. B **472** (1996) 3.

[84] C. Adloff *et al.* [H1 Collaboration], *Proton dissociative ρ and elastic ϕ electroproduction at HERA*, Z. Phys. C **75** (1997) 607.

[85] C. Adloff *et al.* [H1 Collaboration], *Photo-production of $\psi(2S)$ mesons at HERA*, Phys. Lett. B **421** (1998) 385.

[86] C. Adloff *et al.* [H1 Collaboration], *Elastic electroproduction of ρ mesons at HERA*, Eur. Phys. J. C **13** (2000) 371.

[87] C. Adloff *et al.* [H1 Collaboration], *Elastic photoproduction of J/ψ and Υ mesons at HERA*, Phys. Lett. B **483** (2000) 23.

[88] C. Adloff *et al.* [H1 Collaboration], *Measurement of elastic electroproduction of ϕ mesons at HERA*, Phys. Lett. B **483** (2000) 360.

[89] C. Adloff *et al.* [H1 Collaboration], *A measurement of the t dependence of the helicity structure of diffractive ρ meson electroproduction at HERA*, Phys. Lett. B **539** (2002) 25.

[90] C. Adloff *et al.* [H1 Collaboration], *Inelastic photoproduction of J/ψ mesons at HERA*, Eur. Phys. J. C **25** (2002) 25.

[91] C. Adloff *et al.* [H1 Collaboration], *Inelastic leptoproduction of J/ψ mesons at HERA*, Eur. Phys. J. C **25** (2002) 41.

[92] C. Adloff *et al.* [H1 Collaboration], *Diffractive photoproduction of $\psi(2S)$ mesons at HERA*, Phys. Lett. B **541** (2002) 251.

[93] A. Aktas *et al.* [H1 Collaboration], *Elastic J/ψ production at HERA*, submitted to Eur. Phys. J. **C**. [hep-ex/0510016].

[94] M. Derrick *et al.* [ZEUS Collaboration], *Measurement of elastic rho0 photoproduction at HERA*, Z. Phys. C **69** (1995) 39.

[95] M. Derrick *et al.* [ZEUS Collaboration], *Measurement of Elastic ϕ Photoproduction at HERA*, Phys. Lett. B **377** (1996) 259.

[96] M. Derrick *et al.* [ZEUS Collaboration], *Measurement of the Reaction $\gamma^* p \to \phi p$ in Deep Inelastic $e^+ p$ Scattering at HERA*, Phys. Lett. B **380** (1996) 220.

[97] M. Derrick *et al.* [ZEUS Collaboration], *The ZEUS leading proton spectrometer and its use in the measurement of elastic ρ^0 photoproduction at HERA*, Z. Phys. C **73** (1997) 253.

[98] J. Breitweg *et al.* [ZEUS Collaboration], *Elastic and proton-dissociative ρ^0 photoproduction at HERA*, Eur. Phys. J. C **2** (1998) 247.

[99] J. Breitweg *et al.* [ZEUS Collaboration], *Measurement of elastic Υ photoproduction at HERA*, Phys. Lett. B **437** (1998) 432.

[100] J. Breitweg *et al.* [ZEUS Collaboration], *Exclusive electroproduction of ρ^0 and J/ψ mesons at HERA*, Eur. Phys. J. C **6** (1999) 603.

[101] J. Breitweg *et al.* [ZEUS Collaboration], *Measurement of exclusive ω electroproduction at HERA*, Phys. Lett. B **487** (2000) 273.

[102] J. Breitweg *et al.* [ZEUS Collaborations], *Measurement of the spin-density matrix elements in exclusive electroproduction of ρ^0 mesons at HERA*, Eur. Phys. J. C **12** (2000) 393.

[103] S. Chekanov *et al.* [ZEUS Collaboration], *Exclusive photoproduction of J/ψ mesons at HERA*, Eur. Phys. J. C **24** (2002) 345.

[104] S. Chekanov *et al.* [ZEUS Collaboration], *Exclusive electroproduction of J/ψ mesons at HERA*, Nucl. Phys. B **695** (2004) 3.

[105] S. Chekanov [ZEUS Collaboration], *Exclusive electroproduction of ϕ mesons at HERA*, Nucl. Phys. B **718** (2005) 3.

[106] S. Eidelman *et al.* [Particle Data Group], *Review of particle physics*, Phys. Lett. B **592** (2004) 1.

[107] H1 Collaboration, *Combined H1 ZEUS Figures on Heavy Quark Physics*, http://www-h1.desy.de/h1work/hq/figures_public.html (2003).

[108] L. Frankfurt and M. Strikman, *Large T, Triple Pomeron Diffractive Processes In QCD*, Phys. Rev. Lett. **63** (1989) 1914 [Erratum-ibid. **64** (1990) 815];
A. H. Mueller and W. K. Tang, *High-energy parton-parton elastic scattering in QCD*, Phys. Lett. B **284** (1992) 123.

[109] J. R. Forshaw and M. G. Ryskin, *Diffractive vector meson production at large momentum transfer*, Z. Phys. C **68** (1995) 137.

[110] J. Bartels, J. R. Forshaw, H. Lotter and M. Wüsthoff, *Diffractive Production of Vector Mesons at Large t* Phys. Lett. B **375** (1996) 301.

[111] D. Y. Ivanov, R. Kirschner, A. Schäfer and L. Szymanowski, *The light vector meson photoproduction at large t*, Phys. Lett. B **478** (2000) 101 [Erratum-ibid. B **498** (2001) 295].

[112] J. R. Forshaw and G. Poludniowski, *Vector meson photoproduction at high-t and comparison to HERA data*, Eur. Phys. J. C **26** (2003) 411.

[113] R. Enberg, J. R. Forshaw, L. Motyka and G. Poludniowski, *Vector meson photoproduction from the BFKL equation. I: Theory*, JHEP **0309** (2003) 008;
G. G. Poludniowski, R. Enberg, J. R. Forshaw and L. Motyka, *Vector meson*

photoproduction from the BFKL equation. II: Phenomenology, JHEP **0312** (2003) 002.

[114] P. Ball and V. M. Braun, *Higher twist distribution amplitudes of vector mesons in QCD: Twist-4 distributions and meson mass corrections*, Nucl. Phys. B **543** (1999) 201.

[115] B. Cox, J. R. Forshaw and L. Lonnblad, *Hard colour singlet exchange at the Tevatron*, JHEP **9910** (1999) 023.

[116] J. Forshaw, Private Communication.

[117] R. Heremans, *Triple Regge Analysis of Sinlge Diffractive Photoproduction at HERA*, Ph.D. Thesis, Vrije Universiteit Brussel (2002).

[118] F. Jacquet and A. Blondel, DESY Report, **DESY-79-048**.

[119] L. West, *How to use the Heavy Flavour Wroking Group Track, Muon and Electron Selection Code*, H1 internal software manual (1997).

[120] V. Shekelyan *et al.*, *Simulation and Reconstruction in H1 Liquid Argon Calorimetry*, H1 Internal Note, **H1–IN–288 (04/1993)**.

[121] X. Janssen, *Electroproduction diffractive de méson ρ à HERA*, Ph.D. Thesis, University Libre de Bruxelles (2002).

[122] B. Heinemann, *Measurement of Neutral Current and Charged Current Cross Sections in Positron-Proton Collisions at* $\sqrt{s} = 300$ GeV, Ph.D. Thesis, Universität Hamburg (1999).

[123] K. Goulianos, *Diffractive Interactions Of Hadrons At High-Energies*, Phys. Rept. **101** (1983) 169.

[124] T. Sjostrand, *High-energy physics event generation with PYTHIA 5.7 and JETSET 7.4*, Comput. Phys. Commun. **82** (1994) 74.

[125] S. P. Cocks, *Rho Prime Electroproduction at HERA*, Ph.D. Thesis, University of Liverpool (1998).

[126] S. Bentvelsen, J. Engelen and P. Kooijman, *Reconstruction of (x, Q^2) and extraction of structure functions in neutral current scattering at HERA*, Proc. Workshop on Physics at HERA, Vol.1, Edited by W. Buchmller, and G. Ingelman (1992) 23.

[127] B. List *et al* [ETH Zürich Group], Private Communication.

[128] J. D. Jackson, *Remarks On The Phenomenological Analysis Of Resonances*, Nuovo Cim. **34** (1964) 1644;
G. E. Gladding, J. J. Russell, M. J. Tannenbaum, J. M. Weiss and G. B. Thomson, *Measurement Of Photoproduction Of Omega0 And Rho0 Mesons In Hydrogen*, Phys. Rev. D **8** (1973) 3721;
G. Mcclellan *et al.*, *High-Energy Photoproduction Of Rho-Neutral Mesons From Hydrogen And Deuterium*, Phys. Rev. Lett. **22** (1969) 374.

[129] M. Ross and L. Stodolsky, *Photon Dissociation Model For Vector Meson Photoproduction*, Phys. Rev. **149** (1966) 1172.

[130] P. Söding, *On The Apparent Shift Of The Rho Meson Mass In Photoproduction*, Phys. Lett. **19** (1966) 702.

[131] H1 Collaboration, *Photoproduction of ρ Mesons with a leading Proton*, Contrib. pap. 991 to the 31^{st} International Conference on High Energy Physics, Amsterdam 2002.

[132] R. Enberg, Private Communication.

[133] J. Orear, *Notes on Statistics for Physics*, Cornell University Report, **CLNS 82/511** (06/1982).

[134] F. James and M. Roos, *'Minuit' A System For Function Minimization And Analysis Of The Parameter Errors And Correlations*, Comput. Phys. Commun. **10** (1975) 343.